HHS Public Access

Author manuscript

Chem Soc Rev. Author manuscript; available in PMC 2023 January 04.

Published in final edited form as:

Chem Soc Rev. ; 51(1): 329–375. doi:10.1039/c9cs00621d.

Visible-Light and Near-Infrared Fluorescence and Surface-Enhanced Raman Scattering Point-of-Care Sensing and Bio-imaging: A Review

Yingjie Hang, **Jennifer Boryczka**, **Nianqiang Wu***

Department of Chemical Engineering, University of Massachusetts Amherst, Amherst, MA 01003-9303, United States

Abstract

This review article deals with concepts, principles and applications of visible-light and near-infrared (NIR) fluorescence and surface-enhanced Raman scattering (SERS) in *in vitro* point-of-care testing (POCT) and *in-vivo* bio-imaging. It has discussed how to utilize the biological transparency windows to improve penetration depth and signal-to-noise ratio, and how to use surface plasmon resonance (SPR) to amplify fluorescence and SERS signals. This article has highlighted some plasmonic fluorescence and SERS probes. It has also reviewed the design strategies of fluorescent and SERS sensors in detection of metal ions, small molecules, proteins and nucleic acids. Especially, it has provided perspectives on integration of fluorescent and SERS sensors into microfluidic chips as lab-on-chips to realize point-of-care testing. It has also discussed the design of active microfluidic devices and non-paper- or paper-based lateral flow assays for *in vitro* diagnostics. In addition, this article has discussed the strategies to design *in vivo* NIR fluorescence and SERS bio-imaging platforms for monitoring physiological processes and disease progression in live cells and tissues. Moreover, it has highlighted applications of POCT and bio-imaging in testing toxins, heavy metals, illicit drugs, cancers, traumatic brain injury, infectious diseases such as COVID-19, influenza, HIV and sepsis.

Graphical Abstract

*Corresponding author: Tel: +1-413-545-6175, nianqiangwu@umass.edu.

Conflict-of-Interest Statement:
The authors declare no conflict of interests.

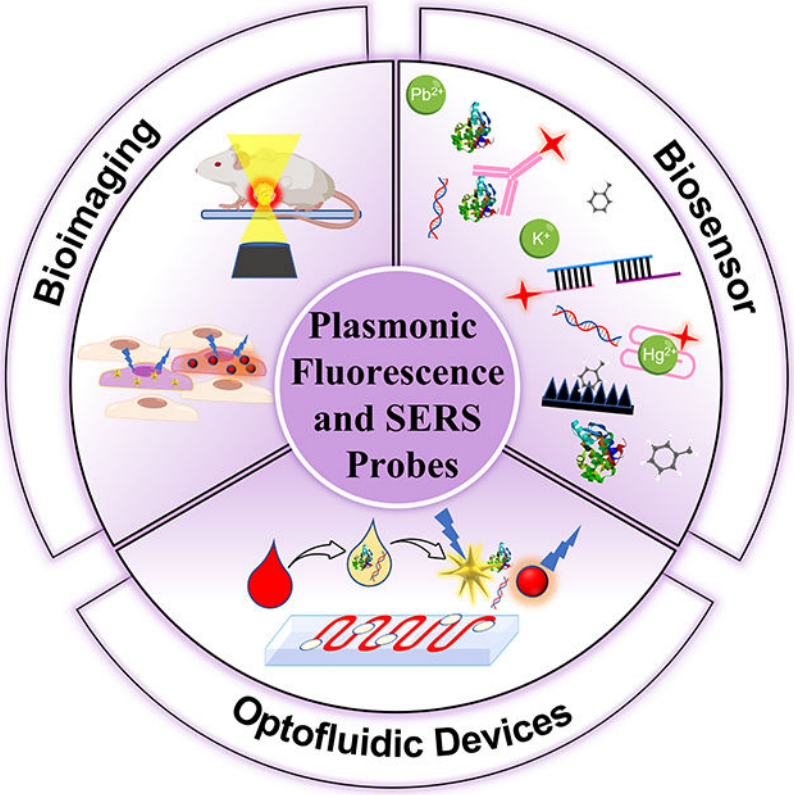

This article reviews the principles, design and applications of visible-light and near-infrared fluorescence and surface-enhanced Raman scattering in point-of-care testing and bio-imaging.

Keywords

fluorescence; surface-enhanced Raman scattering (SERS); surface plasmon resonance (SPR); microfluidic device; optofluidic device; lab-on-chip; point-of care testing; bio-imaging

1. Introduction

Chemical compounds in human fluids and tissues reflect physiological or pathological processes, and can be used for diagnosis of diseases and assessment of medical intervention efficacy. It is essential to perform *in vitro* analysis of analytes such as metal ions, small molecules, proteins and nucleic acids in human fluids (blood, serum, plasma, urine, saliva and cerebrospinal spinal fluid).[1–5] In most cases, *in vitro* analysis is performed with large-scale analytical techniques such as spectrophotometry, mass spectrometry, immunoassays, and electrophoresis. For example, enzyme-linked immunosorbent assay (ELISA) and polymerase chain reaction (PCR) techniques are considered the gold standards for quantitation of soluble proteins and nucleic acids, respectively. Although ELISA and PCR are accurate methods, they are expensive, tedious, time-consuming, and require professionals to operate in a central laboratory. These shortcomings have motivated the development of point-of-care testing (POCT) tools to meet needs of inexpensive,

rapid, high-throughput, field-deployable, *in vitro* analyses by laypersons.[6–8] Emergency of pandemics (such as swine flu (HIN1), severe acute respiratory syndrome (SARS), and COVID-19) and prevalence of epidemic diseases (such as malaria, dengue chikungunya, yellow fever and Zika) have aroused an increasing demand of POCT tools to rapidly test these infectious diseases at home, clinics, schools, employer sites, community or hospitals.

To enable portability, numerous sensors have been developed for *in vitro* analysis. According to the signal transduction mechanism, sensors can be categorized to different types such as electric, electrochemical, acoustic, magnetic, colorimetric, fluorescent, Raman devices and etc.. Among these types of sensors, fluorescence and surface-enhanced Raman scattering (SERS) devices have a great promise in *in vitro* analysis of human fluids due to their high sensitivity and high resistance to interference from sample matrices.[9–11] For sensing applications, visible-light fluorescence and SERS probes are widely used because fluorescence dyes have large fluorescence quantum yield and Raman reporters have large scattering cross-section, leading to strong signals in buffer sample matrices. Although most of NIR-fluorescence dyes exhibit lower quantum yield than visible-light counterparts, and NIR Raman dyes have smaller scattering cross section, they are subject to less interference from sample matrices of blood and plasma due to the reduced light absorption and less auto-fluorescence. On the other hand, it is worth noting that not all sensors are POCT tools because these sensors still require multi-step operation by well-trained personnel in field or even in a laboratory. One of effective means to enable POCT is integration of sensors into microfluidic chips to create lab-on-chips, which are characteristic of militarization, field-deployment, automation, swiftness, minimally- or non-invasive detection, and easy operation by laypersons.[12, 13] The availability of POCT tools will extend *in vitro* diagnosis (IVD) from hospitals to clinics and community.

Besides *in vitro* testing, NIR fluorescence and SERS are finding increasing applications in *in vivo* imaging due to their minimally- or non-invasive detection and relatively deep penetration into human tissues compared to other ultraviolet and visible-light analytical techniques. Current common bio-imaging technologies include magnetic resonance imaging (MRI), computed tomography (CT), ultrasound, X-ray radiography as well as positron-emission tomography scanning (PETS).[14] However, these techniques are quite time-consuming and require minutes to hours to achieve imaging results. Besides, they are unable to obtain target-specific results and usually need professionals to distinguish the target area from background. Also, long-time exposure to radiation under X-ray radiography, CT and PETS may do harm to human health. Thus, it is difficult to obtain long-term and real-time imaging.[15, 16] In contrast to these imaging modalities, NIR fluorescence and SERS enable real-time monitoring of expressed genes, pathogens, metabolites, drug compounds in living cells and tissues. Moreover, the target-specific results enhance diagnostic accuracy.

This article will first clarify the importance of biological transparent windows for selecting NIR fluorescence and SERS for POCT and bio-imaging, and then describe how to use plasmon to enhance the intensity of fluorescence emission and SERS. Next, it will give a summary of the design strategies of fluorescence and SERS sensors in detection of metal ions, small molecules, proteins and nucleic acids, placing an emphasis on the signal transduction and signal amplification. Subsequently, this article will describe a combination

of sensors and sample handling modules in single microfluidic devices to create lab-on-chips toward POCT. Lastly, it will give an overview of bio-imaging based on NIR fluorescence and SERS, including instruments, probes and applications, and highlight how the principles of signal transduction and amplification are used in imaging living cells and tissues.

2. Optical Properties of SERS and Fluorescence

2.1 Biological transparency windows

For optical detection and imaging, an incident light beam is directed to sample to excite light-matter interaction, and a detector is used to collect light emitted or scattered from the sample. Biological samples may strongly absorb both the incident and the emitting light. Also, auto-fluorescence emission can occur under excitation of the incident light, leading to interference. These effects may attenuate the incident light quickly with an increase in the penetration depth, reduce the intensity of emitting/scattering light, and increase the signal-to-noise ratio. Such side effects become deteriorated in the ultraviolet (UV) and visible-light spectral ranges, which make it difficult or even impossible for deep-tissue imaging and trace analyte detection. Fortunately, these side effects are minimized in three NIR spectral ranges, which are called “biological transparency windows”. The first biological window covers the wavelength from 650 nm to 950 nm (NIR-I), the second biological window ranges from 1000 nm to 1350 nm (NIR-II), and the third biological window spans from 1550 nm to 1870 nm (NIR-III).[16–18] In short, this interprets why NIR fluorescence sensing or SERS imaging systems should be designed within the biological transparency windows. For example, traditional organic fluorescent dyes exhibit fluorescence in visible-light or NIR-I window, such as indocyanine green (ICG) and methylene blue (MB) NIR-I probes.[15] Recently, many newly developed organic dyes show the extended emission wavelengths at the NIR-II window.[19] Fluorescence of quantum dots can be tuned from visible-light, NIR-I to NIR-II or NIR-III windows by tailoring the size or/and chemical composition. Semiconducting single-walled carbon nanotubes exhibit fluorescence emission in the NIR spectral range mainly between 900 and 1600 nm, corresponding to NIR-II or NIR-III windows.[16]

Figure 1 shows the light absorption spectra obtained from human skin, which guides selection of the biological transparency windows for *in vivo* optical imaging (IVI).[16] Figure 2 reveals the molecules that cause strong light absorption and scattering in human tissues.[20] The major light-extinction molecules in human tissues are, but not limited to, melanin, collagen, fat, water and blood (e.g., Ox-Hgb, D-Hgb). Light below 650 nm is strongly absorbed by oxy-hemoglobin (Ox-Hgb) and deoxy-hemoglobin (D-Hgb), while water is the main absorber in the spectral range over 1350 nm (Figure 2).[20] It can be seen from Figure 1 that both absorption and scattering of light are reduced dramatically when the wavelength increases from the UV and visible-light regions to the NIR regions. As the wavelength falls into the biological transparency windows, light scattering decreases significantly; and light absorption is maintained at a low level in the spectral range 500 nm to 1300 nm with a small increase in NIR-III region. Therefore, optical loss in human tissues is minimal in the three biological transparency windows.

It is worth noting that light scattering is evident in a narrow spectral region (1350–1550 nm) between the NIR-II and the NIR-III windows. Also, a narrow spectral region (950–1000 nm) between the NIR-I and the NIR-II windows should be avoided for bio-imaging and detection although light scattering is negligible. Light is absorbed in this spectral region by water in biological samples, as shown in Figure 3, and the absorbed light can heat biological samples.[21] This is why the NIR upconversion rare-earth nanoparticles such as $NaYF_4$:Yb, Er, which are typically excited by a 980 nm laser, may encounter a problem when they are used for bio-imaging and detection.

In buffer sample matrices, better limit of detection can be achieved using visible-light fluorescence probe because of their higher fluorescence quantum yields than the NIR counterparts. However, the visible-light fluorescence intensity can be reduced largely in blood or plasma matrices due to strong light absorption and auto-fluorescence of sample matrix. In contrast, the intensity of NIR fluorescence (or SERS) probes may be reduced slightly or even not change when the sample matrix is switched from buffer to blood/plasma. Hence, NIR fluorescence and SERS probes are attractive for *in vitro* diagnosis (IVD), especially for blood or plasma samples. Figure 3 shows the light absorption spectra obtained from human blood and plasma, which guides the selection of the excitation light sources, dyes and fluorophores for *in vitro* optical detection in blood or plasma sample matrices. This figure reveals the major molecules in blood that cause strong light absorption and auto-fluorescence.[21] The light-absorption molecules include oxy-hemoglobin (Ox-Hgb), deoxy-hemoglobin (D-Hgb) and bilirubin. D-Hgb exhibits the strongest light absorption at around 420 nm and the second light absorption peak at around 580 nm. Ox-Hgb displays its strongest light absorption at around 410 nm, and two secondary peaks at 550 nm and 600 nm. Overall, light absorption by Ox-Hgb and D-Hgb decreases with an increase in the wavelength, and becomes much weaker in the spectral range above 770 nm. Auto-fluorescence leads to a low signal-to-background. The typical auto-fluorescence molecules in blood are amino acids and proteins, pyridoxine (Pyr), retinol A (Ret), collagen (Col), cholecalciferol (Chol), folic acid (FA), and porphyrin (PP).[22–25] These molecules may exhibit strong auto-fluorescence in the visible-light regions, as shown in Figure 3. Interestingly, auto-fluorescence becomes low in both the NIR-I and NIR-II windows in a blood sample matrix. The author's group has compared the behavior of visible-light and NIR fluorescence probes in buffer and plasma, respectively. It has been found that fluorescence intensity of visible-light fluorescence dye (Rhodamine 6G) was reduced by more than 50% when the sample matrix was switched from buffer to blood or plasma. In stark contrast, the NIR fluorescent dye (Cyanine 7) exhibited a negligible change in the fluorescence intensity.

The prevailing colorimetric paper-based lateral flow assays employ gold nanoparticles as the colorimetric probes. These gold nanoparticles typically exhibit light absorption maximum at around 520–560 nm, showing a red wine-like color on the test line of assay, which is visible to human eyes. When these colorimetric paper-based lateral flow assays are applied to blood, serum and plasma samples, they suffer from severe interference of biomolecules in sample matrices, leading to poor sensitivity and repeatability. In contrast, NIR fluorophores and SERS probes that fall into the biological transparency windows (NIR-I and NIR-II) have advantages when testing plasma, serum and whole blood samples. Typically, the 785 nm or 1064 nm laser is used to excite SERS probes. And the typical examples of

NIR fluorophore are organic dyes (e.g., indocyanine green, IGG), quantum dots (QDs, e.g., Ag_2S), carbon nanomaterials (e.g., single-wall carbon nanotube, SWCNTs), infrared fluorescent proteins (IFPs) as well as halide perovskite nanocrystals (e.g., lead halide perovskite, LHP).[14, 19, 26–29]

2.2 Surface plasmon resonance

Although NIR fluorescence or SERS detection systems in the biological transparency windows are characteristic of the reduced light absorption and the minimized autofluorescence from biological samples, their signals are relatively low compared to the visible-light counterparts. NIR fluorophores typically exhibit lower quantum efficiency than visible-light counterparts. The quantum yield of visible-light fluorophores typically ranges from 20% to 80%, and is reduced to ~10% for NIR-I fluorophores, and only ~0.01–1.4% for NIR-II counterparts except for some nanomaterials such as PbS quantum dots.[30] On the other hand, Raman scattering of a molecule is dipole-like interaction with the excitation light, which makes Raman scattering strength is proportional to the frequency of the excitation light to the fourth power. Consequently, Raman scattering signal is greatly reduced when shifting from the visible-light to the NIR spectral regions. Therefore, surface plasmon resonance (SPR) is typically tuned into the NIR spectral region to enhance NIR fluorescence and SERS. Thus, we introduce the SPR concept and the plasmon-enhancement principles before we talk about the NIR fluorescence and SERS sensing/imaging. Understanding the underling mechanism will enable “devices-by-design” and “materials-by-design”.

SPR is a phenomenon that numerous conduction electrons collectively oscillate on the surface of metallic nanostructure upon resonant excitation of incident light.[31] It can generate an intense local electromagnetic (EM) field surrounding the nanostructure, which can modulate optical process including photon absorption, Raman scattering and fluorescence.[32] SPR has two typical forms, namely, propagating surface plasmon polariton (SPP) and localized SPR (LSPR). SPP refers to electron oscillation on the surface of a thin metal film when the frequency of incident light is smaller than the plasma frequency (Figure 4a).[32] The SPP frequency is determined by plasma frequency of bulk metal (ω_p) and dielectric constant of surrounding medium (ε_{diel}), which is expressed as[33, 34]

$$\omega_{\mathrm{SPP}}=\frac{\omega_{\mathrm{p}}}{\sqrt{(1+\varepsilon_{\mathrm{diel}})}} \tag{1}$$

Here, ω_p is the plasma frequency of bulk metal and is expressed as

$$\omega_{\mathrm{p}}=\sqrt{\frac{ne^2}{m_{eff}\varepsilon_0}} \tag{2}$$

where ω_p is determined by the charge carrier density (n) and charge (e) of electrons, the effective mass (m_{eff}) as well as permittivity of free space (ε_0).[35] The generated EM field can extend into the dielectric environment, which decays in ~100–200 nm.[36] When it comes to a nanoparticle (NP), plasmon will occur in the form of LSPR (Figure 4b)[32] if the size of metallic NP is comparable or smaller than the wavelength of the incident light. The electron

density of nanoparticle displays a uniform displacement.[32] A strong restoring force is then formed due to the positive ionic core background, which ultimately results in a characteristic oscillation frequency in the metal electrons like a simple harmonic oscillator.[37, 38] In the Mie theory or a simple harmonic oscillator model, the extinction cross-section of light absorption and scattering induced by LSPR in a nanosphere is given by[37]

$$\sigma_{\text{ext}} = 9\left(\frac{\omega}{c}\right)(\varepsilon_{\text{diel}})^{\frac{3}{2}}V\frac{\varepsilon''_{\text{metal}}}{(\varepsilon'_{\text{metal}}+2\varepsilon_{\text{diel}})^2+(\varepsilon''_{\text{metal}})^2} \quad (3)$$

in which ω is frequency of light, V is the volume of the spherical nanoparticle, ε_{diel} is the dielectric constant of surrounding medium, ε'_{metal} and ε''_{metal} are the real and imaginary parts of the dielectric function, respectively.[38] The denominator can be vanished when ε'_{metal} is negative and ε''_{metal} is small at the required wavelength range such as near-infrared range. Strong plasmon resonance could be achieved at[39, 40]

$$\omega_{\text{LSPR}} = \frac{\omega_{\text{P}}}{\sqrt{(1+2\varepsilon_{\text{diel}})}} \quad (4)$$

In addition, the factor of 2 in front of ε_{diel} is a variation dependent on the shape of nanoparticle.[32] Therefore, the LSPR frequency is dependent upon the nanoparticle shape in addition to other two factors (metal types and surrounding environment). The EM field generated by LSPR shows a shorter decay (~10–30 nm) compared to EM field from SPP (~100–200 nm).[41, 42] Specifically, for nanoparticles (NPs) with sharp edges or a small gap (<10 nm) between neighboring plasmonic NPs, it will form “hot spots” where EM field is concentrated with further enhanced field intensity (Figure 4c, d).[43, 44] In addition, after LSPR is excited by incident light, both energy absorption and re-radiation occur along with light absorption and scattering in plasmon. Generally, no obvious Stokes shift between absorption and scattering spectra of the NPs, since radiative decay of LSPR is often earlier than non-radiative process.[45] Whereas, whether it occurs absorption and scattering are dependent on particle size. For metal nanoparticles smaller than 15 nm, light absorption dominates, then plasmon absorbs energy and quickly transfers it into heat.[46, 47] In nanoparticles larger than 15 nm, plasmon tends to re-radiate energy, inducing light scattering with a large scattering cross-section.[46, 47]

2.3 SERS-enhancement mechanisms and SERS probes

Mechanisms: Raman scattering is extremely inefficient. The cross-section of Raman scattering (10^{-28}–10^{-30} cm^2 per molecule) is ~14 orders of magnitude weaker than the fluorescence cross section of fluorophores (10^{-16} cm^2).[48,49] Fortunately, this problem is mitigated by SERS, which is Raman scattering enhanced by molecules adsorbed on metallic nanostructures or rough surfaces, or semiconductor.[50] SERS signals ae typically enhanced by chemical enhancement or/and electromagnetic enhancement (EM) mechanisms.[51, 52] The chemical enhancement mechanism relies on charge transfer between metal substrate and Raman molecules, which is estimated in two cases.[53–55] For the first case, charge transfer forms a new energy state of metal substrate-molecules system. Such charge transfer itself could increase Raman scattering; and resonance of charge transfer system further enhances

the SERS signal after excited by incident light. For the second case, a new electron transfer pathway is either from the highest occupied molecular orbital (HOMO) of the molecule to the unoccupied state above the Fermi level of the metal substate, or from the lowest unoccupied molecular orbital (LUMO) of the molecule to the occupied state below the Fermi level of the metal substrate, assuming that the Fermi level of the metal substrate could match with the HOMO or LUMO of molecule.

The EM enhancement mechanism is based on the enhanced localized EM field around a plasmonic metal nanostructure.[11, 56] In case of influence of both chemical enhancement and EM enhancement, the SERS signal intensity (P_{SERS}) can be estimated by[42]

$$P_{SERS} \propto \text{chemical enhancement} \times \text{EM enhancement} \tag{5}$$

$$P_{SERS} \propto N \cdot \alpha^{R}_{abs} \cdot |A(\upsilon_e)|^2 \cdot |A(\upsilon_s)|^2 \cdot I(\upsilon_e) \tag{6}$$

at which N is the number of molecules absorbed on the metal substrate; α^{R}_{abs} is the Raman probability of the absorbed molecules; $A(\upsilon_e)$ and $A(\upsilon_s)$ represents the enhancement factors of excitation and Raman scattering light, respectively; $I(\upsilon_e)$ shows the intensity of excitation light. In this equation, α^{R}_{abs} is the main contributor for CE mechanism since $I(\upsilon_e)$ influenced by CE is negligible, while $A(\upsilon_e)$ and $A(\upsilon_s)$ is the main contributor to EM enhancement. By comparison, enhancement factor from EM enhancement (between 10^4 and 10^8) is much larger than that of CE mechanism (between 10 to 100), thus EM enhancement is dominant in SERS enhancement.[57] If just considering EM enhancement, the SERS enhancement factor (EF) can be determined as[42]

$$\mathrm{EF}_{EM} = \frac{P_{SERS}}{P_{0,\,SERS}} = |A(\upsilon_e)|^2 \cdot |A(\upsilon_s)|^2 = \left|\frac{E^{LOC}(\omega_e)}{E^{I}(\omega_e)}\right|^2 \cdot \left|\frac{E^{LOC}(\omega_s)}{E^{I}(\omega_s)}\right|^2 \tag{7}$$

at which $P_{0,SERS}$ represents the SERS signal intensity without EM enhancement. E^I and E^{LOC} are the amplitudes of the excitation and local electric fields, respectively. ω_e is the frequency of excitation light and ω_s is the frequency of Raman scattering light. Because Raman shift between excitation and Raman scattered frequency is smaller than width of LSPR range, Raman shift can be ignored (that is, ω_e is approximate to ω_s), which gives $|A(\upsilon_e)|^2 \sim |A(\upsilon_s)|^2$. Therefore, the SERS enhancement factor by the EM field (EF_{EM}) can be approximated by[54]

$$\mathrm{EF}_{EM} = \frac{|E(\omega_e)|^4}{|E_0(\omega_e)|^4} \tag{8}$$

In other words, when molecules are in the enhanced localized EM field, both the intensity of incident light and Raman scattering light of molecules are enhanced. The SERS signal is maximal with an $|E^4|$ enhancement when both excitation and Raman scattered frequency are in the resonance with LSPR frequency. Following the EM enhancement mechanism, the Raman reporter molecules should be placed as close to the plasmonic metal as possible when designing SERS probes. This is because the plasmon-included EM field usually

decays exponentially away from the plasmonic nanoparticle. The design of SERS probes is different from that of the plasmonic fluorescence probes where the fluorophores are typically kept a distance of 10–30 nm away from the plasmonic nanoparticle.

Apart from these two traditional SERS enhancement mechanisms, a new mechanism named "molecular hot spots" was proposed recently.[58] It is found that the polarizability of aromatic molecules conjugated on a plasmonic metal nanoparticle interact strongly with SPR, leading to a spatially extended the enhanced EM field into the conjugated aromatic molecule assembly. This creates "molecular hot spots" surrounding the metal nanoparticle. The enhanced EM field is delocalized and spread throughout the aromatic molecule layer on the surface of metal nanoparticle. The "molecular hot spots" can be generated in aromatic molecules even on a small metal nanoparticle (<15 nm) with weak LSPR. The "molecular hot spots" can result in large enhancement of SERS signals of other molecules that are co-adsorbed with the aromatic molecules on the metal substrate. Even linear-chain molecules, which typical have extremely low polarizability, can exhibit strong SERS signals when they co-exist with aromatic molecules near the metal nanoparticle.

SERS probes: Based on the EM enhancement mechanism, SERS probes have been designed typically with three types. The first type is "Raman dyes".[59–61] To enable high sensitivity, Raman reporter dyes require relatively large scattering cross sections, such as molecules with highly polarizability moieties, e.g., conjugated π-systems.[61, 62] For spectral multiplexing properties, it is necessary for molecules to have the minimal number of vibrational Raman bands and no spectral overlap. Because Raman dyes have no SERS effect themselves, Raman dyes must be coupled to a rough metal surface or a plasmonic metal nanostructure to enable EM enhancement during SERS detection. Raman dyes may be modified with additional functional groups to allow for covalent bonding to the surface of metals.[61, 63] Based on these criteria, many "Raman dyes" have been selected or developed, including benzotriazole derivatives (e.g., Rhodamine 6G, R6G), malachite green isothiocyanate (MGITC), olefin- or alkyne-based molecules (e.g., 5-ethylnyldeoxyuridine, EdU).[59]

The second type is "metal@Raman reporter", in which Raman reporter molecules are attached on a metal nanoparticle. Because the Raman scattering cross-section of Raman reporter molecules is quite small, only 10^{-28}–10^{-30} cm^2 per molecule, they alone cannot be used as a SERS probe.[49] Typically, plasmonic metal nanoparticles such as Au or Ag are utilized to generate LSPR to amplify Raman signals. Because LSPR-induced EM field are decayed to a very blow level beyond a distance of about 30 nm away from the particle surface, Raman reporters are required to stay in close proximity to the metal nanoparticles. Thus, metal@Raman reporters are formed through surface functionalization of plasmonic nanoparticles with Raman reporters.[42] The SH- or NH_2− containing molecules with great affinity to Au or Ag substrate are usually chosen as Raman reporters, such as malachite green isothiocyanate (MGITC), 4-aminothiophenol (4-ATP), 4-mercaptobenzoic acid (4-MBA), 4-mercaptopyridine. (4-MPY), and 5,5-dithiobis-2-nitrobenzoic acid (DTNB).[64–66] To further enhance the SERS signal of Raman reporters, many researchers have engineered the metal nanoparticle shapes from nanospheres to nanorods and nanostars. It was reported that more sharp tips in nanoparticles generate stronger EM field, thus nanostars showed the

highest SERS enhancement, nanorods took the second place, while nanospheres exhibited the lowest enhancement.[44] The “metal@Raman reporter” particles may aggregate in an aqueous solution with high ionic strength or get detached from the metal particle surface during sensing/imaging, which leads to signal loss and poor repeatability.[44, 67] On the other hand, it is difficult to conjugate additional antibodies or DNA into the “metal@Raman reporter” particles due to occupancy of Raman dyes on the metal surface.

The third type is sandwich-structured “metal core@Raman dye@shell” particle,[44] in which the Raman reporter molecules are sandwiched between a metal core and an outer shell. This prevents from leach out of Raman reporter molecules during detection. The plasmonic metal core is used to amplify SERS signals. The thin outer shell is typically made from silica (SiO_2) or polymers such as polyethylene glycol (PEG).[44,68–70] The silica shell not only provides a clean surface for bioconjugation with antibodies and DNA, but also render excellent water-solidity, which make the sandwich-structured SERS probe stable in an aqueous solution with high ionic strength such as blood. In short, the sandwich-structured SERS probes are characteristic of high sensitivity, robustness, water-solubility, and biocompatibility and repeatability.[44]

In general, both the second and the third types of SERS probes can be used in buffer sample matrices in sensing applications. Also, the sandwich-structured “metal core@Raman dye@shell” SERS probes are stable and robust in blood and plasma matrices. However, the “metal@Raman reporter” SERS probes may aggregate in blood or plasma due to high ionic strength of sample matrices.

2.4 Plasmon-enhanced fluorescence mechanisms and NIR fluorophores

Mechanisms: SPR is the most common means for enhancing fluorescence. Because gold and silver are the most popular plasmonic materials. Hence plasmon-enhanced fluorescence (PEF) is sometimes called “metal-enhanced fluorescence (MEF)”, or “surface-enhanced fluorescence (SEF)”. The mechanisms of plasmon-enhanced fluorescence are described in detail in literature[32, 71] Briefly, when a fluorophore is located near a plasmonic nanostructure, energy transfer can occur between the plasmon and the fluorophore via the Förster resonance energy transfer (FRET) process or/and the Purcell effect.[32, 71] For metal nanostructures which primarily scatter, enhancement will be possible through both FRET at short distances (~10 nm) and the Purcell effect at a long distances (10–50 nm). At short distances (~1–10 nm), FRET can take place from the donor to the acceptor via the dipole-dipole interaction.[32, 71] It occurs when the emission band of the donor overlaps with the absorption band of the acceptor, fluorescence of the donor is then quenched. The FRET efficiency (Eff_{FRET}) depends on the dipole-to-dipole separation distance (R) and the Förster distance (R_0) (usually ranges from 3 nm to 8 nm) of this pair of dipoles, as expressed by[72]

$$\mathrm{Eff}_{\mathrm{FRET}} = \frac{1}{1 + \left(\frac{R}{R_0}\right)^6}. \tag{9}$$

The efficiency of FRET decays as $1/R^6$, while the Purcell effect scales with$1/R^3$, and becomes dominant in a longer distance (~10–50 nm). Purcell effect originates from a

resonant cavity that modulates the local density of optical states (LDOS) that is expressed as[73]

$$\rho_{\mathrm{LDOS}}(\omega) \sim |E_{loc}(\omega)|^2, \quad (10)$$

where $|E_{loc}(\omega)|^2$ represents the normalized local electric field of the cavity according to the incident field intensity. When the radiative dipole is in the resonant cavity of plasmonic nanostructures and the plasmon's absorption or scattering band is overlapped with fluorescence emission band, LDOS increases, leading to a higher rate of fluorescence emission into the cavity as compared to the dipole in air. The transferred energy can be absorbed or re-radiated as scattering by the cavity, leading to quenching or enhancement of fluorescence emission.

Considering the spectral overlap of the plasmon and the fluorescence, and the gap, quenching or enhancement of fluorescence emission can be determined (Figure 5a, b).[32] Firstly, when the plasmon band is overlapped with the fluorophore absorption band in Figure 5a, fluorescence emission can be enhanced.[32] It can be illustrated as follow. For the metal nanoparticles smaller than ~15 nm, the particles mainly absorb and generate an enhanced EM field, leading to the excitation enhancement by FRET, followed by the emission enhancement. It should be noticed that plasmon's radiation enhanced by the Purcell effect is negligible, thus excitation is only enhanced by FRET within a few nanometers of distance in this case. For the metal nanoparticles larger than ~15 nm, the particles mainly scatter, both FRET at short distance and the Purcell effect at long distance can result in enhanced fluorescence emission.[32, 46, 74] Secondly, when the plasmon band is overlapped with fluorophore emission band in Figure 5b, quenching or enhancement of fluorophore emission can be achieved.[32] At a short distance (~10 nm) between the plasmon and the fluorophore, fluorescence emission can be quenched through FRET. At a distance beyond FRET (> 10 nm), strong Purcell enhancement is induced because of the large local density of states (LDOS) of the local plasmonic field, which increases the radiative rate of the fluorophore, and if the plasmon can scatter efficiently, strong emission enhancement can occur.[32, 46, 74] Typically the maximum enhancement takes place at an optimal gap of 10–30 nm between the plasmon and the fluorophore. Besides the overlap of plasmon and absorption/emission band, it is important to choose suitable laser line. For the overlap of plasmon and absorption band, signal laser line is enough to excite both plasmon and fluorescence probe. When plasmon is overlapped with emission band, two laser lines are required. One laser line with shorter wavelength is used to excite fluorescence probe, another with longer wavelength can excite plasmon.

Recently, a new mechanism, plasmon-induced resonance energy transfer (PIRET), is proposed for plasmon enhanced fluorescence.[75] It is also non-radiatively energy transfer via the dipole-dipole interaction. Different from FRET which only occurs from the donor at a shorter-wavelength to the acceptor at a longer-wavelength, PIRET can realize the blue-shift coherent energy transfer from the longer-wavelength donor to the shorter-wavelength acceptor. For a plasmon-fluorophore pair, when the SPR band of plasmon is overlapped with the absorption band of fluorophore, the emission intensity of fluorophore can be enhanced through PIRET. The schematic mode of energy transfer is showed in Figure 5c.[45] It often

comes to plasmon spectrum overlaps simultaneously with absorption and emission spectrum of the fluorophore, such that FRET occurs to quench fluorescence and PIRET takes place to enhance fluorescence simultaneously. The net influence of FRET and PIRET is determined by the dephasing time (T_2), which is expressed by[45, 75]

$$\frac{1}{T_2} = \frac{1}{2T_1} + \frac{1}{T_2^*} \tag{11}$$

where T_1 refers to the recombination time of relaxation from the excited state to the ground state of plasmon (or fluorophore), T^*_2 refers to pure dephasing time of plasmon (or fluorophore). Given T^*_2 (around fs range) is much shorter than T_1 (around ps range), T_2 is related to T^*_2. If the fluorophore's dephasing time is faster than the plasmon's, PIRET shows higher efficiency than FRET and the net influence is enhanced fluorescence. Conversely, FRET dominates in the whole process with the result of quenched fluorescence.

NIR fluorophores: Various NIR fluorophores are commercially available, such as organic dyes, inorganic quantum dots (QDs), carbon nanomaterials, halide perovskite nanocrystals and fluorescent proteins.[14,19,26–28] Plasmonic fluorescence probes are typically formed by placement of the above fluorophores near a plasmonic nanoparticle with an optimal gap of 10–30 nm. It is necessary to have a spacer to keep an optimal gap to prevent from quenching of fluorescence. The spacer can be a thin SiO_2 layer, a polymer, a double-stranded DNA, an aptamer and etc..[76–81] For example, an Au nanostar@SiO_2@double strand DNA-labeled Cy5.5 probe was created, showing the enhanced NIR fluorescence.[82] The 22 nm-thick SiO_2 shell has optimized the fluorescence enhancement to 21 folds. Besides silica, polymers can also be used as shell or a spacer to separate NIR fluorophore from a plasmonic nanoparticle.[79,83] In addition, the biotin-avidin complex has also been used as the spacer.[83] The biotinylated bovine serum albumin was self-assembled on the surface of Au nanostar, followed by incorporation of streptavidin-labeled fluorophores via the biotin-avidin interaction. Because the biotinylated bovine serum albumin and the streptavidin are around 8 nm and 4 nm in size, respectively, a 12 nm of gap was created between the fluorophores and the Au nanostar, which activated the Purcell effect for fluorescence enhancement.

The plasmonic fluorescence probes based on PIRET show advantages in bio-sensing and bio-imaging.[45, 75, 84, 85] Because it is a blue-shifted energy transfer from the longer wavelength end to the shorter wavelength end, excitation can reduce photodamage to biological samples. The signal-to-noise ratio can also be improved. For example, Wang *et al.* have developed the Au nanorods covered by a merocyanine-doped poly(methyl methacrylate) film.[45] It was observed that PIRET occurred when there was a significant overlap between the LSPR band and the fluorophore absorption band, which has resulted in an average enhancement factor up to 1854. As PIRET is a newly discovered mechanism for fluorescence enhancement, the plasmonic fluorescence probes based on PIRET have just emerged.

In a special case, when the Raman scattering and the fluorescence spectra are overlapped for a fluorescent molecule at a given excitation wavelength. That is, both SERS and

fluorescence are enhanced by the plasmonic electric field. The total cross-section ($\sigma_{(total)}$) of spectrum is theoretically the sum of the Raman scattering cross-section spectrum ($\sigma_{(RS)}$) and the fluorescence cross-section spectrum ($\sigma_{(FL)}$)[86]

$$\sigma_{(total)} = \sigma_{(RS)} + \sigma_{(FL)} \tag{12}$$

Owing to enhancement by EM field, the total cross-section becomes

$$\sigma_{(enhanced\ total)} = \sigma_{(\mathrm{E}RS)} + \sigma_{(\mathrm{E}FL)} \tag{13}$$

$$\sigma_{(\mathrm{E}RS)} = \sigma_{(RS)} \cdot |A(v_e)|^2 \cdot |A(v_s)|^2 \tag{14}$$

It is noted that $|A(v_e)|^2 \cdot |A(v_s)|^2$ is an enhancement factor of electric field intensity. The $\sigma_{(\mathrm{E}FL)}$ item in Eq.(13) includes the product of EM enhancement of absorption and fluorescence. The EM enhancement of absorption ($|A(v_e)|^2$) is equivalent to an increase in the effective absorption cross-section. The EM enhancement ($|A(v_s)|^2$) is due to emission enhanced by coupling of the plasmon resonance with fluorescence light. Simultaneously, fluorescence may be quenched by a factor of q through a resonance energy transfer process. Thus, these synergistic effects lead to

$$\sigma_{(\mathrm{E}FL)} = q \quad \sigma_{(FL)} \cdot |A(v_e)|^2 \cdot |A(v_s)|^2 \tag{15}$$

Combining Eq.(13), Eq.(14) and Eq.(15),

$$\sigma_{(enhanced\ total)} = \left[\sigma_{(RS)} + q\sigma_{(FL)}\right] \cdot |A(v_e)|^2 \cdot |A(v_s)|^2 \tag{16}$$

The enhanced light intensity is proportional to the enhanced total cross-section, and dependent on the fourth power of electric field.

3. Design of Fluorescence and SERS Sensors

In this section, we review the design of fluorescence and SERS sensors for detection of typical analytes in healthcare and biomedical research. We discuss how to transduce and amplify sensing signals. In addition, we highlight the application examples of fluorescence and SERS sensors.

Signals of both fluorescence and SERS can be amplified dramatically by surface plasmon resonance, achieving high sensitivity of detection, even reaching single molecule level. It is worth noting that SERS signals increase with a decrease in the distance between the Raman reporter and the plasmonic nanostructure while fluorescence signals of a fluorophore reach a maximum at an optimal distance between the fluorophore and the plasmonic nanostructure. On the other hand, both NIR fluorescence and SERS have strong resistance to interference from complex sample matrices (blood and plasma), and have deep penetration capability in bio-imaging. When designing sensors, keep in mind that few analyte molecules have signature or characteristic fluorescence peaks, while many

analytes can generate fingerprinting or signature SERS spectra. Therefore, SERS can be used to conduct label-free detection of many trace analyte molecules, and is good at real-time monitoring metabolites from live cells. Low-cost fluorescence readers are well developed, and a lot of commercial products are available. In contrast, today Raman readers are more expensive than fluorescence counterparts. But rapid technology progress will increase portability and reduce costs of Raman readers in the future. Indeed, this trend was expedited in the last decade. Palm-sized Raman readers, which can be operated with cell phones via Bluetooth, are available commercially now. As for *in vitro* imaging, both modern fluorescence and Raman microscopes are able to real-time image live cells quickly. As for *in vivo* imaging, commercial fluorescent probes and imaging instruments are also well developed and available commercially. *In vivo* collection of Raman signals from deep tissues remains a challenge.

3.1 Protein sensors

Significance: In human, proteins play important roles in multiple facets of life: growth and maintenance of cells and tissues, delivery of messages, retention of mechanical integrity of cells and tissues, regulation of pH values, transport and storage of nutrients, supply of energy, performing reactions, and fighting infection. The state-of-the-art ELISA can achieve a LOD down to ~10 pM toward protein measurement in serum. But the levels of proteins range from 10^{-16} to 10^{-12} M in serum in some cases of diseases.[87, 88] Hence it is essential to develop highly sensitive sensors to meet such need.

Signal transduction: In sensor design, proteins are selectively recognized by specific ligands, such as antibodies, aptamers, peptides and polymers through affinity, electrostatic and hydrophobic interactions. Several signal transduction modes have been developed for protein detection. The first one is formation of a sandwiched antibody-antigen-antibody structure (Figure 6a). The capture antibody is initially immobilized on a solid substrate; and the detection antibody labelled with a fluorescence or SERS probe is suspended in a solution. In the presence of an analyte (antigen), the antigen will bind to both the capture and the detection antibodies, forming a sandwich structure and immobilize the optical probes close to the solid substrate. After washing non-specific biomolecules away, the number of the immobilized optical probes reflects the analyte concentration in a sample. The second mode is a competitive immunoassay (Figure 6b), in which a detection antigen labelled with an optical probe is initially bound to the capture antibody fixed on a solid substrate. When an analyte (antigen) is present, it will bind to the capture antibody because the analyte has a higher affinity to the capture antibody than the detection antigen. In the meanwhile, the detection antigen labelled with an optical probe will go away due to loss of binding competition. Besides antibodies, aptamers (single-stranded DNA or RNA) are alternative candidates of molecular recognition elements to proteins. They can replace antibodies in a sandwiched assay (Figure 6c). An aptamer can also serve as a molecular beacon to transduce fluorescence or SERS signal (Figure 6d). Initially a fluorophore and a gold nanoparticle are linked to two ends of a hairpin-structured aptamer, respectively; and emission of the fluorophore is quenched by gold nanoparticle via FRET. When an analyte (antigen) is present in the assay, the analyte will bind to the aptamer and open the loop of hairpin, pushing the gold nanoparticle away from the fluorophore. This turns on emission of

the fluorophore. If the fluorophore is substituted by a Raman dye, SERS signals will scatter from the Raman dye due to EM-enhancement by the nearby plasmonic gold nanoparticle. When an analyte is present in the assay, SERS signals will be turned off due to moving of the gold nanoparticle away from the Raman dye.

Applications: Following the above signal transduction modes, various NIR fluorescence or SERS sensors are built. Wu's group developed a sandwich-structured SERS immunosensor, where the Au nanostar@Raman dye@SiO_2 nanoparticles acted as SERS probes and the Au triangle nanoarray served as the solid substrate, respectively (Figure 7a).[87] Compared to traditional Au nanosphere particles and a planar Au film, a high density of "hot spots" in 3D hierarchical architecture was generated by coupling the Au nanostars to the Au triangle nanoarray in the presence of antigen analyte, amplifying the SERS signals remarkably. It showed a wide dynamic linear range from 0.1 pg/mL to 10 ng/mL at LOD of 7 fg/mL toward human immunoglobulin G (IgG) protein in a buffer solution. It eliminated multiple washing steps and directly detected vascular endothelial growth factor (VEGF) in blood plasma samples of clinical breast cancer patients. This antibody/antigen/antibody sandwich immuno-sensors are most common for protein detection.[89–96] For example, the graphene quantum dots (QDs)-capture antibody/CA-125 antigen/detection antibody-labelled with horseradish peroxidase (HRP) (Ab–HRP) sandwich immuno-sensor was designed for detection of the CA-125 ovarian cancer biomarker.[97] When the antigen (CA-125) was present, chemiluminescence catalyzed by HRP was quenched by the graphene QDs via a resonance energy transfer process. In addition, many efforts have been made to develop optical probes in the sandwich immuno-sensor. Apoferritin with a cavity structure is an intriguing example.[97, 98] It not only exhibits biocompatibility but also entrap tens of fluorophores or quantum dots into the cavity for signal amplification.[97]

Antibodies are expensive and produced by a complicated synthesis process, and require low temperature for storage. Hence, substitution of antibodies with aptamer are receiving more attention because aptamers possess the tailored specificity and affinity, relatively high thermostability, and can be produced massively to almost any epitope in a programable route.[99] Figure 7b shows an aptamer-based sandwich assay for detection of a cancer biomarker in buffer and diluted human serum.[100] A pair of aptamers was immobilized on the surface of recombinant fluorescent ferritin nanoparticles as optical probe, and the targeted cancer biomarker was sandwiched by the pair of aptamers. Such an aptamer sensor achieved a LOD down to 100 fM in a buffer.

Competitive immunoassays simplify the procedure and require the reduced steps of operation compared with sandwich-structured assays.[91, 101–103] Figure 7c reveals a FRET-based competitive sensor for detection of the cyclic adenosine 3',5'-monophosphate (cAMP) protein that was used for evaluation of G protein-coupled receptor activation.[102] Prior to detection, fluorescence of the donor dye was quenched, but fluorescence was emitted from the acceptor dye due to the FRET effect. When the analyte (cAMP) appeared in the assay, the FRET process was interrupted, and the donor emitted fluorescence. Competitive assays can also employ aptamers as the molecular recognition elements.[104–107] Xing *et al.* designed an aptamer-based competitive sensor for determination of human epidermal growth factor receptor 2 (HER2).[105] Initially, the HER2-specific aptamer linked with the MnCuInS/ZnS

QDs was hybridized with a complementary single-stranded DNA (ssDNA) linked to a gold nanoparticles NPs. The double-stranded DNA (dsDNA) was rigid and held the Au nanoparticle close to the QDs, and enabled FRET, leading to quenching of fluorescence of the QDs. During the detection process, binding of the aptamer to HER2 led to dissociation of dsDNA due to higher affinity of the aptamer with HER2. As a result, the ssDNA became free-standing, and the gold nanoparticles were kept away from the QDs, which tuned on fluorescence of the QDs. This aptamer-based FRET sensor achieved a LOD of 1 ng/mL with a detection range from 2 to 100 ng/mL, and successfully distinguished the healthy (2–15 ng/mL) from the disease individuals (15–75 ng/mL).

3.2 Nucleic acid sensors

Significance: Nucleic acid sequences are usually used to identify a particular species or subspecies of organism.[108, 109] Either deoxyribonucleic acid (DNA) or ribonucleic acid (RNA) acts as a carrier of genetic information for viruses and bacteria. DNA expression is an important index in evaluating the number of bacteria, such as *S. aureus*, *S. typhimurium* as well as *Escherichia coli*.[110, 111] Typical DNA-based viruses include hepatitis B virus (HBV), herpes virus and papilloma virus seriously threaten human health. Early detection of viruses is essential to prevention and treatment of diseases.[112] Different from double-helix structure of DNA, RNA is often found as a single-stranded molecule in nature. It is the main genetic material in most viruses, such as SARS, COVID-19, Ebola, human immunodeficiency virus (HIV), influenza virus as well as tobacco mosaic virus.[6,113,114] RNA also plays significant roles in coding, decoding and expression of genes, among which miRNAs (20–24 nucleotides) are a group of endogenous and noncoding RNAs, which are essential in post-transcription of gene expression. They are closely associated with proliferation, differentiation, development and metabolism in cells. Hence, they act as valuable biomarkers in various physiological disorders like tumors, neural diseases, cardiovascular diseases and diabetes.[115, 116] Detection of nucleic acids is significant for early diagnosis of many diseases because nucleic acids are expressed at very early stage of diseases while antigens or/and antibodies appear in human fluids typically later or even much later than nucleic acids.

Nucleic acid amplification: In many cases, the expressed nucleic acids are at a very low level (10–1,000 copies/mL). Therefore, amplification is a necessary step prior to detection. Taking an advantage of chain reaction of nucleic acids, a variety of methods have been explored to make copies of nucleic acids, such as polymerase chain reaction (PCR), loop-mediated isothermal amplification (LAMP), recombinase polymerase amplification (RPA), strand displacement amplification (SDA), rolling circle amplification (RCA), ligase chain reaction (LCR) and sustained sequence replication (3SR).[117–122] Figure 8 exemplifies four mechanisms of nucleic acid amplification that are most commonly used in analytical devices.

i. PCR is carried out by temperature cycling (Figure 8a).[118] At high temperature of denaturation step, two strands of duplex DNA are fully separated. Temperature is then reduced to allow primers to anneal to each ssDNA. In the presence of deoxynucleoside triphosphates (dNTPs) and heat-stable polymerase, primers are

extended to form new double helical DNA at around 72 °C. Theoretically, the number of double-stranded DNA pieces is doubled in each cycle, achieving 2^n copies of DNA after *n* cycles in PCR process.

ii. LAMP is performed isothermally at 60–65 °C for 45–60min with aid of the specific DNA polymerase, dNTPs and primers (Figure 8b).[123] LAMP process starts when F2 region of Forward Inner Primer (FIP) hybridizes to F2c region of the target DNA and extends the strand, followed by F3 primer that is complementary to F3c region of the target elongating the strand. FIP-linked strand is then displaced and forms a loop at 5'-terminus, which also acts as a template for Backward Inner Primer (BIP). B2 region of BIP undergoes the similar strand synthesis as F2 region and opens 5'-terminus loop. The synthesized strand is then displaced by B3 primer extended strand, forming dumbbell-shaped DNA, which is an initiator of LAMP recycling. As a result, a mixture of stem-loop DNA structures with varied stem lengths and various cauliflower-shaped structures with multiple loops is obtained assisted by these primers.

iii. RPA was developed by Niall Armes *et al.* in 2006 using three proteins (recombinase protein, single-stranded binding protein and a strand displacing DNA polymerase).[124] A typical example is shown in Figure 8c.[125] The recombinase protein (T4 UvsX protein) binds to primers in the presence of loading factor (T4 UvsY) and adenosine triphosphate (ATP) to form a recombinase-primer complex that seeks homologous sequences in duplex DNA and inserted the strand by primers at the cognate site. Single-stranded binding protein (SSB, T4 gp32 protein) is used to prevent from ejection of the invaded primer by branch migration. Subsequently, the recombinase protein disassembles from the complex and a strand displacing DNA polymerase (*Bsu or Sau*) binds to the 3'-end of the primer and initiate the elongation assisted by dNTPs, ultimately resulting in exponential accumulation of target double helical DNA.

iv. SDA is also carried out under an *in vitro* isothermal condition. Figure 8d gives an example of SDA for miRNA amplification.[120] Primers used in SDA consists of a particular sequence (marked in red in Figure 8d) as the recognition site of the nicking enzyme. SDA starts with binding of the target miRNA to Primer 1 at 3'-end, followed by extension of Primer1 and miRNA in the presence of Klenow fragment polymerase. The nicking enzyme is added to cleave Primer 1 at the recognition site. Next, the elongation happens again at the nicking site, thus displacing the replicated strand that serves as new template in the following step and the left duplex strand enters the nicking step to initiate the first cycle. The replicated strand bonds with Primer 2 to trigger the second cycle through extension, nicking, polymerization and displacement steps and ultimately achieve the new target miRNA, which could also enter the first cycle.

Signal transduction: In biosensors, nucleic acids are usually recognized specifically by complementary base-pairing. Figure 9 shows five signal transduction modes that are usually used in optical sensors. Figure 9a reveals a classical "three-strand" mode, in which

the capture strand is grafted on a solid substrate and the detection strand functionalized with an optical probe is suspended in liquid. The analyte (single-stranded DNA or RNA) will be hybridized to the complementary capture and detection strands to form a rigid double-stranded DNA (or RNA). In Figure 9b, a fluorophore-labeled detection single strand is initially immobilized onto a graphene oxide sheet via π–π stacking and hydrogen bonding between the single-stranded DNA and graphene oxide. In this case, emission of the fluorophore is quenched by graphene oxide via FRET. After the analyte (ssDNA) and detection ssDNA forms a double-stranded DNA (dsDNA), the interaction between dsDNA and graphene oxide is too weak to overcome the interfacial electrostatic repulsion. Consequently, the dsDNA is pushed away from graphene oxide and disables FRET, turning on fluorescence emission. Figure 9c demonstrates signal transduction using a molecular beacon (MB), which is a single-stranded oligonucleotide containing 25–35 nucleotides.[126] In the absence of analyte, it is folded into stem-loop (hairpin) structure, where the loop part consists of 18–30 nucleotides, and the stem part comprises 5–8 base pairs labeled with a fluorophore; and the other end is immobilized onto a graphene oxide sheet or a plasmonic metal nanoparticle. In this case, emission of the fluorophore is quenched by graphene oxide or a plasmonic metal nanoparticle via FRET. When the loop part is hybridized to the complementary analyte (ssDNA), the loop will be opened, forming a rigid dsDNA, which can accurately control the gap between the fluorophore and the graphene oxide sheet (or plasmonic metal nanoparticle). This is because the inter-distance between two adjacent base-pairs in rigid dsDNA is 0.3 nm; the gap between two ends of dsDNA thus can be accurately tailored by the number of base-pairs with an increment of 0.3 nm. If the gap between two ends of dsDNA is large enough beyond the FRET effect, the fluorophore at one end will emit. Figure 9d illustrates signal transduction triggered by polymerase enzyme, where the target sequence is firstly hybridized with a probe-labeled strand and a primer which is located at one end of analyte. Polymerase enzymes is added to elongate the primer and digest the probe-labeled strand, leading to the release of the optical probe. After collection and detection of the released optical probes, the concentration of the analyte is derived eventually. Figure 9e presents a special enzyme-assistant assay using CRISPR/Cas12a system. With the guidance of CRISPR RNA (crRNA), CRISPR-Cas12a can recognize the analyte through a T nucleotide-rich protospacer-adjacent motif (PAM) site on the target dsDNA.[110, 127] The formed Cas12a-crRNA-analyte dsDNA ternary complex will activate the trans-cleavage activity of Cas12a to arbitrarily cut the fluorophore quencher-labeled ssDNA reporters, leading to recovery of fluorescence.

Applications: Figure 10a illustrates a classical “three-strand” mode-based DNA sensor.[112] The analyte, Hepatitis B Virus (HBV) DNA brought the SERS probes (Ag nanorice@Raman label@SiO_2 nanoparticles) close to a gold triangle nanoarray pattern, which created a 3D plasmonic field, and resulted in a SERS enhancement factor ($|E|^4$) of ~40,000, achieving a LOD of 50 aM in a buffer solution with specific discriminating a single-base mutant of DNA. It is desirable to combine nucleic acid amplification and detection in a single platform to perform nucleic acid amplification test (NAAT).[128–131] Guven *et al.* incorporated RCA with the “three-strand” detection scheme to detect the 35S promoter from cauliflower mosaic virus (CaMV35S) for tracking gene-modified organism.[129] After the analyte sequence was sandwiched by the primer and the capture strand on a gold substrate, the

primer was catalyzed by DNA ligase and hybridized with a RCA template. With assistance of the Phi29 DNA polymerase and dNTPs, long nucleic acid products were generated via RCA reaction, followed by hybridization with the detection strand-modified gold nanorods. This NAAT device reached a LOD of 6.3 fM with a wide detection range from 100 fM to100 nM.

Figure 10b shows a sensor based on “two-strand” mode as described in Figure 9b.[132] It has achieved a LOD of 1 pM toward miRNA in a buffer solution. The “two-strand” mode has also been used in NAAT.[133–135] For instance, a biosensor was constructed *via* target cycling amplification to detect highly pathogenic avian influenza H7N9 virus.[133] The number of analyte DNA after recycling was dependent on the released capture strands which were immobilized onto the surface of Ag nanorods. The detection strands labeled with fluorescent dye Cyanine-5 (Cy5) were finally hybridized with the capture strands to record the analyte concentration. This NAAT assay exhibited a linear range from 1 fM to100 pM at a LOD of 31 aM for H7 and 44 aM for N9 in buffer solutions, respectively.

Molecule beacons have been widely used in SERS and fluorescence sensors for nucleic acid detection.[126, 134–136, 139] Figure 10c reveals a NIR fluorescent sensor base on a molecule beacon labeled with the CdZnSeTeS QDs, showing a LOD of 2 copies/mL towards influenza virus H1N1 RNA in both buffer and human serum.[136] In addition, the molecular beacon mode-based detection scheme has been incorporated with the nucleic acid amplification methods. Figure 10d presents a NAAT assay using self-circulation of chain reaction between the target miRNA and a molecular beacon (A) together with other three hairpin structures without probes (B, C, D).[135] In the presence of analyte miRNA-34a, a breast cancer biomarker, the molecular beacon was unfolded via hybridization with miRNA-34a, forming a duplex with B (A-B) spontaneously. This released the target to activate the first cycle step 1–2. The A-B duplex entered the next cycles by formation of the C-D duplex, which catalyzed A and B to generate C-D in turn. This sensor detected 2.5 pM miRNA-34a in a buffer.

Enzymatic cleavage of phosphodiester linkages of DNA or RNA is also common in sensor design (Figure 9d).[140–142] Harper *et al.* utilized this method in a SERS sensor for determination of mecA gene sequence of *methicillin-resistant S. Aureus* (MRSA) bacterium (Figure 10e).[137] In this design, a sequence complementary to a specific region of mecA gene was modified with a 5’-biotin residue and a TAMRA dye-labeled 10 adenine bases at 3’-end, respectively, which was termed as TaqSERS probe. When the TaqSERS probe and a primer was hybridized to the target sequence, the Taq polymerase enzyme extended the primer with addition of deoxynucleoside triphosphate (dNTP) and digested TaqSERS probe simultaneously. The TAMRA dye-labeled DNA were then separated in the magnetic field after any free biotin and undigested TaqSERS probes were absorbed by streptavidin coated magnetic beads. The separated dye labeled DNA was aggregated by the negatively charged citrate surface of the Ag nanoparticles. In turn, these DNA sequence neutralized the charge of Ag nanoparticles, facilitating the formation of nanoparticle cluster. Compared with the fluorescence intensity of dye alone, incorporation of amplification method resulted in an order of magnitude lower LOD. Moreover, nucleic acid amplification by LAMP was combined with the enzyme-assisted detection scheme.[141] Briefly, after amplification by

LAMP, the products of analyte sequence of DNA were complementary to a capture ssDNA strand labeled with Cy5 and a Au nanoparticle. Cy5 and Au nanoparticle were linked by oligonucleotides in a close proximity (<2 nm), enabling remarkable enhancement of SERS signal from Cy5. Upon adding S1 nuclease, the SERS signal remained high intensity in the presence of the target DNA strands. Otherwise, the S1 nuclease digested ssDNA into free dNTPs, and separated Cy5 away from nanoparticles, leading to low SERS signals. Apart from amplification feature, nuclease was used to digest any non-specific DNA or potential contamination to minimize the interference to the SERS signals. This sensor was used to detect *Salmonella enterica*, a major foodborne pathogen, achieving a LOD of 66 CFU/mL in buffer.

CRISPR/Cas systems are adaptive immunity found in bacteria and archaea to degrade intruding nucleic acids, which have been wildly developed as gene-editing tools because of their recognition and degradation ability toward the target nucleic acids induced by Cas protein under direction of a guide RNA. CRISPR/Cas systems have been extended to sensor design for nucleic acid testing.[110, 127, 138, 143, 144] Figure 10f shows the use of CRISPR/Cas12a system to design a sensor for detection of breast cancer gene-1 (BRCA-1).[138] The sensor probe was designed as a 60 nm sized Au nanoparticle (60-AuNP); and a 20 nm sized Au nanoparticle (20-AuNP) were linked to a long fluorophore-labeled dsDNA (7 nm) and a short ssDNA (2 nm). Because the fluorescence probe was close to 60-AuNP, it was quenched by 60-AuNP at the initial state. When analyte BRCA-1 gene was present, it was complementary to crRNA and formed Cas12a-crRNA-BRCA-1 complex, activating the CRISPR/Cas system to cleave ssDNA in the surrounding environment. The ssDNA in the probe was then cut to dissociate fluorophore from 60-AuNP. As a result, fluorescence signal was emitted and enhanced by the 20-AuNP via FRET. Combination of CRISPR/Cas with FRET achieved a femtomolar level of LOD both in buffer and human serum condition within a short assay time (<30 min).

3.3 Small molecule sensors

Significance: Several types of small molecules affect human life and the surroundings, including inherent functional molecules, exogenous nutrients and prescribed medicine as well as toxins. Inherent functional molecules, such as adenosine triphosphate (ATP), glucose, bilirubin, non-essential amino acid (such as glycine, cysteine, alanine and tyrosine), play vital roles in regulating physiological and pathological processes.[4, 145–147] For example, ATP transports chemical energy for cellular metabolism and is involved in various life activities, such as liver glycogen metabolism, cell proliferation, muscle contraction and nerve conduction.[64, 145, 148] Expression of ATP out of the intracellular concentrations (1–10 mM) is the sign of diseases including cardiovascular and Parkinson's disease.[148] Glucose exists as main energy resource in human adult blood with a normal level less than 100 mg/dL (5.6 mmol/L) after an overnight fast.[149] Diabetes are confirmed if the blood glucose level reaches 126 mg/dL (7 mmol/L) or higher on two separate tests. Diabetes is a global metabolic disease diagnosed by over 463 million people worldwide.[149] Bilirubin is created from biliverdin catalyzed by enzyme biliverdin reductase during heme moiety catabolism and has potent antioxidant capacity to avoid reverting to biliverdin.[146, 150] It is normally excreted in urine and bile to maintain safe range (0.2–1.2 mg/dL) of total serum

bilirubin in a human adult; otherwise, excess accumulation of bilirubin is responsible for hyperbilirubinemia and jaundice.[150]

Nutrients such as essential amino acid and vitamin cannot be synthesized to a sufficient amount in the body and must be obtained from food, and are indispensable for human health with limited amount.[147, 151] Specifically, in the family of essential amino acid, methionine is associated with greying of hair, depression and atherosclerosis; lysine plays a crucial role in proteinogenesis and epigenetic regulation; valine takes part in blood sugar regulation.[152–157] In addition, adequate vitamin intake is important to enzyme-substrate reaction, growth and development. For the family of B complex vitamins, they form coenzymes to facilitate catalysis processes. For instance, thiamine (B1) can function as thiamine pyrophosphate (TPP) in the body and this coenzyme is a vital player in carbohydrate metabolism.[158] B9 participates in synthesis of nucleic acids, metabolism of amino acids and cell proliferation.[159] It is reported that long-term supplementation of B9 can lessen the risks of stroke, heart disease and prostate cancer.[160] The deficiency of these amino acids and vitamins causes functional disorders, for example, insufficiency of vitamin E can lead to myopathies, spinocerebellar ataxia, peripheral neuropathy and retinopathy etc.[161, 162]

Illicit drugs, pesticides, herbicides, food pollutants pose a threat to human health and the environment. Abuse of illicit drugs is a global problem with 271 million people (1 out of 18 people) from 15 to 64 years old.[163] Drug abuse is one of sources for hepatitis C and a quarter with human immunodeficiency virus (HIV).[164] Therefore, drug testing is essential to drug control and prevention. Nitrite, the main species in nutrient pollution, is of concern to the ecological system.[70] It is also widely present in meat products as food preservative and excessive consumption causes diseases such as diabetes, cancer and neurodegenerative diseases.[42, 165] The United States Environmental Protection Agency (EPA) and the Legislation of the European Union have enacted the maximum contaminant level (MCL) of nitrite at 1.0 μg/mL in drinking water and the maximum allowable level at 50 mg/kg in meat products, respectively.[70, 165] Release of pesticides and herbicides into surface waters can result in pollution of environment, accumulation in food chain, uptake by human eventually, leading to adverse health effects.[166, 167]

Signal transduction: In Figure 11, several signal transduction modes have been developed for detection of small molecules. Like detection of proteins, the capture antibody/analyte/detection antibody sandwich mode (Figure 11a), the molecular beacon-based mode (Figure 11b) and the competitive assay (Figure 11c) are also commonly used for signal transaction in small molecule sensors. Details of these three modes have been described above. Taking advantages of SERS, two unique signal transduction modes have been employed for small molecule detection. As shown in Figure 11d, aromatic compounds, such as amphetamine-type stimulants, dyes and phenolic pollutants, are SERS-active due to their high polarizability. They can be brought close to a plasmonic substrate for SERS detection. For the SERS-inactive analyte molecules, they may *in situ* react with specific reagents in an assay to produce SERS-active molecules. The SERS-active products can be brought close to a plasmonic substrate for SERS detection (Figure 11e).

Applications: Antibodies are widely used as molecular recognition elements in small molecule detection.[168–171] And signal transduction is typically realized by a sandwich-structured assay of the capture antibody/molecule/detection antibody-labeled with optical probe.[171] Such a type of assay with CdSe/ZnS QDs as fluorescence probes exhibited a LOD of 0.3 and 0.4 ng/mL toward clothianidin and thiacloprid in a sodium borate buffer, respectively. This sensor can be employed in different applications, such as river water, soil, cabbage, rice and tomato. In the last decade, more and more aptamers appeared to substitute antibodies as the molecule recognition elements for small molecule detection.[164,172–174] Guler *et al.* decorated QDs on the surface of μ-well plates and further grafted the cocaine-specific aptamer labeled with Au nanoparticles on QDs.[172] When cocaine was present, it was bound to the aptamer and made the aptamer folded to reduce the distance between the QDs and the Au nanoparticles, quenching fluorescence of QDs. It showed a LOD of 42 pg/mL in a PBS buffer, which was much lower than that of traditional liquid chromatography-tandem mass spectrometry (LC-MS, 0.162 ng/mL) and capillary electrophoresis-electrospray ionization-mass spectrometry (CE-ESI-MS, 100 ng/mL). This sensor was also able to distinguish cocaine even from its metabolite benzoylecgonine. With rapid development of specific ligands, competitive assay using different affinity is well established according to the signal transduction mode mentioned in Figure 11d. A competitive biosensor in Figure 12a was constructed using high affinity between morphine and Au nanoparticle because of the overall effects of phenolic hydroxy groups as well as tertiary nitrogen ring atom in morphine.[175] In this design, fluorescein was firstly quenched by colloidal Au nanoparticles via a nanometal surface energy transfer (NSET) process. After adding morphine, it coordinated to Au nanoparticles and introduced the aggregation of nanoparticles since it had two phenolic hydroxy groups, thus fluorescein was departed from the nanoparticles and turned on its fluorescence. This competitive assay utilized the specific interaction of morphine with Au nanoparticles, and exhibited high selectivity and sensitivity without interference from metal ions to other illicit drugs, and achieving LOD of 53 pM, 67 pM, 62 pM and 78 pM in buffer, serum, urine and urine, respectively. Competitive assays recently became more popular for small molecule detection due to availability of more commercial aptamers.[64] In Figure 12b, a gold film was initially modified with ssDNA that was hybridized to an aptamer labeled with a SERS probe (Au nanostar@malachite green isothiocyanate (MGITC)@SiO_2 nanoparticles).[64] Upon adding ATP molecules, the noncanonical G/A base pairs was disrupted in the duplex DNA due to higher affinity of ATP with the aptamer, leading to detachment of the aptamers from the gold surface. This sensor showed a very low LOD of 12.4 pM toward ATP detection in a buffer solution because strong SERS signals were originated from the enhanced electromagnetic field around Au nanostars as well as “hot spots” generated between Au nanostars and Au substrate.

Many small molecules contain benzene rings, which are usually SERS-active. Such molecules can be trapped on a plasmonic substrate to trigger SERS signals. Following this principle, various SERS sensors have been constructed.[42, 176, 177] Huang *et al.* fabricated an Au@Ag nanopillar array with a 10 nm of gap between adjacent pillar tips.[176] Due to its enhancement factor up to 10^7, this SERS sensor was able to detect 5×10^{-6} M 2,3,3’-trichloribiphenyl (PCB20) pesticide. To create stronger “hot spots”, Zhu *et al.* developed a hierarchically ordered arrays of Ag-nanorod bundles with about 2 nm of gaps between

adjacent nanorods.[178] This increased the SERS enhancement factor to 10^8. Furthermore, this sensor was also able to distinguish multiple analytes simultaneously, which benefited from the narrow band of each peak in SERS spectra. Using a Ag nanorod bundle array, methyl parathion had the characteristic bands at 852, 1109, 1260, and 1328 cm^{-1} while 2,4-dichlorophenoxyacetic acid (2,4-D) exhibited specific peaks at 436, 915,1298, 1373, and 1620 cm^{-1}. The strong EM field enhancement ($E/E_0 \sim 3 \times 10^4$) of the Ag nanorod bundle array not only achieved high sensitivity toward methyl parathion (a LOD of 21.5 nM) and 2,4-dichlorophenoxyacetic acid (2,4-D, a LOD of 61.9 nM) in water, but also discriminated two pollutants in a mixture. To trap and preconcentrate the charged or polar analytes, electrophoresis can be integrated into SERS sensors because charged or polar analytes are driven to the oppositely charged electrode under the electric field. This process was employed for selective detection of polar molecules by altering potential polarity. Recently, a copper microgrid, which was modified with germanium nanowires and further decorated with Ag nanoparticles, served as both an electrode and a SERS substrate (Figure 12c).[166] After applying a voltage, the evenly distributed analytes in the solution were forced to move along the electric field to the SERS substrate, leading to a high concentration near the substrate. In this case, polar antibiotics, 2.4 nM 6-aminopenicillanic acid and 0.9 nM penicillin G were detected, which were approximately 5.7 and 2.8 folds of improvement by electrostatic preconcentration.

In situ detection of chemical reaction products of an analyte can result in low interference and high signal-to-noise ratio. Figure 12d shows a SERS sensor for detection of glucose in saliva.[149] The Au nanostar@SiO_2 core-shell nanoparticles were functionalized with glucose oxidase enzyme. It catalyzed glucose to produce H_2O_2 that exhibited finger-print SERS peak. The produced H_2O_2 molecules were close to the surface of core-shell nanoparticles, which was subject to strong electromagnetic field generated by the “hot spot” near the Au nanostar tips, amplifying SERS signals remarkably. This sensor was not interfered by co-existing ascorbic acid and uric acid, and it showed a dynamic range of concentration from 25 μM to 25 mM toward glucose detection in saliva. An additional intriguing example is that the product from the *in situ* chemical reaction served as a linker, which was covalently bound to two adjacent SERS substrates.[70] In their design, the Ag nanopyramid array and the Au nanostar were modified with1-naphthylamine (1-NA) and 4-aminothiophenol (4-ATP), respectively (Figure 12e).[70] After analyte (nitrite) was present in the assay, it reacted with 1-NA and 4-ATP to form the azo group that was sandwiched between the Au nanostar and the Ag nanopyramid array. Owing to a small gap, the “hot spots” between the Ag nanopyramid and the Au nanostars significantly enhanced the SERS signals of azo group, and showed a LOD of 0.6 pg/mL toward nitrite detection in water with a wide linear detection range from 1 pg/mL to 10 μg/mL, which covered the MCL of 1.0 μg/mL of nitrite in drinking water regulated by U.S. EPA.

3.4 Metal ion sensors

Significance: Metal ions include essential metals in living organisms (potassium, sodium, copper, zinc and iron ions, and etc.) and toxic ions (mercury, silver, lead, chromium and arsenic ions, and etc.). The former ions play an important role in various physiological processes such as enzyme catalysis, cell growth and metabolism, while the toxic ions pose

a threat to human health and the ecological environment.[11, 179, 180] For example, potassium (K^+) and sodium (Na^+) ions are critical in many biological functions, including management of blood pressure and pH, nerve, muscle and enzyme activity.[181, 182] Interaction of heavy metals, such as mercury (Hg^{2+}) and silver (Ag^+), with biological systems threatens human health; and even a low level of intake makes it difficult to metabolize them.[69, 76, 183] Metal ions are usually measured by atomic absorption spectroscopy and inductively coupled plasma mass spectrometry (ICP-MS) in a central laboratory, which are expensive, tedious, time-consuming and require professional personnel to operate.[184] Therefore, portable sensors show a great potential in on-site measurement of metal ions.

Signal transduction: Metal ions alone are neither SERS-active nor fluorescence-active. To enable signal transduction in SERS or fluorescence sensors, they need to be specifically coordinated with small molecules or aptamers to form complexes prior to detection. Figure 13 illustrates several signal transduction modes for metal ion detection in SERS or fluorescence sensors. For example, a fluorescent molecule is initially quenched via a photo-induced electron transfer (PET) process (Figure 13a). After the molecule is bound to the metal ion, the PET process is interrupted, triggering fluorescence. In Figure 13b, plasmonic metal nanoparticles, which are functionalized with the SERS-active ligands with selective affinity to specific metal ions, are initially dispersed in a solution. When the metal ion analytes are present in the assay, the open end of the ligand will bind to the metal ions, which induces aggregation of plasmonic nanoparticles given that another end of the ligand is covalently linked to the plasmonic nanoparticle. As a result, the SERS-active ligand is located between the close-contact plasmonic nanoparticles, leading to strong SERS enhancement. Figure 13c shows signal transduction via DNA hybridization. Initially two ssDNA cannot be hybridized owing to their mismatched sequences deliberately designed. In the presence of the target metal ions, the metal ions will bind to ssDNA on the mismatched sites, leading to hybridization of DNA. In Figure 13d, an aptamer labelled with a fluorophore is initially immobilized on a graphene oxide sheet due to **π-π** interaction between the aptamer and the graphene oxide sheet. At this moment, emission of the fluorophore is quenched by graphene oxide via FRET. When an analyte is present, it will coordinate with the aptamer to form a G-quadruplex or a hairpin structure, breaking the **π-π** interaction. This the G-quadruplex or a hairpin structure will be repelled away from the graphene oxide sheet, turning on fluorescence emission.

Applications: The photo-induced electron transfer (PET) process in single entity of molecule has been used to design fluorescent sensors for metal ion detection (Figure 13a).[179, 185–187] Figure 14a. shows a molecule that consists of a fluorophore (rhodamine analog, Rh) and a triazacryptand (TAC) moiety that selectively binds to potassium ion, which forms an electron donor-accept structure.[181] In the absence of K^+ ions, PET led to weak fluorescence. After formation of a coordination complex with a K^+ ion, the PET process was inhibited, leading to strong fluorescence. Since TAC not only acted as an electron donor in sensing K^+ but also had ability to target mitochondrion, the sensor was employed to detect intracellular K^+. A wide detection range of 16 to 400 mM was successfully measured, showing a linear range of 100–300 mM. Taking an advantage of large coordination number of metal ions, complexes could form with two or more

molecules.[185, 188] For example, gold nanoparticles were grafted with 4-mercaptobenzoic acid (MBA) for Hg^{2+} detection (Figure 14b).[188] In the absence of Hg^{2+}, the functionalized gold nanoparticles were dispersed and repelled from each other due to the negative charging of the carboxylic terminal in MBA. At this moment, SERS signals of MBA molecule were very weak. When Hg^{2+} ions were present in the assay, Hg^{2+} ions were bound to the carboxylic moieties, leading to linkage between nanoparticles. This caused aggregation of Au nanoparticles, creating strong “hot spots” between neighboring nanoparticles. The MBA molecules were thus exposed to strong electromagnetic field in the “hot spots”, amplifying SERS signals of MBA remarkably. This simple SERS sensor showed a LOD of 5 ppt toward Hg^{2+} in water.

Figure 14c shows a SERS sensor based on the metal ion-induced DNA hybridization (Figure 13c).[69] A single-stranded DNA (ssDNA) was initially immobilized on a gold nanohole array substrate; and another ssDNA labelled with a SERS probe (gold nanostar@Raman-reporter@silica nanoparticle) was suspended in the solution. Because Hg^{2+} and Ag^{+} showed strong affinity to thymine nucleobase (T) and cytosine nucleobase (C) to form the T–Hg^{2+}–T and C-Ag^{+}-C structures, respectively, the presence of analytes resulted in the formation of double-stranded DNA and moved the SERS probes close to the gold nanohole array substrate. The “hot spots” were formed between the gold nanostars and the Au nanohole array, amplifying SERS signals. The sensor exhibited LOD of 2.3 pM for Hg^{2+} and 0.17 nM for Ag^{+} in human saliva. This sensor can be used to monitor the release of metal ions from the silver-mercury amalgams in dental fillings.

Because aptamers can be programmed to selectively bind to different analytes, there are a plenty of room for application of aptamers in sensors.[76, 182, 189] Wu’s group used an aptamer to construct a fluorescent sensor for Lead (II) ion detection (Figure 14d).[189] Initially an aptamer conjugated with QDs was immobilized on the graphene oxide sheet through **π-π** stacking interaction. Upon binding to Pb^{2+} ions, the aptamer was transformed to a G-quadruplex/Pb^{2+} complex, turning on fluorescence of QDs. This sensor reached a LOD as low as 90 pM and successfully applied to river water. Additionally, a special aptamer with catalytic nucleic acids (DNAzymes) activity, which can be activated by metal ions, provided an alternative method for detection.[191, 192] Lu’s group demonstrated this method by conjugating Zn^{2+}-specific DNAzyme with a quencher (Q2) at the end to lanthanide-doped upconversion nanoparticle, NaYF4:Yb,Tm@NaYF4 UCNP (Figure 14e).[190] The substrate strand of DNAzyme was linked with a fluorophore (F) and another quencher (Q1) at each end, respectively. Synergistic effect of Q1 and Q2 allowed complete quenching of the fluorophore in initial state. The Zn^{2+} ions activated the catalytic ability of DNAzymes, leading to cleavage of the scissile ribonucleotide adenosine (rA) and dehybridization of the substrate strand. This triggered emission of the fluorophore. In this design, the scissile ribonucleotide adenosine (rA) in the middle of the substrate strand was specifically protected by a 2’-nitrobenzyl photocage group (PG) that was photo-dissociated when the upconversion nanoparticles converted 980 nm NIR light into 365 nm emission. This showed precise control of the location and time in detection by regulating NIR light. Similarly, Wang *et al.* introduced it into a SERS sensor where the gold-coated substrate functionalized by DNAzyme. A cleavage substrate was used as a bridge with the bottom part hybridizing to

DNAzyme and the upper part to Au nanoparticles.[193] Upon addition of Pb^{2+}, the SERS signal was reduced due to the detachment of Au nanoparticle from the gold surface.

4. Optofluidic Devices Toward Point-of-Care Testing

Biosensors, which have been described in Section 3, have provided convenience for *in vitro* diagnosis. However, in many cases, these sensors have to be operated manually by professionals in a central laboratory, and thus cannot be used in POC settings. An effective solution is to incorporate SERS or fluorescent sensors into a microfluidic platform to form "all-in-one" optofluidic devices, which can pretreat samples, transport liquid, and detect analytes in a single chip. To enable POCT, optofluidic devices are desired to miniaturized, portable, automotive, non- or minimally-invasive, can be read out by a handheld or a portable reader, and operated by a layperson with minimized or no training. In this section, we highlight some important features and research progress in optofluidic devices that are relevant to POCT. In POC settings, devices are applied to various sample matrices such as water, buffer, saliva, urine and blood. Blood testing is most challenging among all these sample matrices in POC settings. So far, few commercial portable devices are available for direct and quantitative measurement of analytes in finger-prick whole blood samples in POC settings.

4.1 Criteria and features of point-of-care-technologies

Many people call biosensors and microfluidic devices as POC technologies, which is misleading. Not all biosensors and microfluidic devices can be identified as "point-of-care (POC)" technologies unless they meet the following criteria:[194, 195]

Portable: The whole detection system can be carried with a portable carry-on bag, and does not need installation in field except for "plug-in" actions. In addition, all reagents and devices can be stored at room temperature or in a refrigerator with a long shelf life.

Field-deployable: A POC device can be operated in field by end users without professional training at any place such as hospital bedside, emergency room, clinics, home, community and other settings. It should be automatic or just needs several simple steps from sample collection to result readouts. For blood testing, it is desirable to directly measure a finger-prick blood samples in field.

Accurate: A POC device should achieve the required analytical precision, accuracy and range with minimal false negatives and minimal false positives to meet sensitivity and specificity for a specific analyte in a real-world sample.

Rapid: For POC testing of non-nucleic acid samples, the detection duration is typically 5 to 30 minutes. For POC testing of nucleic acid samples, the detection duration is desired to be less than 45–60 minutes.

Affordable: The overall POCT cost should be much lower than that of current laboratory-based test kits. For example, testing a protein biomarker in blood with ELISA typically costs $100-$150 in USA. Correspondingly, the POCT testing may lead to a reduced cost down to $5–$50.

4.2 Active optofluidic devices

4.2.1 Design of operational components in microfluidic devices—Microfluidic devices can be categorized into active and passive microfluidics according to flow control processes. In active microfluidics, liquid flow is driven and/or controlled by active pumps (syringe pumps or pressure pumps).[13] It provides great flexibility in controlling velocity, volume and distance of fluids via regulation of external pressure. Here we introduce some operational components in active microfluidics that are important to POCT.

Pumps: For active microfluidic devices, traditional external pumping systems include syringe pump, vacuum pump, electro-osmotic pump, electrowetting devices.[13, 196–198] However, these pumps are large, expensive and some of them require training for operation. Thus, small and easy-operating pumps are desirable for POCT.[199] For example, a commercially available latex balloon served as a pressure pump to drive liquid flow in microfluidic channels; and sodium polyacrylate with high swelling ratio acted as a suction pump to accelerate flow by absorbing water.[200, 201] Additionally, some hand-operated systems including syringes and pipettes are used to inject liquid into microfluidic channels.[199, 202, 203] Similarly, one can push a deformable elastomer chamber with a finger to change pressure to deliver fluid into the target zones.[199]

Valves: Valve is another important component that stops fluid flow, changes flow direction and sequentially delivers multiple preloaded reagents.[13, 199, 204] Various types of valves have been developed to meet different needs in flow control. For instance, hydrophobic valves are introduced to stop or regulate liquid flow through generating a capillary barrier. Pneumatic valves operate flow based on a change in the pressure. Screwing, twisting, aligning holes or inducting magnetism can also realize fast switching and on-demand flow regulation.[205–207] Compared with these manually operating valves, a series of automatic valves have been designed to better satisfy automation requirement in POCT. For example, a meltable valve made of wax can open in response to heating to separate assay steps.[208] And an integrated pH-responsive hydrogel valve can sense the surrounding pH to display different extents of swelling or contracting to control flow.[209] In addition, retention burst valves with predetermined heights and widths can encode the capillary difference changes, enabling automatic sequential liquid delivery.[210] Moreover, elastic reversible valves on a centrifugal microfluidic platform are used to release liquid on demand. Furthermore, a circular chip incorporated with peptide microarrays can automatically separate, collect and detect five different proteins from a single serum sample.[211]

Mixing modules: Typically, mixing is performed by confluence of fluids from different inlets to induce molecule diffusion. Multiple S-shaped channels are exploited to increase the diffusion efficiency.[212] Apart from these passive micromixers with patterned channels, active stir mixing units can tune the mixing processes. For example, a stir mixing was powered by electrical field using two aqueous electrolyte solutions,[213] in which fluctuating waves were generated and propagated toward the downstream. Alternatively, flow instability conditions can be achieved by acoustic-driven micromixers, centrifugal mixers or magnetic mixers under magnetic fields.[197, 214, 215]

Purification/separation modules: In case of handing complex sample matrices such as blood, urine and silva, separation may be required to extract desirable analytes, or to remove non-specific molecules prior to detection. Classical separation methods, such as nanoporous membrane filtration, cross-flow filtration, electrophoresis and isotachophoresis, rely on size and/or charge difference of molecules in samples.[13, 199, 216–219] For example, in a three-stage spiral channel device, multiplex cross-flow channels were patterned along the spiraling direction. As a result., tumor cells and blood cells were separated by optimizing flow rate, achieving 1100-fold of analyte preconcentration.[217] In order to increase specificity, specific ligand-analyte interaction, or additional surface modification with ovine serum albumin (BSA) are used for sample separation. For example, a porous hierarchical graphene foam served as the channel substrate, in which the electrospun titanium dioxide nanofibers were modified with antibody of epidermal growth factor receptor 2.[220] The surface-modified substrate in microchannels can capture the protein analyte and remove non-specific species by washing. Additional simpler purification methods include modulation of steric hindrance on microchannel substrate and immobilization of the capture ligand on magnetic beads. The targets captured on magnetic beads can be isolated under the magnetic field.[221 222]

On-chip blood plasma separation unit: Testing blood in POC settings is much more challenging than saliva, urine and buffer. Whole blood consists of ~55% plasma as well as ~45% blood cells and platelets.[223] Blood cells may cause severe interference during testing. Therefore, plasma is typically separated from whole blood prior to testing. In a central laboratory, plasma separation is processed by centrifuge and other lab-based equipment. However, such large-scale equipment is unavailable in POC settings, and is not a choice for laypersons. Hence, plasma separation is typically performed *in situ* by an on-chip unit in microfluidic devices using active or passive methods.[196, 224, 225] Active separation methods include centrifugation, dielectrophoresis and acoustic wave (Figure 15). Centrifugal separation, which utilizes difference in mass density between blood cells and plasma, was used in a compact-disk (CD) microfluidic device (Figure 15a).[226] By varying the disk rotation speed, the separated plasma was subsequently divided into smaller samples of equal volume to perform multiple testing simultaneously. Figure 15b shows plasma separation by acoustic standing waves, in which blood cells were driven to the pressure nodes in the standing wave field. Acoustic microstreaming is usually observed, and air bubbles oscillate under the acoustic field. As shown in Figure 15b, blood cells were trapped in the microstreaming vortex at a certain frequency while plasma flowed downstream.[227] Figure 15c demonstrates a dielectrophoresis process, in which the polarization forces were formed in a non-uniform electric field to separate the suspended particles from fluid. Blood cells have dielectric properties different from proteins and small molecules, and can be forced to move in the microchannel. As shown in Figure 15c, blood cells were trapped in the dead-end branches and left blood plasma in the middle of the channel.[228]

Filtration is a common passive separation method, which is based on size exclusion effect to impede cell movement. Pillar-type, grating-type, weir-type microchannels, packed-bead column, and filter membranes have been explored for plasma separation in microfluidic devices.[225, 229–231] Ji *et al.* compared four types of filtration structures, including weir-type, pillar-type, cross-flow and membrane filter (Figure 15d).[229] It was found that the cross-flow

filter showed the highest efficiency in separating white blood cells from red blood cells in whole blood. However, blood cells could block the microchannels in these filters, limiting continuous operation. Hence, other passive separation methods such as hydrodynamic flow and capillary pumps have been exploited. Hydrodynamic flow is based on the Zweifach-Fung bifurcation law that cells prefer to the channels at a higher flow rate, leaving plasma in the channels at a lower flow rate.[232, 233] Both blood cells and plasma keep flowing in the microchannel, thus such devices can work longer time without blocking. For example, Yang *et al* fabricated a "Y"-shaped channel with asymmetric flow rate ratio to separate plasma.[234] Heath's group designed a comb-liked channel to direct plasma skim into the high-resistance branches (Figure 16b).[235] By utilizing the Zweifach–Fung bifurcation effect, Heath's group further increased efficiency of plasma separation with inertial forces.[236] This method permitted direct separation in the same channel without skimming to other channels, leading to a larger proportion of plasma. Natural sedimentation is quite slow. The separation process will stop once the sediment gap is full of cells. To accelerate this process, Maria *et al.* have combined the hydrodynamic effects and the sedimentation to separate 2 μL of plasma from 10 μL of whole blood with 99.9% separation efficiency within 15 min.[237] In Figure 15e, Liu *et al.* combined sedimentation and membrane filtration into a plasma separator.[238] It took less than 7 min to extract about 275 μL plasma from 1.8 mL of whole blood. As a result, HIV virus was measured in the plasma matrix.

Digital microfluidic modules: Digital microfluidics (DMF) has been developed to precisely manipulate small quantities of liquid reagents in microfluidics.[239] Following the electrowetting-on-dielectric principle, continuous liquid can form picoliter-to-microliter droplets due to change in the surface wettability (hydrophobic vs. hydrophilic) of discrete insulated electrodes laid out close to each other.[240–242] Under the electric field, each droplet with different inclusions (targets, detection and capture compounds) can individually move, split, merge and dispense within a short period of time, realizing sample transport, mixing and separation.[240, 243] Digital microfluidics can also reduce sample consumption and avoid cross contamination besides their own merit of low power consumption.[239] For instance, in a digital microfluidic device, the bottom of microfluidic channels was made of glass. An array of discrete ITO electrodes was deposited onto the glass substrate; the ITO electrodes were then completely covered with dielectric material (SU-8/Al_2O_3). Subsequently, a hydrophobic layer was coated onto the surface of dielectric material. The dielectric material served as a spacer between the top hydrophobic layer and the underlying ITO electrode. Without an applied electric field, the top surface layer was hydrophobic. When applying an electric field onto an ITO electrode, the top surface layer became polarized, showing a hydrophilic feature.[244] Droplets were consequently created on the parallel substrates and transported to the target area to function as a fluorescence immunoassay. In this digital microfluidic device, magnetic beads linked with the capture antibody were mixed with sample droplets containing the protein analytes under electrowetting force, followed by incubation for capturing analytes on the magnetic beads. These magnetic beads can be extracted under the magnetic field and washed with buffer prior to fluorescence detection. Compared with conventional ELISA that requires at least 50 μL of a sample volume, this digital microfluidic device required only 520 nL, which made it possible to sensitively test a

rare sample volume (5–10 μL) from fertilization *in vitro*. The total duration was shortened to less than 40 min for multiplexed detection of protein biomarkers.

4.2.2 Integration of fluorescence and SERS sensors into microfluidic platforms—

Microfluidic devices can pretreat, transport, and control liquid flow, which provide attractive platforms for integration of fluorescence and SERS sensors to achieve POCT.[235, 245, 246] Such a technology combines advantages of fluidics and optics, thus is called optofluidics. Signal transduction in optofluidic devices is similar to that in sensors as illustrated in Section 3. The major difference is that optofluidic devices just require simple operation or can realize automation in mixing of sample and reagents, incubation, washing, separation, preconcentration and detection while the sensors, which are described Section 3, typically require manually operation of these steps by trained personnel. Herein we highlight the design and applications of fluorescence and SERS optofluidic devices in protein and nucleic acid detection.

Detection of proteins with optofluidic devices: Figure 16a shows a typical example of optofluidic immunoassay where the liquid sample, the Raman dye-labelled Au nanoparticles with detection antibodies, and the magnetic beads with capture antibodies along with the carrier oil were externally injected into three microchannels, respectively.[218] All liquids were fully mixed as the microdroplets passed through the winding channel, followed by the formation of sandwich magnetic immunocomplexes. These complexes were then separated and concentrated by a magnet. At the end of device, the Au nanoparticles linked to magnetic bead were aggregated, leading to enhanced SERS signals. This device has achieved a LOD (0.1 ng/mL) toward prostate-specific antigen (PSA) detection in serum. Like this device, aggregation of plasmonic nanoparticles in a microfluidic channel was commonly used for SERS transduction in optofluidic devices, which can be realized with other approaches such as micro-nano channel junction and nanoporous silica microspheres besides magnetic field.[247] However, the aggregation methods involve a lot of reagents in the device, which bears a burden on storage, shipping and operation. A different method is capture of analytes into a detection substrate on the bottom of microfluidic chamber. In this way, the SERS or fluorescence probes are *in situ* immobilized onto the detection substrate.[248–250] Heath's group has reported an integrated microfluidic system patterned with antibody barcode arrays as the multiplexed detection substrate (Figure 16b).[235] After a finger-prick blood sample was loaded onto the optofluidic device, plasma was quickly separated via the Zweifach-Fung effect. Different antigen biomarkers were then captured onto different barcode detection zones by forming the sandwiched configuration of the capture antibody-antigen-detection antibody labeled with fluorescence probe. Such *in situ* immunoassays can detect multiple proteins simultaneously.

Detection of nucleic acids with optofluidic devices: When the level of nucleic acids is high, nucleic acids can be directly detected using optofluidic devices; and the structure of devices is similar to that of optofluidic immunoassays. For example, Qi *et al.* have reported an "*in situ*" measurement of nucleic acids using the molecular beacons immobilized on the nanoporous gold disk inside the PDMS microchannel.[248] When targets flowed through the gold disk substrate, they were hybridized with the molecular beacons via base pairing,

generating fluorescence signals on the detection zone. However, in most cases, the level of nucleic acid is very low in samples. For example, the serum level of DNA in HIV patients within the first week of infection is as low as 50–1,000 copies/mL. It is very difficult to directly measure such a level of nucleic acids. Hence a nucleic acid amplification unit needs to be included into an optofluidic POCT device besides a detection unit.

A variety of nucleic acid amplification methods, such as polymerase chain reaction (PCR) and isothermal amplification, have been exploited in microfluidic devices to amplify signals.[251] Especially, digital PCR (dPCR) is a promising high-throughput approach.[252] Amplicons are generated exclusively from a single DNA template in large-scale multiple diluted samples, converting fluorescent signals into linear and digital signals. Digital PCR is generally integrated into microfluidic systems in the form of droplets or integrated flow circuit chip. For example, a slipchip was fabricated with two plates etched with wells and ducts (Figure 17a).[253] In the assembly of two plates, the elongated wells allowed for a continuous flow path to transport reagents into each reaction chamber. When the plates slipped, the misaligned channels and ridges broke off the flow path to obtain droplets. This chip with 1280 wells can achieve 1280 droplets and each of them contained ~2.6 nL of reaction solution, thus is able to perform single-copy PCR assay. Although PCR or digital PCR technology shows high sensitivity and accuracy in detection, 2~3 hours of thermal cycles cannot meet the POCT need. In contrast, isothermal amplification is relatively simpler and has shorter duration, which is suitable for microfluidic systems.[254, 255] For example, a centrifugal microfluidic chip was integrated with the recombinase (RAA)-aided amplification unit and the CRISPR/Cas12a detection unit[256] After centrifuging, the loaded sample was mixed with preloaded RAA-Cas12a reagents, followed with isothermal nucleic acid amplification at 37 °C.

Lysis and/or extraction of nucleic acids is sometimes required prior to detection. In this case, a lysis/extraction unit needs to be added into optofluidic devices so that nucleic acid tests can be done in POC settings. One of common methods is chemical lysis, where lytic agents are mixed with sample liquid in microchannel to disrupt cell membrane.[257] For example, ammonium chloride is capable of red blood cell lysis; guanidinium thiocyanate and guanidinium chloride are used to disrupt membrane proteins; lysozyme works on the bacteria wall.[257, 258] Sethu *et al.* performed lysis by sandwiching whole blood with a lysis buffer on both sides.[259] The mixture passed through a long serpentine channel to achieve full lysis. Besides chemical lysis, physical lysis is also common, including mechanical lysis, electroporation lysis, thermal lysis, laser lysis as well as sonication lysis.[260, 261] Kim *et al.* performed mechanical lysis with ZnO nanowires patterned in a microfluidics device.[261] The ZnO nanowires were characteristic of high aspect ratio and sharp tips, which teared the plasma membrane and released nucleic acids but held cells. After lysis, nucleic acids may need to be extracted and separated for downstream amplification/detection. This can be done via micro-solid phase extraction, electrostatic interactions, nanoporous membrane filtration, or magnetic bead separation.[262,263] Micro-solid phase extraction and magnetic bead separation technologies are commercially available for nucleic acid extraction.[264] In microfluidic devices, silica micro-pillars or silica beads were built in the microchannel to perform micro-solid phase extraction.[265] The negatively charged nucleic acids can bind to silica in a high ionic strength buffer, followed by washing with a non-polar solvent to

remove other biological components. These nucleic acids were then eluted with a low ionic strength solution.[266]

"All-in-one" microfluidic devices are desirable for nucleic acid testing in POC settings, that is, combing lysis, extraction, amplification and detection modules in a single microfluidic chip.[265, 268] Figure 17b shows a typical example, where the self-contained microfluidic cassette can perform separation, amplification, and detection of nucleic acids. It employed the miniaturized linear motors to control fluid flow and valves.[267] All the control units such as motors, heater controllers, micro-vacuum pump, and a liquid trap were packaged into a portable box as an analyzer. Before introducing sample into the mixing chamber, the sealing layer was removed for engagement of the connecting film. The cassette was then inserted into the analyzer to effectuate preprogrammed process operation, including lysis with a prestored lysis buffer, extraction through the silica membrane, collection of pure nucleic acids with an elution buffer, amplification in the PCR chamber and detection in a lateral flow strip. This integrated system was successfully used for monitoring DNA of bacteria (B. Cereus) and RNA of HIV, and it detected 1000 pathogen particles in the sample. In addition, the centrifugal microfluidic CDs are well-known "all-in-one" devices for nucleic acid testing. Stumpf *et al.* have designed a LabDisk with the pre-stored reagents.[246] By controlling the rotational frequencies of the chip and using a magnet, a sample containing influenza H3N2 virus was sequentially transferred to each chamber and mixed with specific reagents. After the sample was mixed with the lysis buffer, nucleic acids were released and bound with the functionalized magnetic beads using a binding buffer. These magnetic beads were subsequently mixed with an elution buffer under magnetic field to extract nucleic acids. Subsequently, nucleic acids were centrifuged into the specific compartments to conduct reverse-transcript PCR, and to read fluorescence signals.

Moreover, the electric field gradients were used for preconcentration, purification, mixing, and acceleration of reactions among sample and reagents.[269, 270] For example, the electric field gradients were formed using isotachophoresis (ITP), which utilized a low-mobility trailing electrolyte (TE) buffer and a high-mobility leading electrolyte (LE)[271]. Under an electric field, TE and LE ions can ensure target sample ions focus with the electro-migrating LE-to-TE interface. In this design, SARS-CoV-2 viral RNA and host DNA from the lysed samples of COVID-19 patients were extracted and preconcentrated in ITP, leaving impurities, proteins and other inhibitors. After loop-mediated isothermal amplification (LAMP), the electric field gradients in ITP were used to control and confocus Cas12–gRNA enzymatic reaction. Such ITP-based nucleic acid device exhibited the test time down to 30 minutes.

4.3 Passive microfluidics

Active microfluidics usually uses external syringe pumps or pressure pumps, which provide great flexibility in designing the structure of microfluidic devices, selecting different liquids, and controlling liquid flow in a well-tuned manner. However, the active microfluidics systems are relatively expensive and large, and require a lot of steps to operate. Therefore, there is an incentive to develop passive microfluidic devices, in which the "built-in" micropumps are used to drive liquid flow to realize self-powered fluidic system, eliminating

the use of external pumps and the associated electronic controllers. Although there are some constraints on regulating liquid flow and realizing sequential operation, passive microfluidic devices are attractive for POCT because they are relatively inexpensive, compact, and have relatively simple structure. Lateral flow is the dominant form in passive microfluidics. Therefore, this section is focused on lateral flow devices that are divided into two different types: (i) plastic-/glass-based lateral flow devices, and (ii) paper-based lateral flow assays.

4.3.1 Plastic-/glass-based lateral flow devices

Basic structure of lateral flow devices: In lateral flow devices, fluids flow almost horizontally along the relatively long microchannels that are divided into different functional zones.[275] It can consecutively or programmably perform sample handling and analyte detection as fluids flow to different functional zones. Figure 18a shows the basic structure of lateral flow device.[272] It contains four main functional zones, including a pretreatment unit, a detection chamber, a fluid resistor and a “built-in” pump. A liquid sample is initially loaded into the pretreatment unit, and fills the pretreatment unit, the detection chamber as well as the fluid resistor sequentially, finally reaches the “built-in” micropump. The resistor is used to adjust the flow rate, and to optimize the incubation duration for fully mixing or reactions of reagents and analytes.[221, 273, 276, 277] In addition, a sample pretreatment unit may need to be placed on the upstream of the detection zone to perform separation or purification. To better regulate the separation and purification process, an additional “built-in” micropump may be added into the pretreatment unit.

“Built-in” micropumps: “Built-in” micropumps are used to drive liquid flow in passive microfluidic devices, and designed based on different mechanisms such as capillary forces, air transfer (solubility or permeability), diffusion and osmosis pressure, magnetic field, electrophoresis, electroosmosis, electrowetting and etc..[273, 278–280] The first two mechanisms are most popular. The capillary pumps drive flow via capillary forces, which are generated by interfacial tension. Once the device is dull of liquid, capillary pumping will stop. The flow rate can be regulated by surface properties, size and shape of microstructures in a micropump, the distance between different pumps, as well as fluid viscosity.[281, 282] Figure 18b illustrates various microstructures in capillary pumps. Line-shaped microstructures are fabricated with a round periphery to reduce the occurrence of fluid pining.[273] The fluids flow in both vertical and horizontal directions, and are modulated by the dimension of lines and the gap between neighboring lines. Zimmermann *et al.* fabricated a vertical line-shaped capillary pump, and found that the 15 μm-sized lines exhibited the highest flow rate.[273] However, such a microstructure showed a random filling front, which can be altered into a straight filing front by rotating the microstructure by 90°, namely “parallel line”. In addition, this pump was designed as gradually increasing lateral dimension from the entrance of the pump, which can prevent from the capillary pressure difference in the connection part to make fluid efficiently flow to the capillary pump. Some capillary pumps exhibit an interlocked microstructure. For example, the rounded hexagons-shaped pump can achieve uniform flow rates due to the inhibited fluid pinning. Furthermore, the tree line-shaped capillary pump has been designed with branched filling paths separated from the main flow region (Figure 18b).[273] Such a structure can program sequential filling flow through generating different capillary pressures of the branched paths.

This “tree-line” pump may suffer from a decrease in flow rate as fluids flow along each branch. Gradient surface wettability can solve this problem by moving spontaneously toward more hydrophilic area owing to contact angle hysteresis.[283]

Pneumatic micropumps are also commonly used in passive microfluidic devices, in which pumping is realized through gas generation or storage of vacuum pillars inside microchannels. Zhu *et al.* fabricated a hydrogen generator using platinum-black to catalyze ammonia borane solution in a microchannel.[280] The generated hydrogen bubbles pushed the liquid flow along the channel, and the velocity of liquid was regulated by the gas removal rate at the gas outlet.[279] Although this technology could achieve self-circulation by collecting hydrogen bubbles to add fresh reactants, it is quite difficult to ensure stable fluid flow; and the chemical reaction may be disturbed when loading sample liquid or detection probes. Vacuum-driven microfluidics provides an alternative method utilizing gas solubility and permeability of PDMS.[274, 278, 284] When it is degassed, the formed negative pressure forces fluid to flow from the inlet to dead-end microchannel. Compared with capillary pumps, surface treatment is typically not required in vacuum-driven microfluidics. However, it is challenging in keeping a constant flow rate due to a gradual decrease in the pressure difference with prolonging time. In this case, prolonging vacuuming time or changing channel patterns was proposed to mitigate this problem. Specifically, multiple vacuum pillars were introduced into microchannel for continuous flow control (Figure 18c).[274]

Purification/separation modules: Filtration, capillary pumping and hydrodynamic flow are commonly used for purification/separation in passive microfluidic devices. Hydrodynamic flow may combine with filtration and capillary pumping to improve the separation efficacy. Maria’s group designed a vertical cylindrical with gradient hydrophilicity as a hydrophobic patch for blood plasma separation.[237] The central portion of the vertical cylindrical was hydrophobic while both sides of the well as well as their connected two parallel channels were hydrophilic. As blood flowed through the bottom hydrophilic microchannel and was elevated along the vertical cylindrical by capillary action, the capillary force decreased due to the hydrophobic patch near the central part, slowing down the flow. The blood cells in the sample subsequently tended to be deposited because of their higher density while plasma was lifted up at a higher velocity because of its lower viscosity. Ultimately, the separated plasma flowed into the upper channel for analyte detection. Similarly, a cyclic olefin copolymer was coated with a super-hydrophilic surface by the layer-by-layer assembly technique. Thus, the asymmetric capillary forces were used for blood plasma separation.[285] In addition, vacuum pillars were designed for automatic blood plasma separation without showing hemolysis. A slant capillary valve led the blood flow to the vacuum pillars. As a result, blood cells were trapped while plasma flowed into the separation channel.[284]

Integration of fluorescence or SERS units: Integration of SERS or NIR fluorescence sensing units into passive microfluidic devices is appealing for POCT. Gao *et al.* has incorporated a SERS sensor into a polydimethylsiloxane (PDMS) lateral flow chip for monitoring prostate-specific antigen biomarkers (Figure 19a).[221] Driven by capillary forces, the liquid sample, the SERS probes conjugated detection antibodies and the magnetic beads

linked with the capture antibodies were loaded from three different inlets and fully mixed in the winding-shaped channel due to the chaotic advection effect. The sandwiched structure was formed via the antigen-antibody interaction, and then purified by applying a magnetic field onto the magnetic beads. The SERS probes linked to the targeted antigen was related to the level of the analyte. The whole process was finished within 5 min. This integrated device achieved a LOD of 0.01 ng/mL in a human serum. Additionally, a blood plasma separation unit and a fluorescent hairpin molecular beacon were integrated into a vacuum-driven microfluidic chip for detection of thrombin in whole blood (Figure 19b).[274] In this device, blood cells flowed into the vacuum microchambers while plasma was driven to a plasma chamber, where the molecular beacons with a quenched fluorophores were stored. In the presence of thrombin, the molecular beacon opened the loop of the hairpin, pushing the quencher away from the fluorophore, and turning on fluorescence.

4.3.2 Paper-based lateral flow assays—In a typical Paper-based Lateral Flow Assay (PLFA), which is also called Paper-based Lateral Flow Strip (PLFS), a porous nitrocellulose paper membrane provides the main microfluidic channels in a test strip; and microstructured polymer, sintered polymer, glass fibers as well as other materials, more or less, are incorporated into the test strip to realize different functions. In such devices, liquid flow is driven by capillary forces.[286, 287] PLFS are of particular interest to POCT because of their low-cost, easy operation on-site, and relatively simple manufacturing processes. The home pregnancy test strip, which detects hormone in urine, is a typical example of such devices. Owing to success of home pregnancy test, this type of devices is sometimes called Lateral Flow Tests (LFT) Strips. Rapid development of this technology has expanded its detection scope to a wide range of analytes such as proteins, nucleic acids, small molecules, metal ions and etc.. If antibodies are employed as the molecular recognition elements, it can also be called Lateral Flow Immunochromatographic Assay (LFIA).

Basic structure and principle: Figure 20a shows basic structure of PLFS.[67] It mainly consists of a sample pad, a conjugated pad, a nitrocellulose microfluidic membrane, an absorbent/wick pad, a control line and one to three test lines/zones. These pads/membranes are connected to each other with small overlaps to ensure continuous liquid flow from the sample pad all way to the absorbent pad. The sample pad is usually made of cellulose, woven meshes or filtration matrices to retain high tensile strength after wetting. The sample pad may be treated with dry pH regulator to standardize the buffer condition of the sample liquid.[286, 288] The conjugate pad should prevent from non-specific binding so that detection probes can be released upon wetting by the liquid sample, and analytes would not be held there. Hence, glass fibers, cellulose and polyester with high bed volume and low non-specific binding are suitable for the conjugate pad to store a large number of probes and release them quickly as liquid flows through.[289] The nitrocellulose membrane is enriched of amine group, which exhibits strong binding to antibodies or other types of bioreceptors, and surface-modified with surfactant or other reagents for prevention from non-specific binding. It also has tunable wicking properties to regulate capillary flow. This absorbent pad should have a sufficient volume so that it is not full even after the whole process is complete. Complete filling or overloading of the absorbent pad will stop the lateral flow of liquid in

the whole strip, and even cause the back flow or liquid accumulation on the nitrocellulose membrane, inducing the background noise on the test line.

Integration of SERS into PLFS: Traditional PLFS usually employ gold nanoparticles as the colorimetric transducers and have achieved huge commercial success in home pregnancy testing in POC settings. Colorimetric PLFS can be read out by human eyes without need of any instrument, and used for qualitatively measurement of a high level of analytes in water, buffer, saliva and urine. But they are unable to quantitatively measure a low level of analytes due to their low sensitivity. Especially, when PLFS are applied to plasma, serum or whole blood, they suffer from severe interference from sample matrices. One of major reasons is that strong red wine color of hemoglobin in such samples is overlapped with the color of gold nanoparticles on the test line. As described in Section 2, NIR fluorescence and SERS fall into the biological transparency windows, and are read out by portable readers. Thus, NIR fluorescence or SERS-based PLFS have a great potential in quantitative measurement of trace analytes even in complex sample matrices such as plasma, serum or whole blood.[1, 67, 290]

Many SERS probes are made by directly attaching Raman dye molecules to bare metal nanoparticles. Such SERS probes are unstable and easily aggregate in liquid with high ionic strength.[44] Hence, Wu's group has designed a sandwich-structured SERS probe, in which Raman dye molecules are sandwiched between a plasmonic metal core and a thin SiO_2 outer shell, which exhibits excellent water solubility and stable in blood sample matrix.[44,64] His team also compared the SERS enhancement factors of Au nanosphere, nanorod and nanostar and found that the Au nanostar contributed a lot of "hot spots", achieving the highest SERS enhancement.[44] The gold nanostar@Raman reporter@silica sandwich SERS probes were incorporated into a PLFS to measure neuron-specific enolase (NSE), a traumatic brain injury (TBI) biomarker, in clinical blood plasma, achieving a LOD of 0.86 ng/mL, which was three orders of magnitude lower than that of colorimetric PLFS (Figure 20a).[67] In order to further enhance SERS signals, a gold nano-pyramid array chip was integrated into the detection zone of PLFS (Figure 20b).[291] By covering the inorganic Au nano-array substrate with a surfactant bridge, the conjugate of SERS probes and analytes can flow smoothly throughout the chip. The "hot spots" formed between the gold nanostars in SERS probes and the gold nano-pyramid array created a hierarchical 3D plasmonic field, which greatly enhanced the SERS signals and achieved a LOD down to 5.0 pg/mL toward the TBI S-100β biomarker in blood plasma. This portable SERS-PLFS system showed a comparable LOD with ultrasensitive ELISA assays but much shorter assay time (~30 min for PLFS vs. 2 h for ELISA). Furthermore, Wu's group has integrated a blood plasma separation unit into a SERS-PLFS following the principle of salt-induced aggregation of blood cells (Figure 20c).[292] Such a SERS-PLFS have directly detected carcinoembryonic antigen (CEA), a cancer protein biomarker, in a drop of whole blood (30 μL) at a LOD of 1.0 ng/mL. This portable "all-in-one" SERS-PLFS system can serve as a POCT tool for testing finger-prick blood samples, assisting *in vitro* diagnostics (IVD) in resource-limited settings. This SERS-PLFS can be adapted easily to detect other protein biomarkers in blood by replacing antibodies.

Integration of fluorescence into PLFS: Fluorescent organic dyes and semiconducting quantum dots (QDs) have been used as fluorescent probes in PLFS.[288, 293–295] Organic dyes usually suffer from low quantum yield, photobleaching and blinking/quenching. To avoid such problems, QDs have been explored in PLFS. The PLFS integrated with the dsDNA-functionalized QDs was developed to measure HIV-DNA in human serum.[296] However, the small size of QDs limits their conjugation with antibodies, especially for proteins over 100 kDa due to the steric effect. In addition, binding with large antibodies would possibly change surface properties of QDs and even cause instability in aqueous solutions. Macromolecule-coated nanobeads were thus introduced to not only stabilize QDs during detection but increase fluorescence intensity in each entity. For instance, the dual-color CdSe/ZnS–COOH QDs were immobilized onto SiO_2 nanoparticles via polyethyleneimine (PEI)-mediated electrostatic adsorption, and conjugated with antibodies.[293] Such a fluorescent PLFS was used to quantify two sepsis biomarkers human serum simultaneously, namely procalcitonin (PCT) and C-reactive protein (CRP) (Figure 21a).

FRET is of particular interest to PLFS because it can reduce the background signals. A quencher can either “turn-on” or “turn-off” fluorescence.[295, 297] For example, an immunoassay PLFS utilized FRET to detect carcino embryonic antigen where fluorescein isothiocyanate (FITC)-labeled antibodies were initially pre-immobilized onto the test zone of PLFS.[297] When analytes were present, the Au NPs functionalized with detection antibody were brought in proximity to the fluorescent dye via formation of the classic sandwich structure. Thus, fluorescence of FITC was quenched by Au NPs via FRET. In addition, the “turn-on” FRET PLFS was developed for measurement of fumonisin mycotoxins based on the competitive mechanism (Figure 21b).[295] In this design, the CdSe/ZnS QDs functionalized with antigen molecules were coated on the detection line of PLFS where the metal NPs with antibody stayed close to QDs via the antigen-antibody interaction, keeping quenching of QD fluorescence prior to detection. When analytes were present on the test line, they formed a complex with the metal NPs, which pushed the metal NPs from QDs as fluid flows, turning on fluorescence of QDs.

Engineering PLFS toward POCT - “On-strip” blood plasma separation: It is challenging in enabling testing of finger-prick blood samples with PLFS in POC settings. A promising route is to combine “on-strip” plasma separation and NIR fluorescence or SERS into a single paper-based microfluidic strip to create an “all-in-one” device. Filtration is a common approach for “on-strip” plasma separation in PLFS. Filter membranes with pore size smaller than 2.5 μm have been placed in the sample pad to block blood cells.[224, 298,299] However, such small pores hinder flow of plasma through the membrane. Hence, various agglutination reagents, such as agglutination antibody, salt and chitosan, have been used for surface-modification of large pore membranes to induce aggregation of blood cells.[291, 300, 301] The aggregated blood cells are too large to pass through the membrane while plasma can do.[230] For example, an assembly of three-layer filtration membranes was treated with salts and then integrated into a SERS-PLFS.[291] The first layer was functionalized with salts, which impaired the electric double-layer of blood cell surface, causing deformation and aggregation of blood cells due to the osmotic pressure. The

surfactant coated on the second layer accelerated liquid flow to the third layer where salts held the residual blood cells. Such an “on-strip” plasma separation unit enabled the PLFS to directly measure whole blood samples.

Engineering PLFS toward POCT – Tunning fluid: Flow rate is an important factor governing the performance of PLFS, which can be regulated by designing different path patterns and lengths.[289, 302] Computational simulation was combined with experimental analysis to investigate the transport processes in simple two-dimensional geometries and assisted optimization for sequential reagent delivery for sample pretreatment and analysis.[303] In addition, valves were constructed for flow control and reagent loading.[204, 299, 304, 305] Paraffin wax, PDMS droplets or dissolvable reagents (e.g., sugar) were deposited on the paper surface as hydrophobic barriers to control flow direction. Surfactant treatment can accelerate flow.[289, 305] To slow down flow, a cellulose pad was placed on the upstream of the test line as a shunt for time delay, tunning flow rate by varying its size and number.[305] Apart from those passive methods, active valves were built into PLFS by folding, stacking or cutting papers to initiate or stop flow.[304, 306,307–309] For example, a paper-based device contained three parts and each part was loaded with different reagents. The loaded liquid can move to other parts by folding the specific part.[310] Inspired by electrowetting on dielectrics, the “on-strip” electrical valves were fabricated by inkjet-printing and spraying technology on a paper-based device. The dielectric surface in the valve can be switched from hydrophobicity to hydrophilicity under an applied bias. Thus, the ionized sample solution can stop or flow by the external bias.

Engineering PLFS toward POCT – Reshaping overall structure: Besides the basic/classic structure as shown in Figure 20a, a lot of varieties have been developed to either improve performance or realize new functions. An intriguing example is the origami paper-based devices that transfer and mix sample and reagents by folding papers.[2, 310, 311] As shown in Figure 22a,[310] an origami device was composed of three layers where the target DNA, a short ssDNA with a quencher (Q1) and a long ssDNA with fluorophore (F1) were loaded on each layer, respectively. Because Q1 was shorter than the target DNA, the target showed priority to hybridize with F1 compared with Q1, and the remaining F1 strands were complementary to Q1. The amount of target DNA was proportional to the intensity of fluorescence.

Additionally, nucleic acid amplification sometimes needs to be conducted at a relative high temperature. For example, loop-mediated isothermal amplification (LAMP) of nucleic acids is typically performed at around 72 °C, which is difficult to be carried directly on paper surface. Hence, a paper-based strip was combined with microfluidic PDMS to create hybrid structures, which not only reduced sample consumption but also enable more functions.[308, 309, 312–314] Phillips *et al.* have modified the sample pad of PLFS to make a LAMP unit for detection of HIV-1 virus in blood.[315] The HIV-1 viral particles were separated by a size-selective filtration membrane, and migrated in a buffer solution to a polyether sulfone membrane preloaded with the LAMP reagents to perform LAMP at room temperature. The amplicons generated by fluorescence-labeled primers flowed along the downstream paper strip, finally captured on the test line for fluorescence recording. The

whole process was finished within 90 minutes, achieving a LOD of 2.3×10^7 copies/mL in whole blood. Recently, Cooper's group developed multiplex microfluidic diagnostic platform using hybrid devices.[2] An additional example of hybrid device was shown in Figure 22b.[2] The origami structure, plastic microfluidic modules and paper-based lateral flow strips were combined to create a hybrid device for detection of malaria in blood. Liquid sample was pretreated with cell lysis. The released DNA was captured onto magnetic beads, and then loaded onto the sample zone of origami paper part where excessive buffer and other residues were removed by capillary force of waste panel. The DNA bounded with the magnetic beads were distributed into three spots through distributing channels and transferred into different LAMP chambers. In each chamber, LAMP reaction proceeded independently by adding different primers labeled with fluorophores. After that, the finger pumps were used to push liquid to flow to the paper test strips. As a result, it can detect two different types of malaria DNA together with the positive and the negative controls simultaneously.

5. NIR Fluorescence and SERS Imaging of Live Cells and Tissues

NIR fluorescence and SERS take advantages of biological transparency windows, feature the extended penetration depth and the reduced interference from cells and tissues, and they are non-invasive techniques. Therefore, they are finding increasing applications in real-time imaging of internal processes living cells, tissues and organisms for diagnostic or biomedical research. This section gives an overview of the instruments, optical probes, imaging activation, and applications.

5.1 Instruments

Fluorescence microscope for *in vitro* imaging: Conventional optical microscopes mainly comprise a light source, a condenser, an objective and an eyepiece.[316, 317] The light from the light source is concentrated by the condenser, leading to a cone of light with uniform intensity to passes through the specimen. After that, a primary magnified image is produced by the objective as well as a secondary magnified image by the eyepiece. The total magnification is equal to objective magnification times eyepiece magnification. Conventional optical microscope has been developed to a large family of commercial products, including brightfield, differential interference contrast, phase contrast, Hoffman modulation contrast and polarized light microscope.[318] Different from these conventional optical microscopes, fluorescence microscope relies on the condensed light from the light source passing through the objective to the specimen; and the emitted light by the specimen will then pass through the same objective to the eyepiece.[319] Given the fact that most fluorophores only absorb a small range of excitation light and their fluorescence emission is quite weaker than incident light, the main research work on fluorescence microscope is to effectively reduce the influence of background light and collect the emission light. Hence, filters are the major means to (i) segregate a defined bandpass of excitation light by an excitation filter; (ii) segregate a defined bandpass of emission light by an emission filter; (iii) segregate the excitation light from the emission light by fluorophores using a dichromatic mirror.[319] By combination of these three filters, condensed light from the source is purified by an excitation filter with most of the nonessential light reflected

back to the source, and then is reflected down by the dichromatic mirror to the objective and reaches the specimen. Non-coherent fluorescence emission passes through the same objective and the dichromatic mirror, followed by filtered by the emission filter to remove the contaminating light including unabsorbed excitation light and light not fully removed by the previous filters, and finally reaches the eyepiece. Apart from the filters, light sources and objectives should be carefully chosen to provide sufficient excitation energy in the required spectrum ranges and gather large amount of emission light, respectively. Light sources include mercury, LEDs and metal-halide lamps.[320] Mercury lamps are the line-emitting arc discharge lamps whose 405 and 546-nanometer lines can overlap Alexa Fluors 405 and 546, while LEDs and metal-halide lamps are suitable for Alexa Fluor 488.[321, 322] The objectives are fabricated with various lens elements such as high light transmission values over large spectrum ranges, and large numerical apertures. It should be noted that water immersion objectives used in live-cell imaging need color correction for compensation of coverslip and temperature variations, while oil immersion objectives used in fixed specimens can reduce light loss due to reflections at the glass-air interface of the objectives. Additionally, imaging experiments should be done in a relative dark room to reduce light disturbance.

Developed from basic fluorescence microscope, confocal laser scanning microscope (CLSM) features controllable depth scanning, serial optical sectioning, spatially filtering, adjustable magnification.[323, 324] The key to success is application of pinholes located between laser source and excitation filter (named light source pinhole), and between emission filter and eyepiece or detector (named detector pinhole), respectively. With the addition of light source pinhole, a point-liked laser is formed and reaches on the specimen. Then the emission fluorescence from in-focus specimen passes through the detector pinhole to the detector. Otherwise, fluorescence from out-of-focus specimen is reflected. Thus, the use of pinhole not only realizes high signal-to-noise ratio but also acquire multiple two-dimensional (2D) images at different depths in a sample, following with reconstruction to form a three-dimensional (3D) image. Especially for uneven samples, depth scanning can collect and integrate serial optical sections into a single image, which help eliminate the out-of-focus imaging. In addition, confocal laser scanning microscope has zoom function that adjust magnification by altering the scanning rate and scanning area of the laser without changing objectives. Given high zoom factor would lead to photobleaching, it is advisable to achieve a balance between zoom factor and imaging. In terms of thick samples, such as embryos and brain slices, confocal microscopy with single-photon excitation is weak in serially scanning in the deeper planes, thus multiphoton microscopy has emerged.[325] Taking two-photon excitation fluorescence microscope as an example, it depends on simultaneous absorption of two photons, followed by non-radiative relaxation and fluorescence emission.[326] It results that excitation wavelength is longer than emission wavelength, which is opposite to the traditional fluorescence microscope. More importantly, NIR excitation light is commonly used in two-photon microscope, leading to deep tissue penetration, low background signal as well as reduced photobleaching. Despite these advantages and commercial application of confocal microscope, the theoretical resolution limit is around 200 nm within the visible light spectrum because of far-field diffraction limit.[327] Fortunately, a series of super resolution techniques and microscopies and has been introduced, such as 4Pi and I^5M, stimulated emission depletion (STED), saturated structure

illumination (SSIM), single-molecule localization and far-field microscopy.[328–331] It is desirable that nanometer-scale can be resolved using a commercial fluorescence microscope in the near future.

Fluorescence microscope for *in vivo* imaging: The main problems faced by *in vivo* imaging are light absorption and autofluorescence of tissues, which can be partially overcome by NIR fluorescence probes. In commercial *in vivo* imaging systems, the basic light path is similar to that in fluorescence microscopes. However, specimens are living creatures, and the optical pathlength in a specimen is much longer.[332] The core of an *in vivo* imaging systems is a charge coupled device (CCD) camera.[333] Upon illumination by light, each pixel creates a charge which is proportional to the illumination intensity. The important parameters of CCD include quantum efficiency and dark current level. Quantum efficiency can be improved by generating back-thinned and back- CCD to increase photon absorption. Dark current level is referred to the charge electrons that leaks into a pixel within an exposure process in the absence of light, which limits the minimal light intensity of CCD detection. Low dark current can be achieved by cooling the CCD camera or introducing a cooled intensifier tube into the system.

In addition, optical fiber-based imaging systems is one of *in vivo* imaging tools, which is referred to fluorescence microendoscopy (FME).[334] The optical fiber in FME can be insert into a tissue in a minimally invasive way, and flexibly maneuvered in the hollow tissue cavities. Various types of optical fibers are used in FME, such as fiber bundle, single-mode fiber, double-clad fiber, multi-mode fiber as well as graded index microlens.[335] For example, a fiber bundle generally consists of ~100,000 individual step index fibers, which are closely packed with a total diameter, ranging from hundreds of micrometers to a few millimeters. Each core is of high-refractive index and serves as a pixel of an image. Because the arrangement of individual fibers in a fiber bundle is relatively maintained at both ends, the intensity of the image can be transmitted in a pixelated form. The fiber bundle can be introduced into basic fluorescence and confocal laser scanning as well as two-photon excited fluorescence microscope. Specifically, each core of fiber bundles could also act as a pinhole in confocal instrument. In a typical FME, the excitation light from light source (eg. lasers, LEDs and lamps) is transmitted to the distal end of the fiber bundle, illuminating the sample. The fluorescence emission light from the sample is then gathered by the fiber bundle, followed by sequentially passing through the objective, the dichroic mirror and the emission filter, and finally reaches a CCD camera.

Raman microscope: Raman signals are in the form of light scattering and commonly built under the confocal model, which consists of a laser source, band pass filters, pinholes, dichroic mirrors, an objective and a CCD camera.[336] Like laser scanning confocal microscopy (LSCM) of fluorescence, out-of-focus Raman scattering light is minimized to increase the signal-to-light ratio with assistance of point-liked scanning. Depth scanning is also applicable in confocal Raman microscope to realize 3D imaging. Taking an advantage of fingerprinting spectrum of a specific Raman-active molecule, Raman microscopes can be used for imaging living cells and tissues even without labeling. And the distribution of chemical species in images can be further analyzed with statistical methods such as

Principal Component Analysis (PCA).[337] In addition, the common excitation lasers, such as 785 nm and 830 nm, fall in a biological transparent window. Thus, confocal Raman microscope could also be used for *in vivo* imaging, but the penetration depth is limited because an objective lens is typically needed.[338] To achieve deeper imaging capability, various types of Raman optical fibers are introduced in confocal Raman microscope for endoscopic use.[337, 339]

Considering the spatial resolution of confocal Raman microscope is limited to the submicron scale, hyperspectral imaging is combined with Raman scattering into a single microscope to perform dual functions. Hyperspectral imaging can enhance the spatial resolution to tens of nanometers. In addition, Raman scattering is incorporated with a scanning near-field optical microscopy (SNOM) because SNOM can reach the nanometer scale resolution. In a single instrument, SNOM can be used to map morphology of a sample and Raman scattering can be used to acquire chemical information.

Recent Raman microscopes are mainly used for *in vitro* imaging for cultured cells and biopsy tissues. The reason is that a sample under Raman microscope needs to be focused within a specific length to the object. It is difficult to collect Raman scattering with a controlled distance under the *in vivo* condition. Also, to obtain a high-resolution image in a large area, Raman microscope should scan the target area sequentially, which is a quite time-consuming process. These drawbacks impede its development in *in vivo* imaging. Different from Raman imaging, fluorescence emission from a sample is much easier to collect from a large-area or a large sized sample.

5.2 Materials for NIR fluorescence probes

The general design and materials of NIR fluorescence probes have been described in Section 2.4. Compared to SERS imaging, there are much more varieties of materials for NIR fluorescence bio-imaging. Hence this sub-section is focused on materials for NIR fluorescence probes. For imaging of live cells and tissues, NIR fluorescence probes require high molar extinction coefficient, high quantum yield, low- even non-toxicity as well as good photostability in an aqueous environment. Especially, *in vivo* imaging requires deep penetration and low background noise. In the past decades, numerous NIR probes have been exploited, which can be classified into three types, namely, organic dyes, nanomaterials and proteins.

Organic dyes: The basic structures of organic dyes contain cyanine, squaraine, rhodamine, 4,4-difluoro-4-bora-3a,4a-diaza-s-indacene (BODIPYs), or porphyrin.[19, 340, 341] Among them, the emission wavelengths of classical rhodamine, BODIPYs and porphyrin dyes are not in the NIR region. Hence, NIR derivatives have been developed by chemical modification to regulate their photophysical properties. For example, NIR rhodamine derivatives can be generated by extending conjugation of the xanthene moiety or replacing the central oxygen atom with other atoms including N, C, S, Si, P, Se, and Tn.[342] Although typical cyanine (Cy5 and Cy7) and squaraine dyes emit in the NIR region, chemical modification is still required to improve their photophysical properties. For example, the emission peak of cyanine dyes can be tuned from NIR-I window to NIR

II window through extending the conjugated structure length or regulating their chemical substitutions.[343] Moreover, traditional dyes suffer from poor water solubility and self-aggregation due to their hydrophobic moieties. When organic dyes aggregate at high concentration, their fluorescence intensity will decrease because of aggregation-caused quenching (ACQ) effect. To mitigate these problems, small hydrophilic groups including sulfonate, carboxyl, carboxylate, amine, as well as maleimide are added to these dyes to increase water solubility. Besides, fluorogens with aggregation-induced emission (AIE) features were exploited by Tang *et al.*[344] AIE fluorogens showed enhanced and stable fluorescence intensity upon aggregation, as well as high photobleaching threshold. Recently, many AIE fluorogens with NIR emission have been developed by introducing hydrophobic π-conjugated bridge into AIE initial fluorogens.[345, 346] Overall, organic dyes exhibit easy processability and good biocompatibility. There are some issues with organic dyes, such as small Stoke's shift, self-aggregation, poor photostability in aqueous medium.

Nanomaterials: Nanomaterials have a great promise in NIR fluorescence imaging, such as quantum dots (QDs), graphene-based nanomaterials, carbon nanotubes as well as halide perovskite nanocrystals.[14, 15] At nanoscale, they can be designed to overcome biological barriers and penetrate cells and tissues. In addition, the optical properties of nanomaterials can be modulated by quantum effects. The emission wavelength depends on the size and shape of nanomaterials. Fluorescent QDs are a class of zero-dimensional (0D) nanomaterials in a typical diameter of 2–20 nm. They exhibit greater photostability and can achieve higher quantum yield than traditional organic dyes, thus enabling long-term imaging with high signal intensity. In addition, they have broad absorption spectra and their emission peaks are tunable and narrow, facilitating multi-component imaging with minimal overlapping.[347, 348] At the early stage, NIR QDs contained toxic elements such as Cd, Hg, Pb and As, which leads to cytotoxicity, limiting their biological applications. To mitigate this problem, core/shell nanostructures are designed by coatinf the toxic core with ZnS, ZnS, SiO_2 or C.[349] Alternatively, some materials with less cytotoxicity are used to synthesize NIR QDs, including Ag_2S and Ag_2Se, silicon and carbon.[350, 351] Si exists in human body in the form of orthosilicic acid and could be efficiently excreted out of body through urine. Thus, Si QDs display relatively good biocompatibility and biodegradability features. Fluorescence emission of Si QDs can be tuned to the NIR-I region by varying the particle size; and they can become water soluble by surface modification. Because the bulk band gap (1.12 eV) of Si is larger than that of PbS and AgS, it is not practical to increase their size for reaching NIR-II emission region. In this case, boron (B) and phosphorus (P) co-doping makes it possible to generate NIR-II Si QDs.

Similarly, biocompatible and biodegradable carbon quantum dots (CQDs) are alternatives to traditional metal-based QDs. Their absorption and NIR emission spectra can aslo be tuned via size control, surface modification as well as heteroatom doping. Furthermore, carbon quantum dots display excitation-wavelength-dependent fluorescence due to the "giant red-edge effect".[352] Hence, they are able to present different fluorescence emission bands in imaging under different excitation wavelengths. Other carbon materials such as graphene oxides and carbon nanotubes (CNTs) have been explored for bio-imaging. Pristine graphene with sole sp^2-carbon atoms do not show fluorescence. Graphene oxides and graphene

quantum dots (GQDs) consist of a mixture of sp^2 and sp^3 carbon atoms, thus they have an opened band gap; and their surface possess carboxylic acid and other moieties that make themselves water soluble. Like carbon quantum dots, free-standing graphene oxides and graphene quantum dots exhibit excitation-wavelength-dependent fluorescence, and they are photostable and biocompatible.

Recently halide perovskite nanocrystals have emerged for NIR fluorescence imaging.[28, 353] Among the vast perovskite family, lead-based halide perovskite (LHP) nanocrystals have attracted great interest due to their high quantum yield. It has been reported that lead-based halide perovskite nanocrystals achieved a photoluminescence quantum yield up to 90% without any post-treatment.[354] Lead-based halide perovskite had a very narrow fluorescence emission band that can be tuned by either compositional or/and size. However, halide perovskite nanocrystals typically contain toxic elements, and may exhibit poor stability in an aqueous solution.

Proteins: Fluorescence proteins (FPs) were initially discovered from jellyfish and corals. Fluorescence proteins and their derivatives have revolutionized many fields of molecular and cell biology. However, most of them exhibit the excitation band in the spectral range less than 610 nm. It is worth noting that Tsien's group reported monomeric NIR fluorescence protein with excitation/emission maxima at 684/708 nm by engineering of bacterial phytochromes (BphPs) of *Deinococcus radiodurans*.[355] Similarly, other NIR fluorescence proteins have been exploited from *Rhodopseudomonas palustris*.[27] Since the chromophore of NIR fluorescence protein is converted from haeme, which is influenced by haeme oxygenase 1. Fluorescence intensity of these proteins in cells could be enhanced via engineered cofactor biosynthesis.[356] In contrast to other NIR probes, fluorescence proteins feature exceptional biocompatibility and biodegradation; and they are widely used in monitoring gene expression, tumor growth, bacterial or viral infections *in vitro* and in *vivo* imaging.

5.3 Signal transduction

For fluorescence or SERS imaging of live cells and tissues, there are three common signal transduction modes/principles: (i) direct imaging with non-targeting optical probes, (ii) imaging with targeting optical probes, and (iii) activatable imaging with triggering modes.

Direct imaging with non-targeting optical probes: Direct imaging is independent on specific binding events to the target/analyte; and a signal is under the "always on" mode. Generally live cells or tissues are stained with fluorescence probes to directly visualize the structures of cells or tissues (e.g., tumor vessels), and to monitor their dynamic changes.[357–359] For example, Dai's group fabricated a NIR-II PbS/CdS QDs for noninvasive *in vivo* imaging of tumor tissues (Figure 23a).[360] After tail vein injection of such QDs into a mouse with xenograft MC38 tumors, the PbS/CdS QDs were circulated over time in vessels. Because of the increasing structural abnormalities and the permeability of tumor vasculatures (enhanced permeability and retention (EPR) effect), these QDs were gradually leaked from vessels and accumulated at the tumor sites, brightening up the whole tumor. Moreover, these QDs could be excreted over 1 month, providing a tool for localizing

tumors and real-time monitoring their dynamic changes. Because inorganic quantum dots exhibit long-term photostability and capability of real-time localization, they are suitable for imaging-guide surgery, especially for surgery resection of brain tumors. Brain tumor margins are irregular and indistinct, and extensive tumor-induced angiogenesis increases risk of irreversible damage. Li *et al.* reported a dual-modality nanoprobe (Gd-DOTA-Ag_2S QDs) together with both MRI and fluorescence imaging functions for highly efficient and precise physical resection of brain tumors[357] After nanoprobes were accumulated at the tumor sites based on the permeability and retention effect, the deep tissue penetration capability of MRI enables the identification the tumor locations. Simultaneously, NIR fluorescence imaging guided the intraoperative resection precisely.

SERS probes without specific targeting moieties can also be used in tumor imaging by utilizing the permeability and retention effect. For example, a PEGlyated sandwiched SERS nanostars with a LOD down to 1.5 fM were successfully used for imaging of premalignant lesions of pancreatic and prostatic neoplasias.[362] In addition, based on “finger-printing” features of SERS spectra, SERS imaging can be directly used for identification of cells and monitoring of molecular evolution in cells or tissues. After the Raman dye-free plasmonic metal nanoparticles entered cells or tissues, the SERS-active molecules in living body, such as proteins with chromophore groups (e.g. hemoglobin, can myoglobin), nucleic acids, metabolites (e.g. lactic acid and glucose), can be detected when they were in proximity with the plasmonic nanoparticles. In the meanwhile, a dark-field microscope was employed to map the position of plasmonic metal nanoparticles in living cells, tracking the SERS signals of characteristic biomolecules at different sites of cells, which can continuously monitor intracellular information (Figure 23b).[361] In order to mitigate the uncertainty and uncontrollability of distribution of nanoparticles in living cells, researchers deposited metal nanoparticles on a solid substrate to form SERS-active substrate.[363] After seeding cells on such SERS-active substrate, biomolecules on cell membrane get close to the substrate, thus obtaining SERS signals of these biomolecules. The SERS images, which are obtained from the cells on plasmonic substrate, can monitor cell state because these biomolecules on cell membrane play a vital role in regulating signal pathway, cell behavior as well as in identifying cell type and condition. The large amount of data generated in a dynamic system can be analyzed by statistical methods such as principal component analysis (PCA) and multivariate curve resolution (MCR).

Imaging with targeting optical probes: In this mode, the signals of probes are under the “always on” mode like the direct imaging mode, but the probe is conjugated with the specific ligands (antibodies or aptamers) as the molecular recognition elements that specifically bind to the targets/analytes through the antibody-antigen interaction or the aptamer-nucleic acid interaction. Compared with direct imaging, this mode can provide more specific information about biological events.[364–366] Furthermore, ligand-assisted imaging could concentrate the optical probes at the targeted sites, leading to higher sensitivity. Ghosh *et al.* have compared the signal intensity of single-walled carbon nanotubes (SWNTs) with the conjugated ovarian tumor-targeting ligands and without ligands.[367] It was found that those with the conjugated ligands showed 10 times higher signal-to background ratio than that of the un-conjugated counterparts. NIR

photoluminescence of single-walled carbon nanotubes fall into the biological transparent window, which endows them with higher sensitivity for imaging-guided surgery, especially for submillimeter tumors. SERS probes are also characteristic of high sensitivity for *in vivo* imaging. For example, a sandwich SERS probe with a polyethylene glycol (PEG) shell was used for imaging of human cancer cells and xenograft tumors in mice (Figure 24).[368] These PEGlyated SERS probes showed not only great stability over a wide range of pH solutions but also high signal intensity. It was observed that SERS intensity of the adsorbed molecules increased as much as 10^{14} to 10^{15} folds when the SERS probe were conjugated with the tumor-targeting ligands.

Imaging with triggering modes: Fluorescence or SERS imaging can be conducted on either “turn on” or “turn off” modes in response to targets, bio-events or their surroundings. Compared with the “always on” mode, activatable imaging is more convenient, accurate and sensitive in imaging with minimal interference by the background signal. In activatable fluorescence imaging, the signal transduction principles are based on various physicochemical processes such as electron transfer (ET), Förster resonance energy transfer (FRET), aggregate-induced emission (AIE) and *etc.*. Signal transduction via ET and FRET is based on donor-receptor interaction. ET can be categorized into intracellular charge transfer (ICT) and photoinduced-electron transfer (PET), which often takes place when the distance between the donor and the acceptor is less than 3 nm, such as chemical bounds and physical absorption. Different from ET, FRET is a relatively long-range energy transfer process up to 10 nm. In addition, AIE process is often used in signal transduction, in which the initial “fluorescence-off” probes are solute or dispersive in the aqueous environment. In the presence of hydrophobic target (e.g., proteins), the “fluorescence-off” probes binds with the target specifically, which induces the aggregation of probes, turning on fluorescence emission.

In activable SERS imaging, the signal trigger is the environment-sensitive Raman reporter. Signal variation of Raman reporters reflects the physicochemical changes in living cells and tissues. For example, 4-mercaptobenzoic acid (MBA), 2-aminothiophenol and 4-mercaptopyridine are pH-sensitive Raman reporters, while indocyanine green (ICG) is a thermosensitive reporter.[369–371]

Fluorescence or SERS imaging can be triggered by various operating parameters (eg. pH, viscosity, temperature) or biomarkers (e.g., small molecules, protein, nucleic acids) in cells and tissues. For example, the pH value plays a vital role in biological processes, such as ion transport, endocytosis and cell growth. In normal physiological condition, the pH value is around 7.2 and 7.4 in the cytosolic and extracellular environment, respectively; and the pH value in lysosomes and mitochondria are approximately 5.0 and 8.0. respectively. Abnormal pH values may reflect pathological conditions, including cancer and Alzheimer’s diseases. For instance, the pH value of lysosomes in the tumor cells becomes more acidic (pH_{ly} 3.8–4.7) than the normal one. Figure 25a illustrates the effect of pH on the ET process resulting from protonation/deprotonation-induced electron distribution.[372] Briefly, a pH-responsive probe was constructed using a heptamethine cyanine dye, which had good biocompatibility and relatively high quantum yield. The NIR fluorophore (heptamethine cyanine derivatives IR783) served as the electron acceptor, and the amine moiety on one

indole ring was the electron donor in neutral pH. When the probe was delivered into lysosomes through an organic anion transporting peptide, the acidic environment protonated the amine groups, triggering fluorescence emission. Visualization of a pH change in cancer cells can localize cancer cells specifically, and guide tumor ablation. In addition, Tang *et al.* have developed a pH-triggered imaging method using the PET process, which strongly depends upon a pH change from 6.70 to 7.90.[373] It was used successfully for real-time imaging cellular pH in living HepG2 and HL-7702 cells. However, it is difficult to achieve a broad range of pH detection in these single-electron transfer modes, especially from acidity to alkalinity, to show the overall pH change in cells. A combinational electron transfer-energy transfer method was thus exploited to create an ICT–PET–FRET probe with dual pH-responsive sites.[374] Therefore, the probe responded to a wide pH range from 4.0 to 8.0 with high sensitivity. It can be utilized not only in fluorescence imaging of the lysosomal pH values with one of the pH sites targeting the lysosome place, but also in therapeutic effect evaluation based on the intracellular pH changes in cells after chloroquine treatment. In addition, taking an advantage of a pH change from normal to tumor tissues, researchers have developed the pH-sensitive imaging and drug delivery to realize imaging-guided surgery. For example, Song *et al.* have labeled a hydrophilic polymer brush, a pH-sensitive hydrophobic brush as well as a Raman reporter on the surface of gold nanoparticle to form SERS-encoded amphiophilic nanoparticles (Figure 25b).[375] These nanoparticles can be further self-assembled into vesicles with the anticancer drugs embedded in the hollow cavity. After tagged with the cancer-targeting ligands on the outer surface of SERS vesicles, these vesicles were successfully bound to the target cancer cells with strong SERS signals due to their assembly structure. Afterwards, the SERS vesicles were transferred into cytosol through endocytosis and the acidic intracellular compartments triggered pH-responsive disassembly of SERS vesicles to form single gold particles. Compared with the SERS vesicles, these dispersed single gold nanoparticles showed much weaker signal intensity. Simultaneously, the embedded drugs were released with disassembly of the SERS vesicles.

Viscosity is one of the critical microenvironment parameters, which is associated with transportation and reactions of biomolecules as well as chemical signals within cells. Viscosity perturbances are caused by diseases and pathologies, such as diabetes, atherosclerosis, cancers and Alzheimer's diseases. As it is an important indicator in disease diagnostics, a series of molecular rotors has been developed to map the cellular viscosity. For example, a molecular rotor, malononitrile moiety, was linked to 4H-chromene groups modified triphenylamine as the NIR fluorophore to form viscosity-sensitive probes. As shown in Figure 25c, in low-viscosity media, after the fluorophore was excited by a proton, the excited electron was transferred into a twisted excited state due to the rotation of the malononitrile group, which reached a non-emissive decay.[376] In contrast, in a high-viscosity media, molecular rotation was restricted, and the ET process was then inhibited, leading to emissive decay of NIR fluorescence. This method was used to identify cancer, which showed higher viscosity than normal tissues, and to evaluate the efficacy of anticancer drugs.

Imaging can be triggered by unique features of biomolecules or reactions, such as hydrophobic property of proteins, chain reactions of nucleic acids, or specific chemical reaction of small molecules. Figure 26a shows images of nucleic acids using the FRET signal transduction and nucleic acid amplification to overcome the problems of intrinsic low-

abundance analytes.[377] First, the target microRNA-21 (miR-21), a crucial tumor-associated biomarker, was recycled via an Exo-III-assisted assay, and the exposed DNAzyme was further partially hybridized with a fluorophore/quencher pair. After experiencing biocatalysis by Mg^{2+} in cells, the fluorophore/quencher pair was cleaved, thus fluorescence of the separated fluorophore was restored. In addition, the base-pairing complementarity can also be used in the intermolecular FRET process. For example, Hwang *et al.* have developed a fluorophore-labeled nucleic acid as an imaging probe whose fluorescence was initially quenched by graphene oxide (GO) via FRET.[378] After the probes were internalized into cancer cells through CD44 receptor-mediated endocytosis, the nucleic acid of the probe was specifically hybridized with the target when encountering the target miRNA, leading to detachment of the probes from graphene oxide and recovery of fluorescence. Figure 26b reveals an AIE imaging process activated by amyloid-β (Aβ) plaques, an important pathological hallmark for early diagnosis of Alzheimer's disease.[379] Initially, the AIE probe was under the "fluorescence-off" state due to hydrophilicity of sulfonate group of the probe. Fluorescence of the probe was turned on when binding to the Aβ aggregates via the N,N-dimethylamino group in the probe.

In cells, there exist a lot of chemically active molecules, such as reactive oxygen species (ROS), reactive nitrogen species (RNS), enzymes and metal ions. Thus, activable imaging can also be triggered by chemical reactions. Figure 27 shows a NIR fluorescence imaging process activated by an alkaline phosphatase (ALP) reaction.[380] Initially, fluorescence of merocyanine was quenched by the modified phosphate group via the electron transfer process. When it came to ALP-positive tumor tissues, the membrane-bound ALP dephosphorylated the phosphate group, leading to emission of NIR fluorescence. In this design, fluorescence imaging was combined with magnetic resonance imaging (MRI) imaging through modification of paramagnetic DOTA-Gd chelate to the probe with a hydrophobic dipeptide liner. After dephosphorylated, the hydrophobic interaction of dipeptide promoted the molecular self-assembly into magnetic nanoparticles.

6. Remarks and Perspective

In summary, further efforts are needed to design and fabricate plasmonic nanostructures to achieving effective coupling of plasmon with fluorescence or SERS to amplify signals. These efforts will include commercialization of plasmonic NIR fluorescence and SERS probes. These probes should be inexpensive, water-soluble, "bright" (strong intensity), stable in storage, shipment and operation, and repeatable from batch to batch.[44] Commercial availability of these plasmonic probes is the key step in boosting application of NIR fluorescence and SERS in POCT and bio-imaging.

Pregnancy test strip is the most successful example of commercial POCT devices. Like pregnancy test strips, most of commercial lateral flow assays are based on colorimetric transduction. Such devices are inexpensive and can be used for rapidly and qualitatively detecting a relatively high level of analytes. However, they suffer from low sensitivity and severe interference from complex sample matrices such blood. In contrast, the NIR fluorescence and SERS microfluidic devices have a great promise in sensitive and quantitative measurement of a low level of analytes in complex sample matrices. However,

such POCT devices typically requires the integration of a complex plasmonic nanostructure into a microfluidic chip in order to amplify NIR fluorescence or SERS signals. Although significant progress has been made in such a direction, it remains large technical barriers in fabricating and integrating 1D, 2D or 3D plasmonic nanostructures into a microfluidic POCT devices.[291]

Today there are a lot of commercial POCT devices based on immunoassays with antibodies as the molecular recognition elements. These immunoassays have been successfully used for detecting illicit drugs, HIV antibodies, biological warfare agents, pathogens and so on. They are typically used for qualitative measurement of analytes in relatively simple sample matrices such as tapping water, river water, saliva and urine. So far, few POCT devices are commercially available for direct and quantitative measurement of analytes in finger-prick blood because whole blood is a much more challenging sample matrix as compared to buffer solutions, water, saliva and urine. Integration of a plasma separation unit and a NIR fluorescence or SERS detection platform into a single microfluidic or paper lateral flow strip is an effective solution to blood analysis in POC settings.[292]

There are few commercial POCT devices for nucleic acid testing. For example, no commercial POCT device are now available for reliable testing of SARS-COV-2 viral RNA in saliva or nasal swab samples in POC settings. One of the reasons is that the levels of nucleic acid biomarkers of interest, such as DNA, RNA and micro-RNA, are typically too low to be detected directly by a sensor. To enable nucleic acid testing in POC settings, both amplification and detection of nucleic acid should be performed in a single lab-on-chip device. In some cases, an on-chip lysis and nucleic acid extraction module also needs to be integrated into a POCT device. In short, nucleic acid POCT devices are complicated and quite challenging. Many researchers are tackling such challenges now. It is believed that more and more POCT devices will appear in market for rapidly testing nucleic acids.

Besides test chips/strips/cartridges, readers are critical for POCT testing, many inexpensive handheld fluorescence readers are commercially available for directly reading fluorescence signals from the test chips/strips/cartridges. However, inexpensive handheld SERS readers are not commercially available to fit into the test chips/strips/cartridges, which has hindered commercialization of SERS-based POCT systems.

Smartphones have a great potential in recording signals from fluorescence and SERS POCT test chips/strips/cartridges.[381] One option is integration of an optical detector into an existing smartphone, enabling direct reading of signals with the smartphone. Another option is connection of a smartphone with an existing reader via Bluetooth, enabling wireless operation of the reader with the smartphone using an App, allowing for wireless transmission of data to a doctor’s office or a central station via a wireless 4G or 5G network. Such readers, which are wirelessly connected to smartphones, could be operated by someone at a remote central station.

Incorporation of numerous POCT devices, ambulances, clinics and hospitals into a wireless sensor network or a cloud-based network is an important direction in the future. Such a cloud-based network will play import roles in multi-facets of public health and security

in smart-cities, -towns, or -countries. For example, it will allow for real-time monitor reoccurrence or treatment process of chronic diseases. And it can be used to track acute infected or asymptotic COVID-19 patients. Furthermore, it can be employed to monitor the occurrence and progression of pandemic or epidemic diseases.

Besides *in vitro* POCT, NIR fluorescence and SERS imaging can achieve fast screening and real-time tracking and monitoring of specific targets in living cells and tissues. They can greatly overcome the drawbacks of current large diagnostic instruments, such as high cost, time consuming as well as requirement of professional training. It is worth noting that the longer wavelength probes exhibit weaker signals than the shorter-wavelength counterparts. However, the reduced light absorption and scattering by tissues and the depressed tissue autofluorescence not only enable deeper penetration but also allow for longer acquisition time with a greater signal-to-background ratio. On the other hand, in case of rapid screening demand such as image-guided surgical applications, use of shorter NIR wavelengths and tolerance of higher background noise may be necessary for achieving stronger signals.

One of technical barriers for bio-imaging is biocompatibility and biodegradability of NIR fluorescence and SERS probes. It is highly recommended to not only construct biocompatible and biodegradable probes, but also to reveal their mechanisms of action and metabolism, which can provide clear guidelines for choosing proper material and structure to design probes. In addition, improvement in spatial resolution of imaging is an important research direction. This will benefit to site-specific detection or mapping of physiological or pathological processes in live cells, tissues and organs. Moreover, Theranostics, which combines therapy with imaging functions into single entity to form therapeutic agents, has a great promise. It will allow for time-solved and space-resolved tracking and adjustment of medical intervention.

It is estimated that the global POCT market increases quickly from $29.5 billion in 2020 to $50.6 billion by 2025.[382] Market will drive the advance in the POCT techniques. With increasing need of sensitive and quantitative measurement of analytes in POC settings, the market share will shift from colorimetric and electrochemical devices to the NIR fluorescence and SERS devices. To the best of our knowledge, we do not have the quantitative data about the market value of NIR fluorescence and SERS bio-imaging. The technology development in NIR fluorescence and SERS bio-imaging will boost the growth of market in these areas in the future.

Acknowledgements

This work is partially supported by the National Institute of Neurological Disorders and Stroke of the National Institutes of Health (1U01NS119647). Wu is partially supported by the Armstrong-Siadat Professorship Endowment. The content is solely the responsibility of the authors and does not necessarily represent the official views of the National Institutes of Health.

Biography

Dr. Nianqiang (Nick) Wu received his Ph.D. degree in Materials Science & Engineering from Zhejiang University, China. Currently he is Armstrong-Siadat Endowed Chair Professor in Materials Science at University of Massachusetts Amherst. Dr. Wu is Fellow of the Electrochemical Society (FECS) and Royal Society of Chemistry (FRSC). He received several honors and awards such as Highly Cited Researcher (Clarivate Analytics, Thomson Reuters) and ECS Sensor Division Outstanding Achievement Award. He has authored or co-authored about 200 journal articles, 3 book chapters and 1 book entitled "*Biosensors Based on Nanomaterials and Nanodevices*".

Yingjie Hang is a graduate student under supervision of Prof. Wu in at University of Massachusettes Amherst. She received her BS degree from Soochow University in 2016. Her research interest lies in point-of-care testing, plasmon-enhanced fluorescence and surface-enhanced Raman scatterring (SERS) for protein and nucleic acids detection.

Jennifer Boryczka received her M.S. degree in Materials Science and Engineering from West Virginia University, USA. Currently she is a graduate student under supervision of Prof. Wu at University of Massachusetts Amherst. She has co-authored about 5 journal articles. Her research interest lies in plasmon-enhanced fluorescent sensing, imaging and photodynamic therapy.

References

1. Wang D, He S, Wang X, Yan Y, Liu J, Wu S, Liu S, Lei Y, Chen M, Li L, Zhang J, Zhang L, Hu X, Zheng X, Bai J, Zhang Y, Zhang Y, Song M and Tang Y, Nat. Biomed. Eng, 2020, 4, 1150–1158. [PubMed: 33273714]
2. Reboud J, Xu G, Garrett A, Adriko M, Yang Z, Tukahebwa EM, Rowell C and Cooper JM, Proc. Natl. Acad. Sci. U S A, 2019, 116, 4834–4842. [PubMed: 30782834]
3. Yuzon MK, Kim J-H and Kim S, Biochip J, 2019, 13, 277–287.

4. Chaiyo S, Mehmeti E, Siangproh W, Hoang TL, Nguyen HP, Chailapakul O and Kalcher K, Biosens. Bioelectron, 2018, 102, 113–120. [PubMed: 29128713]
5. Wu L and Qu X, Chem. Soc. Rev, 2015, 44, 2963–2997. [PubMed: 25739971]
6. Ning B, Yu T, Zhang S, Huang Z, Tian D, Lin Z, Niu A, Golden N, Hensley K, Threeton B, Lyon CJ, Yin X-M, Roy CJ, Saba NS, Rappaport J, Wei Q and Hu TY, Sci. Adv, 2021, 7, eabe3703. [PubMed: 33310733]
7. Meng J, Tang X, Zhou B, Xie Q and Yang L, Talanta, 2017, 164, 693–699. [PubMed: 28107992]
8. Song Y, Lin B, Tian T, Xu X, Wang W, Ruan Q, Guo J, Zhu Z and Yang C, Anal. Chem, 2019, 91, 388–404. [PubMed: 30412383]
9. Gao X, Xu H, Baloda M, Gurung AS, Xu L-P, Wang T, Zhang X and Liu G, Biosens. Bioelectron, 2014, 54, 578–584. [PubMed: 24333569]
10. Martinez AW, Phillips ST, Whitesides GM and Carrilho E, Anal. Chem, 2010, 82, 3–10. [PubMed: 20000334]
11. Li M, Gou H, Al-Ogaidi I and Wu N, ACS Sustain. Chem. Eng, 2013, 1, 713–723.
12. Song Y, Huang YY, Liu X, Zhang X, Ferrari M and Qin L, Trends Biotechnol, 2014, 32, 132–139. [PubMed: 24525172]
13. Berlanda SF, Breitfeld M, Dietsche CL and Dittrich PS, Anal. Chem, 2021, 93, 311–331. [PubMed: 33170661]
14. Quek CH and Leong KW, Nanomaterials, 2012, 2, 92–112. [PubMed: 28348298]
15. Yang F, Zhang Q, Huang S and Ma D, J. Mater. Chem. B, 2020, 8, 7856–7879 [PubMed: 32749426]
16. Hemmer E, Benayas A, Legare F and Vetrone F, Nanoscale Horiz, 2016, 1, 168–184. [PubMed: 32260620]
17. Smith AM, Mancini MC and Nie S, Nat. Nanotechnol, 2009, 4, 710–711. [PubMed: 19898521]
18. Sordillo L, Pu Y, Pratavieira S, Budansky Y and Alfano R, JBO, 2014, 19, 056004. [PubMed: 24805808]
19. Zhu S, Tian R, Antaris AL, Chen X and Dai H, Adv. Mater, 2019, 31, e1900321. [PubMed: 31025403]
20. Scholkmann F, Kleiser S, Metz AJ, Zimmermann R, Mata Pavia J, Wolf U and Wolf M, Neuroimage, 2014, 85 (Part 1), 6–27. [PubMed: 23684868]
21. Swanson C and D'Andrea A, Clin. Chem, 2013, 59, 641–648. [PubMed: 23364182]
22. Haga Y, David Kay H, Tempero MA and Zetterman RK, Clin. Biochem, 1992, 25, 277–283. [PubMed: 1381998]
23. Abugo OO, Nair R and Lakowicz JR, Anal. Biochem, 2000, 279, 142–150. [PubMed: 10706783]
24. Semenov AN, Yakimov BP, Rubekina AA, Gorin DA, Drachev VP, Zarubin MP, Velikanov AN, Lademann J, Fadeev VV, Priezzhev AV, Darvin ME and Shirshin EA, Molecules, 2020, 25, 1863.
25. Zeng H, MacAulay C, McLean DI and Palcic B, J. Photochem. Photobiol. B, 1997, 38, 234–240. [PubMed: 9203387]
26. Álvarez-Puebla RA, J. Phys. Chem. Lett, 2012, 3, 857–866. [PubMed: 26286411]
27. Miyawaki A, Nat. Methods, 2016, 13, 729–730. [PubMed: 27575623]
28. Lignos I, Morad V, Shynkarenko Y, Bernasconi C, Maceiczyk RM, Protesescu L, Bertolotti F, Kumar S, Ochsenbein ST, Masciocchi N, Guagliardi A, Shih CJ, Bodnarchuk MI, deMello AJ and Kovalenko MV, ACS Nano, 2018, 12, 5504–5517. [PubMed: 29754493]
29. Chang X-H, Zhang J, Wu L-H, Peng Y-K, Yang X-Y, Li X-L, Ma A-J, Ma J-C and Chen G-Q, Micromachines, 2019, 10, 422.
30. Antaris AL, Chen H, Diao S, Ma Z, Zhang Z, Zhu S, Wang J, Lozano AX, Fan Q, Chew L, Zhu M, Cheng K, Hong X, Dai H and Cheng Z, Nat Commun, 2017, 8, 15269. [PubMed: 28524850]
31. Jones MR, Osberg KD, Macfarlane RJ, Langille MR and Mirkin CA, Chem. Rev, 2011, 111, 3736–3827. [PubMed: 21648955]
32. Li M, Cushing SK and Wu N, Analyst, 2015, 140, 386–406. [PubMed: 25365823]
33. Dostálek J and Knoll W, Biointerphases, 2008, 3, Fd12–22. [PubMed: 20408695]
34. Lakowicz JR, Plasmonics, 2006, 1, 5–33. [PubMed: 19890454]

35. Ashcroft NW and Mermin DN, Solid Stat. Physics, Cengage Learning, 1976.
36. Shalaev VM and Kawata S, Nanophotonics with Surface Plasmon, Elsevier, 2007.
37. Mayer KM and Hafner JH, Chem. Rev, 2011, 111, 3828–3857. [PubMed: 21648956]
38. Mulvaney P, Langmuir, 1996, 12, 788–800.
39. Stiles PL, Dieringer JA, Shah NC and Van Duyne RP, Annu. Rev. Anal. Chem, 2008, 1, 601–626.
40. Moskovits M, Rev. Mod. Phys, 1985, 57, 783–826.
41. Schwartzberg AM and Zhang JZ, J. Phys. Chem. C, 2008, 112, 10323–10337.
42. Tang H, Zhu C, Meng G and Wu N, J. Electrochem. Soc, 2018, 165, B3098–B3118.
43. McMahon JM, Li S, Ausman LK and Schatz GC, J. Phys. Chem. C, 2011, 116, 1627–1637.
44. Li M, Cushing SK, Zhang J, Lankford J, Aguilar ZP, Ma D and Wu N, Nanotechnology, 2012, 23, 115501. [PubMed: 22383452]
45. Wang M, Rajeeva BB, Scarabelli L, Perillo EP, Dunn AK, Liz-Marzan LM and Zheng Y, J. Phys. Chem. C: Nanomater. Interfaces, 2016, 120, 14820–14827. [PubMed: 29576840]
46. Lakowicz JR, Anal. Biochem, 2005, 337, 171–194. [PubMed: 15691498]
47. Gryczynski I, Malicka J, Gryczynski Z and Lakowicz JR, Anal. Biochem, 2004, 324, 170–182. [PubMed: 14690680]
48. Käll M, Xu H and Johansson P, J. Raman Spectrosc, 2005, 36, 510–514.
49. Christesen SD, Appl. Spectrosc, 1988, 42, 318–321.
50. Fleischmann M, Hendra PJ and McQuillan AJ, Chem. Phys. Lett, 1974, 26, 163–166.
51. Jeanmaire DL and Van Duyne RP, J. Electroanal. Chem. Interfacial Electrochem, 1977, 84, 1–20.
52. Albrecht MG and Creighton JA, J. Am. Chem. Soc, 1977, 99, 5215–5217.
53. Doering WE and Nie S, J. Phys. Chem. B, 2002, 106, 311–317.
54. Kneipp K, Kneipp H, Itzkan I, Dasari RR and Feld MS, Chem. Rev, 1999, 99, 2957–2976. [PubMed: 11749507]
55. Kim J, Jang Y, Kim N-J, Kim H, Yi G-C, Shin Y, Kim MH and Yoon S, Front. Chem, 2019, 7.
56. Schatz GC, Young MA and Van Duyne RP, in Surface-Enhanced Raman Scattering: Physics and Applications, Springer Berlin Heidelberg, 2006, DOI: 10.1007/3-540-33567-6_2
57. Le Ru EC, Blackie E, Meyer M and Etchegoin PG, J. Phys. Chem. C, 2007, 111, 13794–13803.
58. Li M, Cushing SK, Zhou G and Wu N, Nanoscale, 2020, 12, 22036–22041. [PubMed: 33146197]
59. Schutz M, Muller CI, Salehi M, Lambert C and Schlucker S, J. Biophotonics, 2011, 4, 453–463. [PubMed: 21298811]
60. Graham D, Faulds K and Smith WE, Chem. Commun, 2006, 42, 4363–4371.
61. Keller T, Brem S, Tran V, Sritharan O, Schäfer D and Schlücker S, J. Biophotonics, 2020, 13, e201960126. [PubMed: 31957948]
62. Mu X, Guo Y, Li Y, Wang Z, Li Y and Xu S, J. Raman. Spectrosc, 2017, 48, 1196–1200.
63. Lin L, Tian X, Hong S, Dai P, You Q, Wang R, Feng L, Xie C, Tian Z-Q and Chen X, Angew. Chem. Int. Ed. Engl, 2013, 52, 7266–7271. [PubMed: 23703791]
64. Li M, Zhang J, Suri S, Sooter LJ, Ma D and Wu N, Anal. Chem, 2012, 84, 2837–2842. [PubMed: 22380526]
65. Gabudean AM, Biro D and Astilean S, J. Mol. Struct, 2011, 993, 420–424.
66. Michota A and Bukowska J, J. Raman. Spectrosc, 2003, 34, 21–25.
67. Gao X, Zheng P, Kasani S, Wu S, Yang F, Lewis S, Nayeem S, Engler-Chiurazzi EB, Wigginton JG, Simpkins JW and Wu N, Anal. Chem, 2017, 89, 10104–10110. [PubMed: 28817769]
68. Tan X, Wang Z, Yang J, Song C, Zhang R and Cui Y, Nanotechnology, 2009, 20, 445102. [PubMed: 19801773]
69. Zheng P, Li M, Jurevic R, Cushing SK, Liu Y and Wu N, Nanoscale, 2015, 7, 11005–11012. [PubMed: 26008641]
70. Zheng P, Kasani S, Shi X, Boryczka AE, Yang F, Tang H, Li M, Zheng W, Elswick DE and Wu N, Anal. Chim. Acta, 2018, 1040, 158–165. [PubMed: 30327106]
71. Park JE, Kim J and Nam JM, Chem. Sci, 2017, 8, 4696–4704. [PubMed: 28936337]
72. Lakowicz JR, Principles of Fluorescence Spectroscopy, Springer Academic, 2006.

73. Itoh T, Yamamoto YS and Ozaki Y, Chem. Soc. Rev, 2017, 46, 3904–3921. [PubMed: 28653715]
74. Khurgin JB and Sun G, J. Opt. Soc. Am. B, 2009, 26, B83–B95.
75. Li J, Cushing SK, Meng F, Senty TR, Bristow AD and Wu N, Nat. Photonics, 2015, 9, 601–607.
76. Li M, Zhou X, Ding W, Guo S and Wu N, Biosens. Bioelectron, 2013, 41, 889–893. [PubMed: 23098856]
77. Yang J, Zhang F, Chen Y, Qian S, Hu P, Li W, Deng Y, Fang Y, Han L, Luqman M and Zhao D, Chem. Commun, 2011, 47, 11618–11620.
78. Trotsiuk L, Muravitskaya A, Kulakovich O, Guzatov D, Ramanenka A, Kelestemur Y, Demir HV and Gaponenko S, Nanotechnology, 2020, 31, 105201. [PubMed: 31751975]
79. Tang F, He F, Cheng H and Li L, Langmuir, 2010, 26, 11774–11778. [PubMed: 20545370]
80. Gontero D, Veglia AV, Boudreau D and Bracamonte AG, J. Nanophotonics, 2017, 12, 012505.
81. Wang X, Zhang L, Hao A, Shi Z, Dai C, Yang Y and Huang H, ACS Appl. Nano. Mater, 2020, 3, 9796–9803.
82. Gao Y, Wang J, Wang W, Zhao T, Cui Y, Liu P, Xu S and Luo X, Anal. Chem, 2021, 93, 2480–2489. [PubMed: 33410672]
83. Theodorou IG, Jawad ZAR, Jiang Q, Aboagye EO, Porter AE, Ryan MP and Xie F, Chem. Mater, 2017, 29, 6916–6926.
84. Ren H, Yang J-L, Yang W-M, Zhong H-L, Lin J-S, Radjenovic PM, Sun L, Zhang H, Xu J, Tian Z-Q and Li J-F, ACS Mater. Lett, 2020, 3, 69–76.
85. Yang M, Moroz P, Jin Z, Budkina DS, Sundrani N, Porotnikov D, Cassidy J, Sugiyama Y, Tarnovsky AN, Mattoussi H and Zamkov M, J. Am. Chem. Soc, 2019, 141, 11286–11297. [PubMed: 31265269]
86. Itoh T, Yoshida K.-i., Tamaru H, Biju V and Ishikawa M, J. Photochem. Photobiol. A: Chem, 2011, 219, 167–179.
87. Li M, Cushing SK, Zhang J, Suri S, Evans R, Petros WP, Gibson LF, Ma D, Liu Y and Wu N, ACS Nano, 2013, 7, 4967–4976. [PubMed: 23659430]
88. Rissin DM, Kan CW, Campbell TG, Howes SC, Fournier DR, Song L, Piech T, Patel PP, Chang L, Rivnak AJ, Ferrell EP, Randall JD, Provuncher GK, Walt DR and Duffy DC, Nat. Biotechnol, 2010, 28, 595–599. [PubMed: 20495550]
89. Fu X, Chen L and Choo J, Anal. Chem, 2017, 89, 124–137. [PubMed: 28105817]
90. Yang Z, Liu H, Tian Y, Chen Y, Niu Z, Zhou C, Wang F, Gu C, Tang S, Jiang T and Zhou J, J. Mater. Chem. C, 2020, 8, 2142–2154.
91. Jiang T, Wang X, Zhou J and Jin H, Sens. Actuators B Chem, 2018, 258, 105–114.
92. Lee M, Kim H, Kim E, Yi SY, Hwang SG, Yang S, Lim EK, Kim B, Jung J and Kang T, ACS Appl. Mater. Interfaces, 2018, 10, 37829–37834. [PubMed: 30360053]
93. Farka Z, Mickert MJ, Hlavacek A, Skladal P and Gorris HH, Anal. Chem, 2017, 89, 11825–11830. [PubMed: 28949515]
94. Cheng Z, Choi N, Wang R, Lee S, Moon KC, Yoon SY, Chen L and Choo J, ACS Nano, 2017, 11, 4926–4933. [PubMed: 28441008]
95. Chen Z, Tabakman SM, Goodwin AP, Kattah MG, Daranciang D, Wang X, Zhang G, Li X, Liu Z, Utz PJ, Jiang K, Fan S and Dai H, Nat. Biotechnol, 2008, 26, 1285–1292. [PubMed: 18953353]
96. Al-Ogaidi I, Gou H, Aguilar ZP, Guo S, Melconian AK, Al-Kazaz AK, Meng F and Wu N, Chem. Commun, 2014, 50, 1344–1346.
97. Luo Y, Wang X, Du D and Lin Y, Biomater. Sci, 2015, 3, 1386–1394. [PubMed: 26301700]
98. Uchida M, Kosuge H, Terashima M, Willits DA, Liepold LO, Young MJ, McConnell MV and Douglas T, ACS Nano, 2011, 5, 2493–2502. [PubMed: 21391720]
99. Qian H, Huang Y, Duan X, Wei X, Fan Y, Gan D, Yue S, Cheng W and Chen T, Biosens. Bioelectron, 2019, 140, 111350. [PubMed: 31154255]
100. Kim S-E, Ahn K-Y, Park J-S, Kim KR, Lee KE, Han S-S and Lee J, Anal. Chem, 2011, 83, 5834–5843. [PubMed: 21639087]
101. Degorce F, Card A, Soh S, Trinquet E, Knapik GP and Xie B, Curr. Chem. Genomics, 2009, 3, 22–32. [PubMed: 20161833]

102. Norskov-Lauritsen L, Thomsen AR and Brauner-Osborne H, Int. J. Mol. Sci, 2014, 15, 2554–2572. [PubMed: 24531140]
103. Hepojoki S, Rusanen J, Hepojoki J, Nurmi V, Vaheri A, Lundkvist A, Hedman K and Vapalahti O, J. Clin. Microbiol, 2015, 53, 2292–2297. [PubMed: 25972427]
104. Shao K, Wang L, Wen Y, Wang T, Teng Y, Shen Z and Pan Z, Anal. Chim. Acta, 2019, 1068, 52–59. [PubMed: 31072477]
105. Xing H, Wei T, Lin X and Dai Z, Anal. Chim. Acta, 2018, 1042, 71–78. [PubMed: 30428990]
106. Zhao L, Cheng M, Liu G, Lu H, Gao Y, Yan X, Liu F, Sun P and Lu G, Sens. Actuators B Chem, 2018, 273, 185–190.
107. Yang J, Zhang Z and Yan G, Sens. Actuators B Chem, 2018, 255, 2339–2346.
108. Pyrak E, Krajczewski J, Kowalik A, Kudelski A and Jaworska A, Molecules, 2019, 24.
109. Strachan BC, Sloane HS, Lee JC, Leslie DC and Landers JP, Analyst, 2015, 140, 2008–2015. [PubMed: 25673152]
110. Peng L, Zhou J, Yin L, Man S and Ma L, Anal. Chim. Acta, 2020, 1125, 162–168. [PubMed: 32674762]
111. Liu X, Wang F, Aizen R, Yehezkeli O and Willner I, J. Am. Chem. Soc, 2013, 135, 11832–11839. [PubMed: 23841845]
112. Li M, Cushing SK, Liang H, Suri S, Ma D and Wu N, Anal. Chem, 2013, 85, 2072–2078. [PubMed: 23320458]
113. Wang S, Lifson MA, Inci F, Liang LG, Sheng YF and Demirci U, Expert Rev. Mol. Diagn, 2016, 16, 449–459. [PubMed: 26777725]
114. Huang L, Ding L, Zhou J, Chen S, Chen F, Zhao C, Xu J, Hu W, Ji J, Xu H and Liu GL, Biosens. Bioelectron, 2021, 171, 112685. [PubMed: 33113383]
115. Sun Y and Li T, Anal. Chem, 2018, 90, 11614–11621. [PubMed: 30175580]
116. Liang Z, Zhou J, Petti L, Shao L, Jiang T, Qing Y, Xie S, Wu G and Mormile P, Analyst, 2019, 144, 1741–1750. [PubMed: 30663745]
117. Wong YP, Othman S, Lau YL, Radu S and Chee HY, J. Appl. Microbiol, 2018, 124, 626–643. [PubMed: 29165905]
118. Garibyan L and Avashia N, J. Investig. Dermatol. Symp. Proc, 2013, 133, 1–4.
119. Li J, Macdonald J and von Stetten F, Analyst, 2018, 144, 31–67. [PubMed: 30426974]
120. Shi C, Liu Q, Ma C and Zhong W, Anal. Chem, 2014, 86, 336–339. [PubMed: 24345199]
121. Zhou Y, Li B, Wang M, Wang J, Yin H and Ai S, Mikrochim. Acta, 2017, 184, 4359–4365.
122. Fakruddin M, Mannan KS, Chowdhury A, Mazumdar RM, Hossain MN, Islam S and Chowdhury MA, J. Pharm. Bioallied. Sci, 2013, 5, 245–252. [PubMed: 24302831]
123. Nzelu CO, Kato H and Peters NC, PLoS Negl. Trop. Dis, 2019, 13, e0007698. [PubMed: 31697673]
124. Piepenburg O, Williams CH, Stemple DL and Armes NA, PLoS Biol, 2006, 4, e204. [PubMed: 16756388]
125. James AS and Alawneh JI, Diagnostics, 2020, 10, 399
126. Bidar N, Oroojalian F, Baradaran B, Eyvazi S, Amini M, Jebelli A, Hosseini SS, Pashazadeh-Panahi P, Mokhtarzadeh A and de la Guardia M, TrAC-Trend Anal. Chem, 2020, 131, 116021.
127. Chen JS, Ma E, Harrington LB, Da Costa M, Tian X, Palefsky JM and Doudna JA, Science, 2018, 360, 436–439. [PubMed: 29449511]
128. Khalil I, Yehye WA, Julkapli NM, Rahmati S, Sina AA, Basirun WJ and Johan MR, Biosens. Bioelectron, 2019, 131, 214–223. [PubMed: 30844598]
129. Guven B, Boyaci IH, Tamer U, Acar-Soykut E and Dogan U, Talanta, 2015, 136, 68–74. [PubMed: 25702987]
130. Ge L, Sun X, Hong Q and Li F, ACS Appl. Mater. Interfaces, 2017, 9, 32089–32096. [PubMed: 28849916]
131. Zhang J, Yang Y, Jiang X, Dong C, Song C, Han C and Wang L, Biosens. Bioelectron, 2019, 141, 111402. [PubMed: 31185418]

132. Ryoo S-R, Lee J, Yeo J, Na H-K, Kim Y-K, Jang H, Lee JH, Han SW, Lee Y, Kim VN and Min D-H, ACS Nano, 2013, 7, 5882–5891. [PubMed: 23767402]
133. Song C, Liu Y, Jiang X, Zhang J, Dong C, Li J and Wang L, Talanta, 2019, 205, 120137. [PubMed: 31450475]
134. Huang J, Su X and Li Z, Anal. Chem, 2012, 84, 5939–5943. [PubMed: 22715964]
135. Guk K, Hwang SG, Lim J, Son HY, Choi Y, Huh YM, Kang T, Jung J and Lim EK, Chem. Commun, 2019, 55, 3457–3460.
136. Adegoke O, Kato T and Park EY, Biosens. Bioelectron, 2016, 80, 483–490. [PubMed: 26890823]
137. Harper MM, Robertson B, Ricketts A and Faulds K, Chem. Commun, 2012, 48, 9412–9414.
138. Choi JH, Lim J, Shin M, Paek SH and Choi JW, Nano Lett, 2020, DOI: 10.1021/acs.nanolett.0c04303.
139. Liu Y, Kannegulla A, Wu B and Cheng L-J, ACS Appl. Mater. Interfaces, 2018, 10, 18524–18531. [PubMed: 29763288]
140. Dougan JA, MacRae D, Graham D and Faulds K, Chem. Commun, 2011, 47, 4649.
141. Draz MS and Lu X, Theranostics, 2016, 6, 522–532. [PubMed: 26941845]
142. Obande GA and Banga Singh KK, Infect. Drug Resist, 2020, 13, 455–483. [PubMed: 32104017]
143. Zhao X, Li S, Liu G, Wang Z, Yang Z, Zhang Q, Liang M, Liu J, Li Z, Tong Y, Zhu G, Wang X, Jiang L, Wang W, Tan G-Y and Zhang L, Sci. Bull, 2020, 66, 69–77.
144. Liu Y, Li S, Zhang L, Zhao Q, Li N and Wu Y, RSC Adv, 2020, 10, 28037–28040. [PubMed: 35519131]
145. Yu M, Yao Y, Cui B, Sun C, Zhao X, Wang Y, Liu G, Cui H and Zeng Z, ACS Appl. Nano Mater, 2018, 2, 48–57.
146. Tan W, Zhang L, Doery JCG and Shen W, Lab Chip, 2020, 20, 394–404. [PubMed: 31853529]
147. Zhou Y and Yoon J, Chem. Soc. Rev, 2012, 41, 52–67. [PubMed: 21799954]
148. Feng R, Xu Y, Zhao H, Duan X and Sun S, Analyst, 2016, 141, 3219–3223. [PubMed: 27143565]
149. Al-Ogaidi I, Gou H, Al-Kazaz AK, Aguilar ZP, Melconian AK, Zheng P and Wu N, Anal. Chim. Acta, 2014, 811, 76–80. [PubMed: 24456597]
150. Tan W, Zhang L, Doery JCG and Shen W, Sens. Actuators B Chem, 2020, 305, 127448.
151. Yin J, Kwon Y, Kim D, Lee D, Kim G, Hu Y, Ryu JH and Yoon J, J. Am. Chem. Soc, 2014, 136, 5351–5358. [PubMed: 24649915]
152. Wood RM, Rilling JK, Sanfey AG, Bhagwagar Z and Rogers RD, Neuropsychopharmacology, 2006, 31, 1075–1084. [PubMed: 16407905]
153. Rondanelli M, Opizzi A, Antoniello N, Boschi F, Iadarola P, Pasini E, Aquilani R and Dioguardi FS, Clin. Nutr, 2011, 30, 571–577. [PubMed: 21636183]
154. Xiao F, Yu J, Guo Y, Deng J, Li K, Du Y, Chen S, Zhu J, Sheng H and Guo F, Metabolism, 2014, 63, 841–850. [PubMed: 24684822]
155. Martin C and Zhang Y, Nat. Rev. Mol. Cell Biol, 2005, 6, 838–849. [PubMed: 16261189]
156. Wood JM, Decker H, Hartmann H, Chavan B, Rokos H, Spencer JD, Hasse S, Thornton MJ, Shalbaf M, Paus R and Schallreuter KU, FASEB J, 2009, 23, 2065–2075. [PubMed: 19237503]
157. Weaver ICG, Champagne FA, Brown SE, Dymov S, Sharma S, Meaney MJ and Szyf M, J. Neurosci, 2005, 25, 11045–11054. [PubMed: 16306417]
158. Mkrtchyan G, Aleshin V, Parkhomenko Y, Kaehne T, Luigi Di Salvo M, Parroni A, Contestabile R, Vovk A, Bettendorff L and Bunik V, Sci. Rep, 2015, 5, 12583. [PubMed: 26212886]
159. Naderi N and House JD, in Adv. Food Nutr. Res, Academic Press, 2018, vol. 83, pp. 195–213. [PubMed: 29477222]
160. Visentin M, Diop-Bove N, Zhao R and Goldman ID, Annu. Rev. Physiol, 2014, 76, 251–274. [PubMed: 24512081]
161. I. o. Medicine, Dietary Reference Intakes for Vitamin C, Vitamin E, Selenium, and Carotenoids, The National Academies Press, 2000.
162. Brigelius-Flohé R and Traber MG, FASEB J, 1999, 13, 1145–1155. [PubMed: 10385606]
163. U. Nations, in World Drug Report 2017, United Nations, 2017, DOI: doi:10.18356/bdc264f4-en.

164. De Rycke E, Stove C, Dubruel P, De Saeger S and Beloglazova N, Biosens. Bioelectron, 2020, 169, 112579. [PubMed: 32947080]
165. Li D, Ma Y, Duan H, Deng W and Li D, Biosens. Bioelectron, 2018, 99, 389–398. [PubMed: 28806669]
166. Zhou Q, Meng G, Liu J, Huang Z, Han F, Zhu C, Kim D-J, Kim T and Wu N, Adv. Mater. Technol, 2017, 2, 1700028.
167. Hu X, Zheng P, Meng G, Huang Q, Zhu C, Han F, Huang Z, Li Z, Wang Z and Wu N, Nanotechnology, 2016, 27, 384001. [PubMed: 27528554]
168. Xue W, Tan X, Khaing Oo MK, Kulkarni G, Ilgen MA and Fan X, Analyst, 2020, 145, 1346–1354. [PubMed: 31967116]
169. Yu W, Jiang C, Xie B, Wang S, Yu X, Wen K, Lin J, Wang J, Wang Z and Shen J, Anal. Chim. Acta, 2020, 1102, 91–98. [PubMed: 32044000]
170. Hua X, Ding Y, Yang J, Ma M, Shi H and Wang M, Sci. Total. Environ, 2017, 583, 222–227. [PubMed: 28117157]
171. Li M, Ma M, Hua X, Shi H, Wang Q and Wang M, RSC Adv, 2015, 5, 3039–3044.
172. Guler E, Bozokalfa G, Demir B, Gumus ZP, Guler B, Aldemir E, Timur S and Coskunol H, Drug Test Anal., 2017, 9, 578–587. [PubMed: 27336666]
173. Ahmed SR, Chand R, Kumar S, Mittal N, Srinivasan S and Rajabzadeh AR, TrAC-Trend Anal. Chem, 2020, 131, 116006.
174. Wu L, Li G, Xu X, Zhu L, Huang R and Chen X, TrAC-Trend Anal. Chem, 2019, 113, 140–156.
175. Nebu J, Anjali Devi JS, Aparna RS, Aswathy B, Aswathy AO and Sony G, Mikrochim. Acta, 2018, 185, 532. [PubMed: 30402728]
176. Huang Z, Meng G, Huang Q, Yang Y, Zhu C and Tang C, Adv. Mater, 2010, 22, 4136–4139. [PubMed: 20803760]
177. Qian C, Guo Q, Xu M, Yuan Y and Yao J, RSC Adv, 2015, 5, 53306–53312.
178. Zhu C, Meng G, Zheng P, Huang Q, Li Z, Hu X, Wang X, Huang Z, Li F and Wu N, Adv. Mater, 2016, 28, 4871–4876. [PubMed: 27112639]
179. Guo Z, Park S, Yoon J and Shin I, Chem. Soc. Rev, 2014, 43, 16–29. [PubMed: 24052190]
180. Alvarez-Puebla RA and Liz-Marzan LM, Angew. Chem. Int. Ed. Engl, 2012, 51, 11214–11223. [PubMed: 23074161]
181. Song G, Jiang D, Wang L, Ning J, Sun X, Su F, Chen M and Tian Y, Chem. Commun, 2020, 56, 5405–5408.
182. Li C, Yao D, Jiang X, Liang A and Jiang Z, J. Mater. Chem. C, 2020, 8, 11088–11101
183. Li M, Wang Q, Shi X, Hornak LA and Wu N, Anal. Chem, 2011, 83, 7061–7065. [PubMed: 21842845]
184. Chen P, Jiang X, Huang K, Hu P, Li X, Wei L, Liu W, Wei L, Tao C, Ying B, Wei X and Geng J, ACS Appl. Mater. Interfaces, 2019, 11, 36476–36484. [PubMed: 31532182]
185. Li D, Ma Y, Duan H, Jiang F, Deng W and Ren X, Anal. Chim. Acta, 2018, 1038, 148–156. [PubMed: 30278897]
186. Chen X, Zhou Y, Peng X and Yoon J, Chem. Soc. Rev, 2010, 39, 2120–2135. [PubMed: 20502801]
187. Cao J, Zhao C, Wang X, Zhang Y and Zhu W, Chem. Commun, 2012, 48, 9897–9899.
188. Zheng P, Shi X, Curtin K, Yang F and Wu N, Mater. Res. Express, 2017, 4, 055017.
189. Li M, Zhou X, Guo S and Wu N, Biosens. Bioelectron, 2013, 43, 69–74. [PubMed: 23277342]
190. Yang Z, Loh KY, Chu Y-T, Feng R, Satyavolu NSR, Xiong M, Nakamata Huynh SM, Hwang K, Li L, Xing H, Zhang X, Chemla YR, Gruebele M and Lu Y, J. Am. Chem. Soc, 2018, 140, 17656–17665. [PubMed: 30427666]
191. Lake RJ, Yang Z, Zhang J and Lu Y, Acc. Chem. Res, 2019, 52, 3275–3286. [PubMed: 31721559]
192. Lin Y, Yang Z, Lake RJ, Zheng C and Lu Y, Angew. Chem. Int. Ed. Engl, 2019, 58, 17061–17067. [PubMed: 31529664]
193. Wang Y and Irudayaraj J, Chem. Commun, 2011, 47, 4394–4396.

194. Drain PK, Hyle EP, Noubary F, Freedberg KA, Wilson D, Bishai WR, Rodriguez W and Bassett IV, Lancet Infect. Dis, 2014, 14, 239–249. [PubMed: 24332389]
195. Kettler H, White K, and Hawkes S, Mapping the landscape of diagnostics for sexually transmitted infections. Geneva: World Health Organization, 2004.
196. Yang F, Zhang Y, Cui X, Fan Y, Xue Y, Miao H and Li G, Biotechnol. J, 2019, 14, 1800181.
197. Gorkin R, Park J, Siegrist J, Amasia M, Lee BS, Park JM, Kim J, Kim H, Madou M and Cho YK, Lab chip, 2010, 10, 1758–1773. [PubMed: 20512178]
198. Nge PN, Rogers CI and Woolley AT, Chem. Rev, 2013, 113, 2550–2583. [PubMed: 23410114]
199. Park J, Han DH and Park J-K, LChip, 2020, 20, 1191–1203.
200. Thurgood P, Zhu JY, Nguyen N, Nahavandi S, Jex AR, Pirogova E, Baratchi S and Khoshmanesh K, Lab chip, 2018, 18, 2730–2740. [PubMed: 30063234]
201. Seo J, Wang C, Chang S, Park J and Kim W, LChip, 2019, 19, 1790–1796.
202. Kim B, Oh S, You D and Choi S, Anal. Chem, 2017, 89, 1439–1444. [PubMed: 28208273]
203. Gervais L, de Rooij N and Delamarche E, Adv. Mater, 2011, 23, H151–176. [PubMed: 21567479]
204. Han J, Qi A, Zhou J, Wang G, Li B and Chen L, ACS Sens, 2018, 3, 1789–1794. [PubMed: 30080022]
205. Guler MT, Beyazkilic P and Elbuken C, Sens. Actuators A Phys, 2017, 265, 224–230.
206. Ma Y-D, Chen Y-S and Lee G-B, Sens. Actuators B Chem, 2019, 296, 126647.
207. Park J and Park J-K, LChip, 2019, 19, 2973–2977.
208. Díaz-González M, Boix G, Fernández-Sánchez C and Baldi A, SPIE, 2017.
209. Jo B, Lerberghe LMV, Motsegood KM and Beebe DJ, J. Microelectromech. Syst, 2000, 9, 76–81.
210. Olanrewaju AO, Robillard A, Dagher M and Juncker D, LChip, 2016, 16, 3804–3814.
211. Aeinehvand MM, Weber L, Jiménez M, Palermo A, Bauer M, Loeffler FF, Ibrahim F, Breitling F, Korvink J, Madou M, Mager D and Martínez-Chapa SO, LChip, 2019, 19, 1090–1100.
212. Enders A, Siller IG, Urmann K, Hoffmann MR and Bahnemann J, Small, 2019, 15, e1804326. [PubMed: 30548194]
213. Luo W, Yarn K, Shih M, Wu Y, Chang K and Weng M 3rd IEEE International Conference on NEMS, 2008, 801–806
214. Xiong Q, Lim CY, Ren J, Zhou J, Pu K, Chan-Park MB, Mao H, Lam YC and Duan H, Nat. Commun, 2018, 9, 1743. [PubMed: 29717124]
215. Rasouli MR and Tabrizian M, LChip, 2019, 19, 3316–3325.
216. Bender AT, Borysiak MD, Levenson AM, Lillis L, Boyle DS and Posner JD, Anal. Chem, 2018, 90, 7221–7229. [PubMed: 29761701]
217. Xiang N, Li Q and Ni Z, Anal. Chem, 2020, 92, 6770–6776. [PubMed: 32297510]
218. Gao R, Cheng Z, deMello AJ and Choo J, Lab chip, 2016, 16, 1022–1029. [PubMed: 26879372]
219. Szydzik C, Khoshmanesh K, Mitchell A and Karnutsch C, Biomicrofluidics, 2015, 9, 064120. [PubMed: 26759637]
220. Ali MA, Mondal K, Jiao Y, Oren S, Xu Z, Sharma A and Dong L, ACS Appl. Mater. Interfaces, 2016, 8, 20570–20582. [PubMed: 27442623]
221. Gao R, Lv Z, Mao Y, Yu L, Bi X, Xu S, Cui J and Wu Y, ACS Sens, 2019, 4, 938–943. [PubMed: 30864786]
222. Sharafeldin M and Davis JJ, Anal. Chem, 2021, 93, 184–197. [PubMed: 33215911]
223. Tripathi S, Varun Kumar YVB, Prabhakar A, Joshi SS and Agrawal A, J. Micromech. Microeng, 2015, 25, 084004.
224. Maria MS, Chandra TS and Sen AK, Microfluid. Nanofluidics, 2017, 21.
225. Tripathi S, Varun Kumar YVB, Prabhakar A, Joshi SS and Agrawal A, J. Micromech. Microeng, 2015, 25, 083001.
226. Haeberle S, Brenner T, Zengerle R and Ducrée J, LChip, 2006, 6, 776–781.
227. Liu SC, Yoo PB, Garg N, Lee AP and Rasheed S, Sens. Actuators A Phys, 2021, 317, 112482.
228. Mohammadi M, Madadi H, Casals-Terre J and Sellares J, Anal. Bioanal. Chem, 2015, 407, 4733–4744. [PubMed: 25925854]

229. Ji HM, Samper V, Chen Y, Heng CK, Lim TM and Yobas L, Biomed. Microdevices, 2008, 10, 251–257. [PubMed: 17914675]
230. Yang X, Forouzan O, Brown TP and Shevkoplyas SS, Lab chip, 2012, 12, 274–280. [PubMed: 22094609]
231. Shimizu H, Kumagai M, Mori E, Mawatari K and Kitamori T, Anal. Methods, 2016, 8, 7597–7602.
232. Svanes K and Zweifach BW, Microvasc. Res, 1968, 1, 210–220.
233. Fung Y-C, Microvasc. Res, 1973, 5, 34–48. [PubMed: 4684755]
234. Yang S, Undar A and Zahn JD, Lab chip, 2006, 6, 871–880. [PubMed: 16804591]
235. Fan R, Vermesh O, Srivastava A, Yen BK, Qin L, Ahmad H, Kwong GA, Liu CC, Gould J, Hood L and Heath JR, Nat. Biotechnol, 2008, 26, 1373–1378. [PubMed: 19029914]
236. Wang J, Ahmad H, Ma C, Shi Q, Vermesh O, Vermesh U and Heath J, Lab chip, 2010, 10, 3157–3162. [PubMed: 20924527]
237. Maria MS, Rakesh PE, Chandra TS and Sen AK, Sci. Rep, 2017, 7, 43457. [PubMed: 28256564]
238. Liu C, Mauk M, Gross R, Bushman FD, Edelstein PH, Collman RG and Bau HH, Anal. Chem, 2013, 85, 10463–10470. [PubMed: 24099566]
239. Luka G, Ahmadi A, Najjaran H, Alocilja E, DeRosa M, Wolthers K, Malki A, Aziz H, Althani A and Hoorfar M, Sensors, 2015, 15, 30011–30031. [PubMed: 26633409]
240. Choi K, Ng AH, Fobel R and Wheeler AR, Annu. Rev. Anal. Chem, 2012, 5, 413–440.
241. Coelho B, Veigas B, Águas H, Fortunato E, Martins R, Baptista P and Igreja R, Sensors, 2017, 17, 2616.
242. Mugele F and Baret J-C, J. Phys. Condens. Matter, 2005, 17, R705–R774.
243. Foudeh AM, Brassard D, Tabrizian M and Veres T, Lab chip, 2015, 15, 1609–1618. [PubMed: 25659351]
244. Lee MS, Hsu W, Huang HY, Tseng HY, Lee CT, Hsu CY, Shieh YC, Wang SH, Yao DJ and Liu CH, Biosens. Bioelectron, 2020, 150, 111851. [PubMed: 31740257]
245. Srinivasan V, Pamula VK and Fair RB, Lab chip, 2004, 4, 310–315. [PubMed: 15269796]
246. Stumpf F, Schwemmer F, Hutzenlaub T, Baumann D, Strohmeier O, Dingemanns G, Simons G, Sager C, Plobner L, von Stetten F, Zengerle R and Mark D, Lab chip, 2016, 16, 199–207. [PubMed: 26610171]
247. Yazdi SH, Giles KL and White IM, Anal. Chem, 2013, 85, 10605–10611. [PubMed: 24125433]
248. Qi J, Zeng J, Zhao F, Lin SH, Raja B, Strych U, Willson RC and Shih WC, Nanoscale, 2014, 6, 8521–8526. [PubMed: 24953169]
249. Kaminska A, Witkowska E, Winkler K, Dziecielewski I, Weyher JL and Waluk J, Biosens. Bioelectron, 2015, 66, 461–467. [PubMed: 25497986]
250. Sang CH, Chou SJ, Pan FM and Sheu JT, Biosens. Bioelectron, 2016, 75, 285–292. [PubMed: 26322591]
251. Chang CM, Chang WH, Wang CH, Wang JH, Mai JD and Lee GB, Lab chip, 2013, 13, 1225–1242. [PubMed: 23407669]
252. Sykes PJ, Neoh SH, Brisco MJ, Hughes E, Condon J and Morley AA, BioTechniques, 1992, 13, 444–449. [PubMed: 1389177]
253. Shen F, Du W, Kreutz JE, Fok A and Ismagilov RF, Lab chip, 2010, 10, 2666–2672. [PubMed: 20596567]
254. Safavieh M, Kanakasabapathy MK, Tarlan F, Ahmed MU, Zourob M, Asghar W and Shafiee H, ACS Biomater. Sci. Eng, 2016, 2, 278–294. [PubMed: 28503658]
255. Yuan H, Chao Y and Shum HC, Small, 2020, 16, 1904469.
256. Chen Y, Mei Y, Zhao X and Jiang X, Anal. Chem, 2020, 92, 14846–14852. [PubMed: 33064442]
257. Kim J, Johnson M, Hill P and Gale BK, Integr. Biol, 2009, 1, 574–586.
258. Pang Z, Al-Mahrouki A, Berezovski M and Krylov SN, Electrophoresis, 2006, 27, 1489–1494. [PubMed: 16532518]
259. Sethu P, Anahtar M, Moldawer LL, Tompkins RG and Toner M, Anal. Chem, 2004, 76, 6247–6253. [PubMed: 15516115]

260. Nan L, Jiang Z and Wei X, Lab chip, 2014, 14, 1060–1073. [PubMed: 24480982]
261. Kim J, Hong JW, Kim DP, Shin JH and Park I, Lab chip, 2012, 12, 2914–2921. [PubMed: 22722645]
262. Shin Y, Perera AP, Wong CC and Park MK, Lab chip, 2014, 14, 359–368. [PubMed: 24263404]
263. Cho YK, Lee JG, Park JM, Lee BS, Lee Y and Ko C, Lab chip, 2007, 7, 565–573. [PubMed: 17476374]
264. Hu W-P, Chen Y-C and Chen W-Y, Sci. Rep, 2020, 10, 21132. [PubMed: 33273557]
265. Yin J, Suo Y, Zou Z, Sun J, Zhang S, Wang B, Xu Y, Darland D, Zhao JX and Mu Y, LChip, 2019, 19, 2769–2785.
266. Petralia S, Sciuto EL and Conoci S, Analyst, 2017, 142, 140–146.
267. Chen D, Mauk M, Qiu X, Liu C, Kim J, Ramprasad S, Ongagna S, Abrams WR, Malamud D, Corstjens PL and Bau HH, Biomed. Microdevices, 2010, 12, 705–719. [PubMed: 20401537]
268. Zhu C, Hu A, Cui J, Yang K, Zhu X, Liu Y, Deng G and Zhu L, Micromachines, 2019, 10, 537.
269. Solsona M, Westerbeek EY, Bomer JG, Olthuis W and van den Berg A, LChip, 2019, 19, 1054–1059.
270. Liu C, Sun J, Li J, Xiang C, Che L, Wang Z and Zhou X, Sci. Rep, 2017, 7, 7552. [PubMed: 28790426]
271. Ramachandran A, Huyke DA, Sharma E, Sahoo MK, Huang C, Banaei N, Pinsky BA and Santiago JG, Proc. Natl. Acad. Sci. U S A, 2020, 117, 29518–29525. [PubMed: 33148808]
272. Betancur V, Sun J, Wu N and Liu Y, Micromachines, 2017, 8, 376.
273. Zimmermann M, Schmid H, Hunziker P and Delamarche E, Lab chip, 2007, 7, 119–125. [PubMed: 17180214]
274. Yeh E-C, Fu C-C, Hu L, Thakur R, Feng J and Lee LP, Sci. Adv, 2017, 3, e1501645. [PubMed: 28345028]
275. Mak WC, Beni V and Turner APF, TrAC-Trend Anal. Chem, 2016, 79, 297–305.
276. Gervais L and Delamarche E, LChip, 2009, 9, 3330.
277. Ghosh S and Ahn CH, Analyst, 2019, 144, 2109–2119. [PubMed: 30741267]
278. Xu L, Lee H, Jetta D and Oh KW, LChip, 2015, 15, 3962–3979.
279. Qin L, Vermesh O, Shi Q and Heath JR, Lab chip, 2009, 9, 2016–2020. [PubMed: 19568669]
280. Zhu L, Kroodsma N, Yeom J, Haan JL, Shannon MA and Meng DD, Microfluid. Nanofluidics, 2011, 11, 569–578.
281. Gervais L, Hitzbleck M and Delamarche E, Biosens. Bioelectron, 2011, 27, 64–70. [PubMed: 21752632]
282. Xu L, Wang A, Li X and Oh KW, Biomicrofluidics, 2020, 14, 031503. [PubMed: 32509049]
283. Morrissette JM, Mahapatra PS, Ghosh A, Ganguly R and Megaridis CM, Sci. Rep, 2017, 7, 1800. [PubMed: 28496152]
284. Shin S, Kim B, Kim YJ and Choi S, Biosens. Bioelectron, 2019, 133, 169–176. [PubMed: 30928735]
285. Lee KK, Kim MO and Choi S, J. Pharm. Biomed. Anal, 2019, 162, 28–33. [PubMed: 30219596]
286. Parolo C, Sena-Torralba A, Bergua JF, Calucho E, Fuentes-Chust C, Hu L, Rivas L, Alvarez-Diduk R, Nguyen EP, Cinti S, Quesada-Gonzalez D and Merkoci A, Nat. Protoc, 2020, 15, 3788–3816. [PubMed: 33097926]
287. Hu J, Wang S, Wang L, Li F, Pingguan-Murphy B, Lu TJ and Xu F, Biosens. Bioelectron, 2014, 54, 585–597. [PubMed: 24333570]
288. Wei H, Peng Y, Bai Z, Rong Z and Wang S, Analyst, 2021, 146, 558–564. [PubMed: 33165449]
289. Kasetsirikul S, Shiddiky MJA and Nguyen N-T, Microfluid. Nanofluidics, 2020, 24, 17
290. Wang R, Zhang W, Wang P and Su X, Mikrochim. Acta, 2018, 185, 191. [PubMed: 29503465]
291. Gao X, Boryczka J, Zheng P, Kasani S, Yang F, Engler-Chiurazzi EB, Simpkins JW, Wigginton JG and Wu N, Biosens. Bioelectron, 2021, 177, 112967. [PubMed: 33429202]
292. Gao X, Boryczka J, Kasani S and Wu N, Anal. Chem, 2021, 93, 3, 1326–1332 [PubMed: 33347264]

293. Yang X, Liu X, Gu B, Liu H, Xiao R, Wang C and Wang S, Mikrochim. Acta, 2020, 187.
294. Weng X and Neethirajan S, Mikrochim. Acta, 2017, 184, 4545–4552.
295. Anfossi L, Di Nardo F, Cavalera S, Giovannoli C, Spano G, Speranskaya ES, Goryacheva IY and Baggiani C, Mikrochim. Acta, 2018, 185, 94. [PubMed: 29594559]
296. Deng X, Wang C, Gao Y, Li J, Wen W, Zhang X and Wang S, Biosens. Bioelectron, 2018, 105, 211–217. [PubMed: 29412945]
297. Wang J, Cao F, He S, Xia Y, Liu X, Jiang W, Yu Y, Zhang H and Chen W, Talanta, 2018, 176, 444–449. [PubMed: 28917774]
298. Lu Z, Rey E, Vemulapati S, Srinivasan B, Mehta S and Erickson D, Lab chip, 2018, 18, 3865–3871. [PubMed: 30444230]
299. Yetisen AK, Akram MS and Lowe CR, LChip, 2013, 13, 2210.
300. Guo W, Hansson J and van der Wijngaart W, Anal. Chem, 2020, 92, 6194–6199. [PubMed: 32323979]
301. Li H and Steckl AJ, Anal. Chem, 2019, 91, 352–371. [PubMed: 30257554]
302. Cate DM, Adkins JA, Mettakoonpitak J and Henry CS, Anal Chem, 2015, 87, 19–41. [PubMed: 25375292]
303. Fu E, Ramsey SA, Kauffman P, Lutz B and Yager P, Microfluid. Nanofluidics, 2011, 10, 29–35. [PubMed: 22140373]
304. Ainla A, Hamedi MM, Güder F and Whitesides GM, Adv. Mater, 2017, 29, 1702894.
305. Choi JR, Liu Z, Hu J, Tang R, Gong Y, Feng S, Ren H, Wen T, Yang H, Qu Z, Pingguan-Murphy B and Xu F, Anal. Chem, 2016, 88, 6254–6264. [PubMed: 27012657]
306. Koo CK, He F and Nugen SR, Analyst, 2013, 138, 4998–5004. [PubMed: 23828822]
307. Choi JR, Hu J, Tang R, Gong Y, Feng S, Ren H, Wen T, Li X, Wan Abas WA, Pingguan-Murphy B and Xu F, Lab chip, 2016, 16, 611–621. [PubMed: 26759062]
308. Connelly JT, Rolland JP and Whitesides GM, Anal. Chem, 2015, 87, 7595–7601. [PubMed: 26104869]
309. Chen P, Chen C, Liu Y, Du W, Feng X and Liu B-F, Sens. Actuators B Chem, 2019, 283, 472–477.
310. Scida K, Li B, Ellington AD and Crooks RM, Anal. Chem, 2013, 85, 9713–9720. [PubMed: 24070108]
311. Yang Z, Xu G, Reboud J, Ali SA, Kaur G, McGiven J, Boby N, Gupta PK, Chaudhuri P and Cooper JM, ACS Sens, 2018, 3, 403–409. [PubMed: 29322764]
312. Ahn H, Batule BS, Seok Y and Kim MG, Anal. Chem, 2018, 90, 10211–10216. [PubMed: 30075080]
313. Komatsu T, Maeki M, Ishida A, Tani H and Tokeshi M, ACS Sens, 2020, 5, 1287–1294. [PubMed: 32283919]
314. Rohrman BA and Richards-Kortum RR, Lab chip, 2012, 12, 3082–3088. [PubMed: 22733333]
315. Phillips EA, Moehling TJ, Ejendal KFK, Hoilett OS, Byers KM, Basing LA, Jankowski LA, Bennett JB, Lin LK, Stanciu LA and Linnes JC, Lab chip, 2019, 19, 3375–3386. [PubMed: 31539001]
316. Ebnesajjad S, in Surface Treatment of Materials for Adhesive Bonding (Second Edition), William Andrew Publishing, Oxford, 2014, DOI: 10.1016/B978-0-323-26435-8.00004-6, pp. 39–75.
317. Di Gianfrancesco A, in Materials for Ultra-Supercritical and Advanced Ultra-Supercritical Power Plants, Woodhead Publishing, 2017, DOI: 10.1016/B978-0-08-100552-1.00008-7, pp. 197–245.
318. Holik AS, in Encyclopedia of Materials: Science and Technology, Elsevier, Oxford, 2001, DOI: 10.1016/B0-08-043152-6/01142-6, pp. 6458–6463.
319. Lichtman JW and Conchello J-A, Nat. Methods, 2005, 2, 910–919. [PubMed: 16299476]
320. Huang B, Bates M and Zhuang X, Annu. Rev. Biochem, 2009, 78, 993–1016. [PubMed: 19489737]
321. de Grooth BG, van Dam M, Swart NC, Willemsen A and Greve J, Cytometry, 1987, 8, 445–452. [PubMed: 2444397]

322. Webb DJ and Brown CM, in Cell Imaging Techniques: Methods and Protocols, Humana Press, Totowa, NJ, 2013, DOI: 10.1007/978-1-62703-056-4_2, pp. 29–59.
323. Paddock SW, Mol. Biotechnol, 2000, 16, 127–149. [PubMed: 11131973]
324. Maddox AS and Maddox PS, in Methods Cell Biol, Academic Press, 2012, vol. 107, pp. 1–34. [PubMed: 22226519]
325. Larson AM, Nat. Photonics, 2011, 5, 1.
326. So PTC, Dong CY, Masters BR and Berland KM, Annu. Rev. Biomed. Eng, 2000, 2, 399–429. [PubMed: 11701518]
327. Li L, Guo W, Yan Y, Lee S and Wang T, Light Sci. Appl, 2013, 2, e104–e104.
328. Galbraith CG and Galbraith JA, J. Cell. Sci, 2011, 124, 1607–1611. [PubMed: 21536831]
329. Perinetti G, Müller T, Spaar A, Polishchuk R, Luini A and Egner A, Traffic, 2009, 10, 379–391. [PubMed: 19170980]
330. Pullman JM, Nylk J, Campbell EC, Gunn-Moore FJ, Prystowsky MB and Dholakia K, Biomed. Opt. Express, 2016, 7, 302–311. [PubMed: 26977341]
331. Willig KI, Rizzoli SO, Westphal V, Jahn R and Hell SW, Nature, 2006, 440, 935–939. [PubMed: 16612384]
332. Cool SK, Breyne K, Meyer E, De Smedt SC and Sanders NN, J. Fluoresc, 2013, 23, 909–920. [PubMed: 23579930]
333. Lesser M, in High Performance Silicon Imaging, Woodhead Publishing, 2014, DOI: 10.1533/9780857097521.1.78, pp. 78–97.
334. Spring BQ, Abu-Yousif AO, Palanisami A, Rizvi I, Zheng X, Mai Z, Anbil S, Sears RB, Mensah LB, Goldschmidt R, Erdem SS, Oliva E and Hasan T, Proc. Natl. Acad. Sci. U S A, 2014, 111, E933–E942. [PubMed: 24572574]
335. Oh G, Chung E and Yun SH, Opt. Fiber Technol, 2013, 19, 760–771.
336. Horgan CC, Bergholt MS, Nagelkerke A, Thin MZ, Pence IJ, Kauscher U, Kalber TL, Stuckey DJ and Stevens MM, Theranostics, 2021, 11, 2006–2019. [PubMed: 33408795]
337. Wang W, Zhao J, Short M and Zeng H, J. Biophotonics, 2015, 8, 527–545. [PubMed: 25220508]
338. Seo SH, Kim BM, Joe A, Han HW, Chen X, Cheng Z and Jang ES, Biomaterials, 2014, 35, 3309–3318. [PubMed: 24424205]
339. Cordero E, Latka I, Matthaus C, Schie I and Popp J, J. Biomed. Opt., 2018, 23, 1–23.
340. Yi X, Wang F, Qin W, Yang X and Yuan J, Int. J. Nanomedicine, 2014, 9, 1347–1365. [PubMed: 24648733]
341. Li J-B, Liu H-W, Fu T, Wang R, Zhang X-B and Tan W, Trends Chem, 2019, 1, 224–234. [PubMed: 32864595]
342. Wang L, Du W, Hu Z, Uvdal K, Li L and Huang W, Angew. Chem. Int. Ed. Engl, 2019, 58, 14026–14043. [PubMed: 30843646]
343. Weinstain R, Slanina T, Kand D and Klan P, Chem. Rev, 2020, 120, 13135–13272. [PubMed: 33125209]
344. Wang H, Zhao E, Lam JWY and Tang BZ, Mater. Today, 2015, 18, 365–377.
345. Xu W, Wang D and Tang BZ, Angew. Chem. Int. Ed. Engl, 2021, 60, 7476–7487. [PubMed: 32515530]
346. Liu L-J, Liu W, Ji G, Wu Z-Y, Xu B, Qian J and Tian W-J, Chinese J. Polym. Sci, 2019, 37, 401–408.
347. Zhao P, He K, Han Y, Zhang Z, Yu M, Wang H, Huang Y, Nie Z and Yao S, Anal. Chem, 2015, 87, 9998–10005. [PubMed: 26358143]
348. Zhao P, Xu Q, Tao J, Jin Z, Pan Y, Yu C and Yu Z, WIREs Nanomed. Nanobi, 2018, 10, e1483.
349. Chinnathambi S and Shirahata N, Sci. Technol. Adv. Mater, 2019, 20, 337–355. [PubMed: 31068983]
350. Montalti M, Cantelli A and Battistelli G, Chem. Soc. Rev, 2015, 44, 4853–4921. [PubMed: 26051500]
351. Bao X, Yuan Y, Chen J, Zhang B, Li D, Zhou D, Jing P, Xu G, Wang Y, Hola K, Shen D, Wu C, Song L, Liu C, Zboril R and Qu S, Light Sci. Appl, 2018, 7, 91. [PubMed: 30479757]

352. Zheng P and Wu N, Chem. Asian. J, 2017, 12, 2343–2353. [PubMed: 28742956]
353. Shamsi J, Urban AS, Imran M, De Trizio L and Manna L, Chem. Rev, 2019, 119, 3296–3348. [PubMed: 30758194]
354. Protesescu L, Yakunin S, Bodnarchuk MI, Krieg F, Caputo R, Hendon CH, Yang RX, Walsh A and Kovalenko MV, Nano Lett, 2015, 15, 3692–3696. [PubMed: 25633588]
355. Shu X, Royant A, Lin MZ, Aguilera TA, Lev-Ram V, Steinbach PA and Tsien RY, Science, 2009, 324, 804–807. [PubMed: 19423828]
356. Yu D, Gustafson WC, Han C, Lafaye C, Noirclerc-Savoye M, Ge W-P, Thayer DA, Huang H, Kornberg TB, Royant A, Jan LY, Jan YN, Weiss WA and Shu X, Nat. Commun, 2014, 5, 3626. [PubMed: 24832154]
357. Li C, Cao L, Zhang Y, Yi P, Wang M, Tan B, Deng Z, Wu D and Wang Q, Small, 2015, 11, 4517–4525. [PubMed: 26058947]
358. Huang LY, Zhu S, Cui R and Zhang M, Anal. Chem, 2020, 92, 535–542. [PubMed: 31756071]
359. Kim DE, Schellingerhout D, Jaffer FA, Weissleder R and Tung CH, J. Cereb. Blood Flow Metab, 2005, 25, 226–233. [PubMed: 15678125]
360. Zhang M, Yue J, Cui R, Ma Z, Wan H, Wang F, Zhu S, Zhou Y, Kuang Y, Zhong Y, Pang D-W and Dai H, Proc. Natl. Acad. Sci. U S A, 2018, 115, 6590–6595. [PubMed: 29891702]
361. Ando J, Fujita K, Smith NI and Kawata S, Nano Lett, 2011, 11, 5344–5348. [PubMed: 22059676]
362. Harmsen S, Huang R, Wall MA, Karabeber H, Samii JM, Spaliviero M, White JR, Monette S, O'Connor R, Pitter KL, Sastra SA, Saborowski M, Holland EC, Singer S, Olive KP, Lowe SW, Blasberg RG and Kircher MF, Nat. Biotechnol, 2015, 7, 271ra277–271ra277.
363. Huang JY, Zong C, Xu LJ, Cui Y and Ren B, Chem. Commun, 2011, 47, 5738–5740.
364. Wei T, Xing H, Wang H, Zhang Y, Wang J, Shen J and Dai Z, Talanta, 2020, 210, 120625. [PubMed: 31987166]
365. Huefner A, Kuan WL, Barker RA and Mahajan S, Nano lett, 2013, 13, 2463–2470. [PubMed: 23638825]
366. Chang J, Zhang A, Huang Z, Chen Y, Zhang Q and Cui D, Talanta, 2019, 198, 45–54. [PubMed: 30876586]
367. Ghosh D, Bagley AF, Na YJ, Birrer MJ, Bhatia SN and Belcher AM, Proc. Natl. Acad. Sci. U S A, 2014, 111, 13948–13953. [PubMed: 25214538]
368. Qian X, Peng X-H, Ansari DO, Yin-Goen Q, Chen GZ, Shin DM, Yang L, Young AN, Wang MD and Nie S, Nat. Biotechnol,2008, 26, 83–90. [PubMed: 18157119]
369. Chen J, Sheng Z, Li P, Wu M, Zhang N, Yu XF, Wang Y, Hu D, Zheng H and Wang GP, Nanoscale, 2017, 9, 11888–11901. [PubMed: 28561825]
370. Jaworska A, Jamieson LE, Malek K, Campbell CJ, Choo J, Chlopicki S and Baranska M, Analyst, 2015, 140, 2321–2329. [PubMed: 25485622]
371. Puppulin L, Hosogi S, Sun H, Matsuo K, Inui T, Kumamoto Y, Suzaki T, Tanaka H and Marunaka Y, Nat. Commun, 2018, 9, 5278. [PubMed: 30538244]
372. Zhang J, Liu Z, Lian P, Qian J, Li X, Wang L, Fu W, Chen L, Wei X and Li C, Chem. Sci, 2016, 7, 5995–6005. [PubMed: 30034741]
373. Tang B, Yu F, Li P, Tong L, Duan X, Xie T and Wang X, J. Am. Chem. Soc, 2009, 131, 3016–3023. [PubMed: 19199620]
374. Dong B, Song X, Wang C, Kong X, Tang Y and Lin W, Anal. Chem, 2016, 88, 4085–4091. [PubMed: 26987045]
375. Song J, Zhou J and Duan H, J. Am. Chem. Soc, 2012, 134, 13458–13469. [PubMed: 22831389]
376. Yin J, Kong X and Lin W, Anal. Chem, 2021, 93, 2072–2081 [PubMed: 33393756]
377. Zhou Y, Yu S, Shang J, Chen Y, Wang Q, Liu X and Wang F, Anal. Chem, 2020, 92, 15069–15078. [PubMed: 33141555]
378. Hwang DW, Kim HY, Li F, Park JY, Kim D, Park JH, Han HS, Byun JW, Lee Y-S, Jeong JM, Char K and Lee DS, Biomaterials, 2017, 121, 144–154. [PubMed: 28088076]
379. Fu W, Yan C, Guo Z, Zhang J, Zhang H, Tian H and Zhu W-H, J. Am. Chem. Soc, 2019, 141, 3171–3177. [PubMed: 30632737]

380. Yan R, Hu Y, Liu F, Wei S, Fang D, Shuhendler AJ, Liu H, Chen H-Y and Ye D, J. Am. Chem. Soc, 2019, 141, 10331–10341. [PubMed: 31244188]

381. Gao X and Wu N, Electrochem. Soc. Interface, 2016, 25, 79–81.

382. Point of Care/Rapid Diagnostics Market, https://www.marketsandmarkets.com/Market-Reports/point-of-care-diagnostic-market-106829185.html

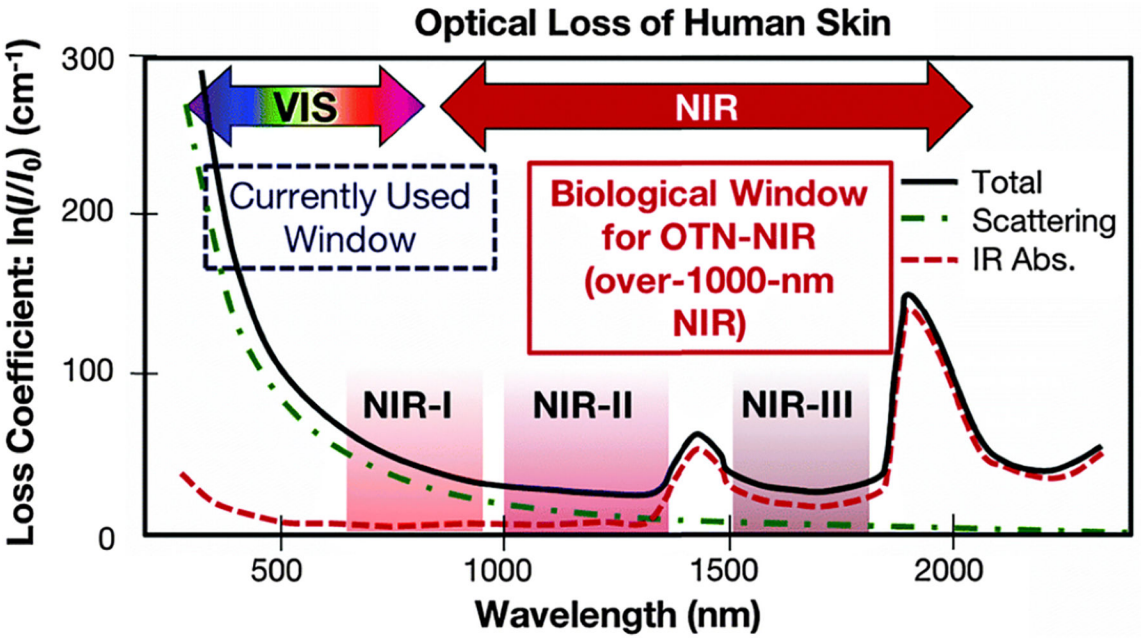

Figure 1.
Optical loss of human skin. Reproduced from Ref. 16, copyright 2016, The Royal Society of Chemistry.

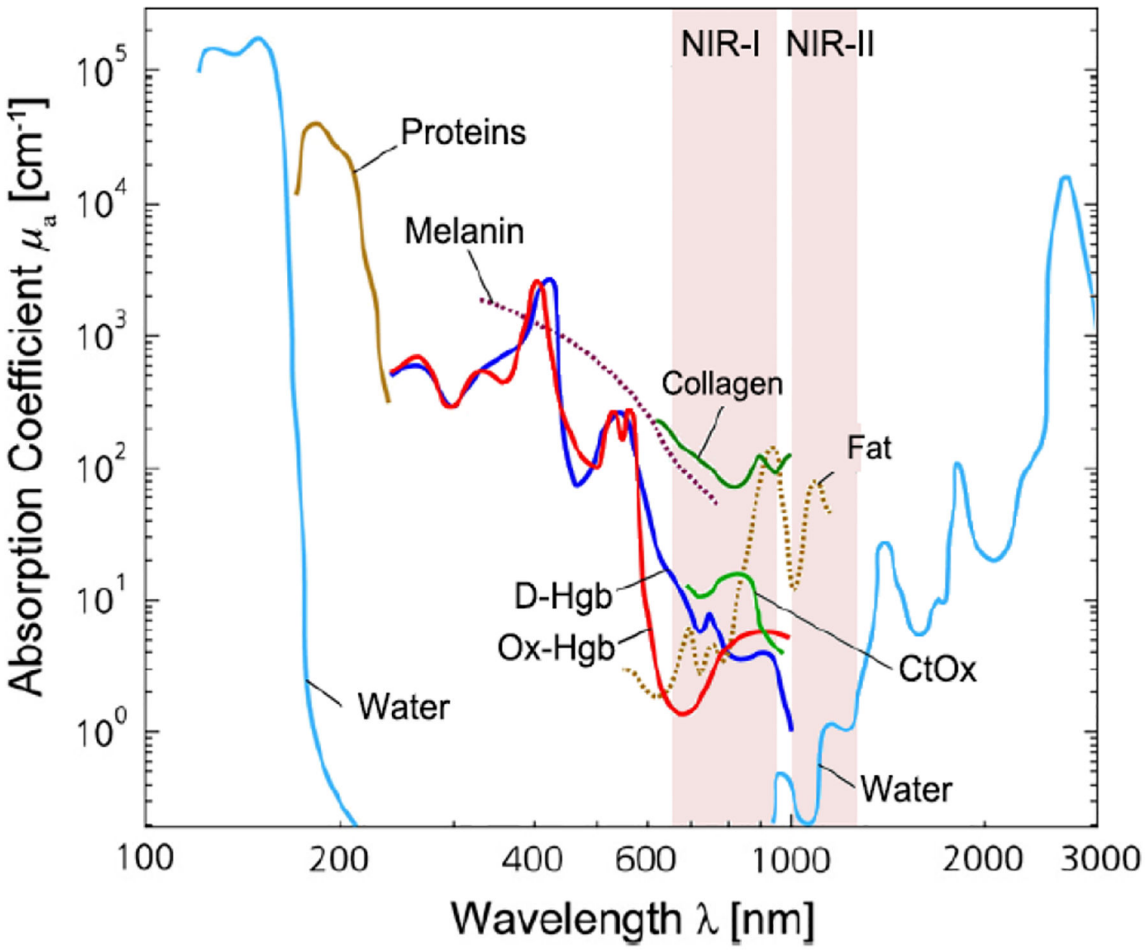

Figure 2.

Light absorption spectra with X-axis on the natural logarithm base for different chromophores present in human tissues. The shown are the spectra for oxy-hemoglobin (Ox-Hgb) and deoxy-hemoglobin (D-Hgb), proteins, water, collagen, fat and cytochrome oxidase (CtOx) in the region from 100 nm to 3000 nm with respect to the specific concentration in mM. This figure is further modified from Ref 20, copyright 2014, Elsevier.

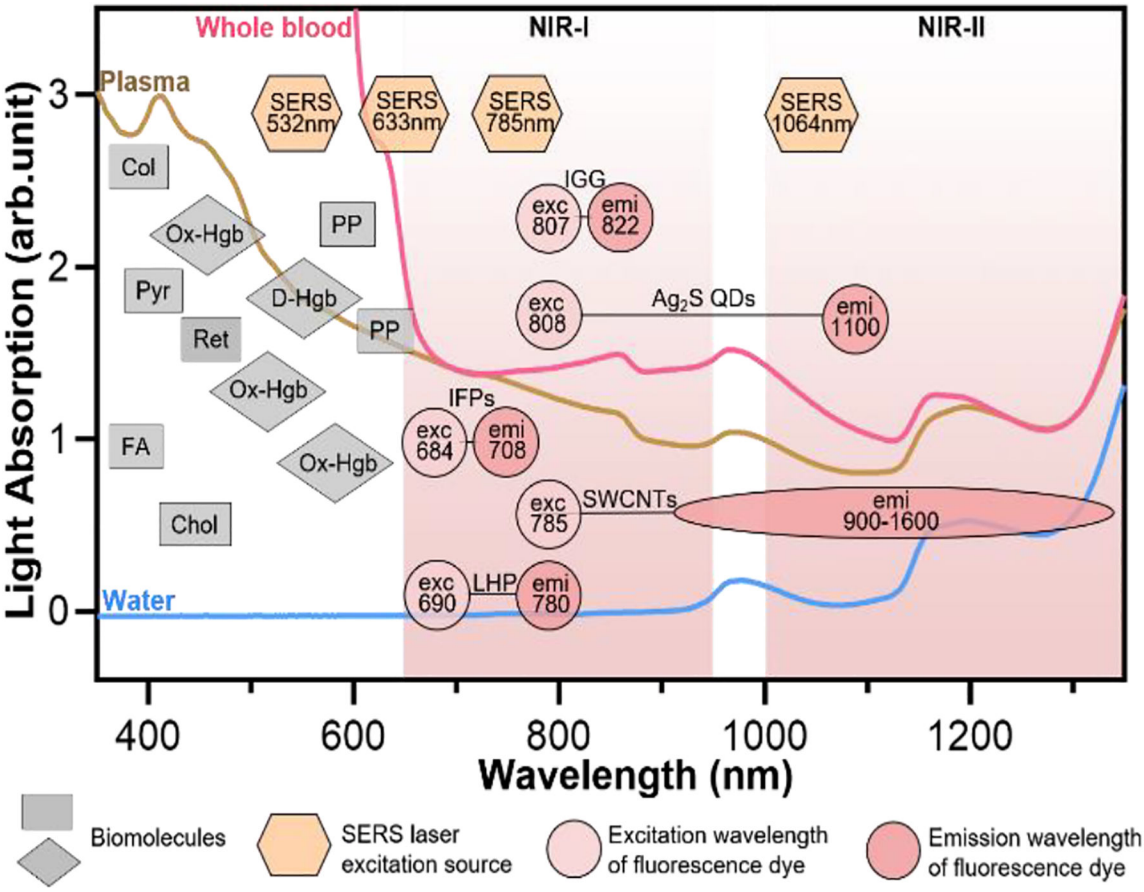

Figure 3.

Light absorption and autofluorescence species in human blood as well as excitation and emission wavelengths of common fluorophores and SERS probes. Rectangles represent auto-fluorescence spectral bands of plasma/blood proteins including pyridoxine (Pyr), retinol A (Ret), collagen (Col), cholecalciferol (Chol), folic acid (FA), and porphyrin (PP); Diamonds represent absorbent peaks of oxy-hemoglobin (OxHe) and deoxy-hemoglobin (D-He); Hexagons represent excitation wavelength of SERS probes; and circles represent excitation and emission of NIR fluorescence probes including indocyanine green (IGG), Ag_2S quantum dots (Ag_2S QDs), single-wall carbon nanotube (SWCNTs), infrared fluorescent proteins (IFPs) and lead halide perovskite (LHP). The light spectra in this figure were acquired in Wu's lab. Some data in this figure were taken from Ref. 21 with permission of Oxford University Press.

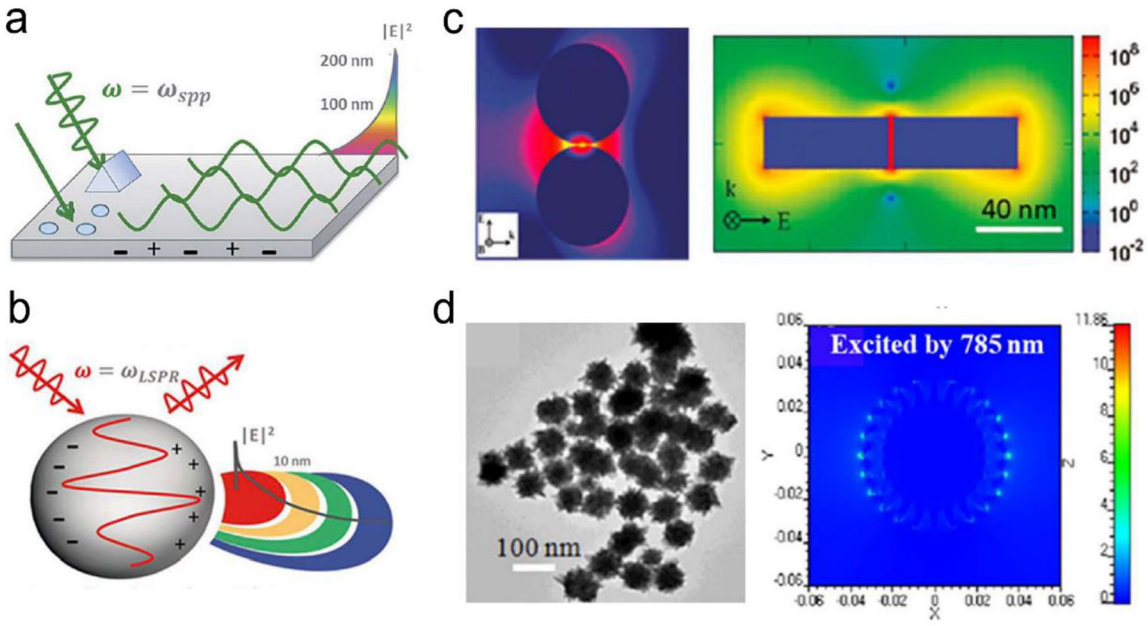

Figure 4.

(a) The SPP-induced EM field and the decay. (b) The LSPR-induced EM field and the decay. (c) Finite-difference time-domain (FDTD) simulated EM field distributions for NP with small gaps or sharp edges. (d) FDTD simulated EM field distributions for nanostars. Reproduced with permission from (a) ref. 32, copyright 2015, The Royal Society of Chemistry; (b) ref. 32, copyright 2015, The Royal Society of Chemistry; (c) ref. 44, copyright 2011, American Chemical Society; (d) ref. 45, copyright 2012, IOP Publishing Ltd.

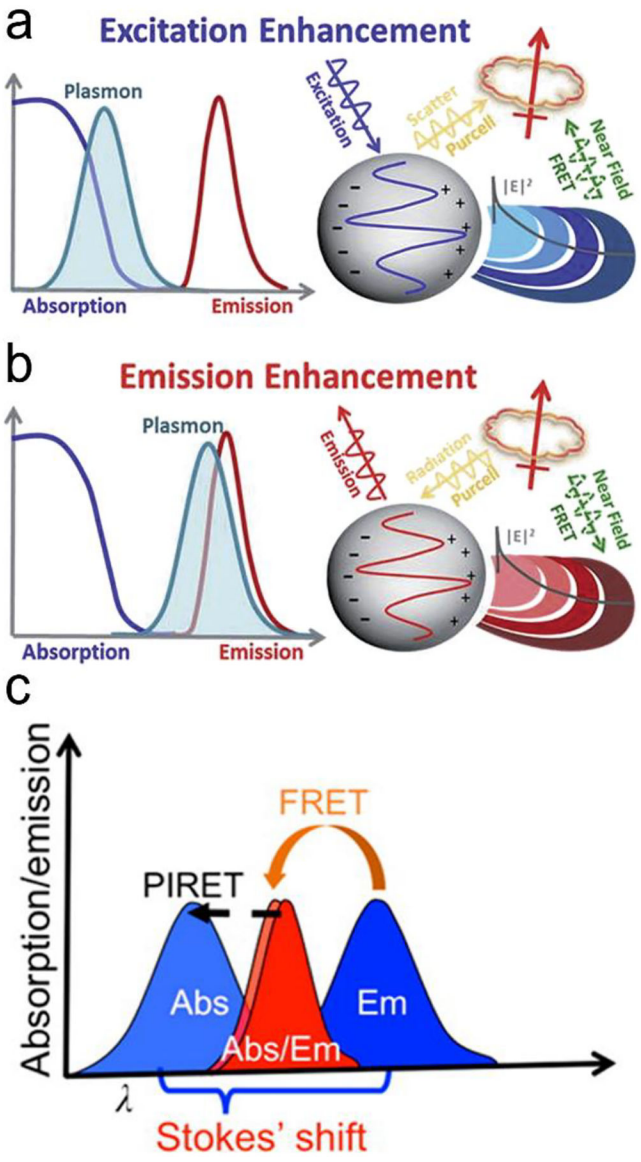

Figure 5.

Mechanisms of plasmon-enhanced fluorescence. (a) When the plasmon overlaps with fluorophore absorption spectrum, an enhanced fluorophore emission can be achieved. (b) when the plasmon overlaps with fluorophore emission spectrum, a quenching or enhancement of fluorophore emission can be achieved. (c) When the spectrum peak of plasmon is longer than the absorption of the fluorophore, fluorescent intensity can be enhanced through PIRET process if there is an overlap between plasmon spectrum and fluorophore absorption. Reproduced with permission from (a) ref. 32, copyright 2015, The Royal Society of Chemistry; (b) ref. 32, copyright 2015, The Royal Society of Chemistry; (c) ref. 45, copyright 2016, American Chemical Society.

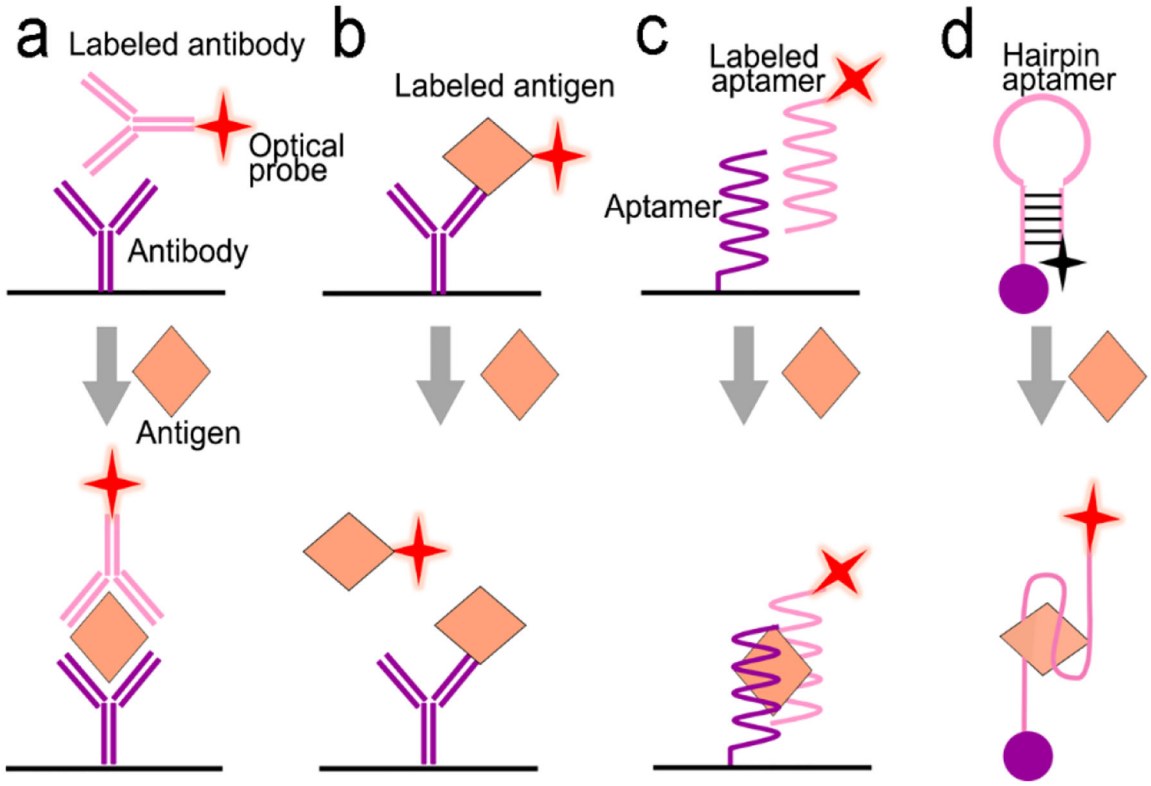

Figure 6.

Signal transduction modes/principles for protein detection. (a) sandwiched antibody-protein-antibody assay; (b) competitive assay; (c) sandwiched aptamer-protein-aptamer assay, and (d) aptamer beacon that can change its conformation.

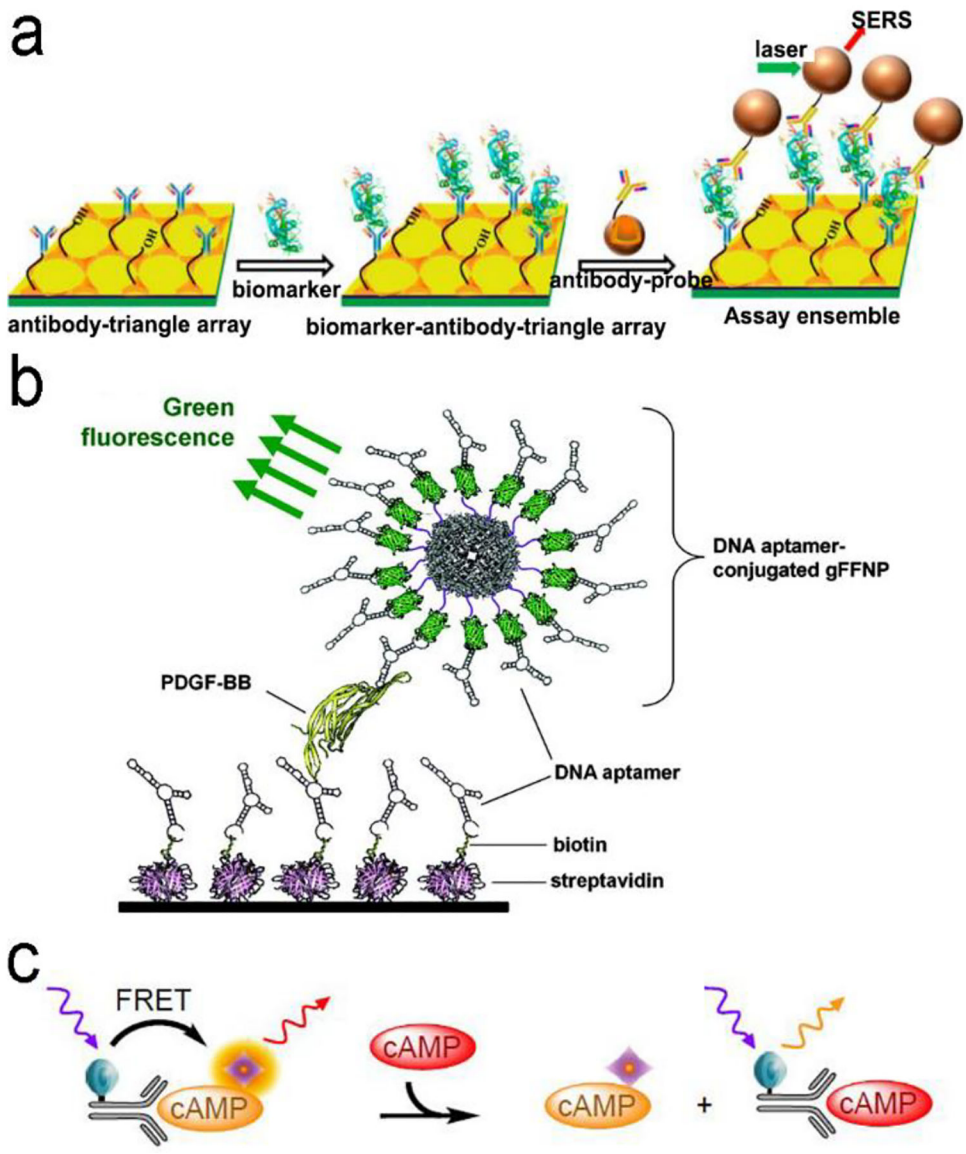

Figure 7.

(a) ELISA-like SERS immunosensor using antibody-antigen interaction for cancer biomarkers in blood plasma. (b) ELISA-like fluorescence immunosensor using aptamer-antigen interaction. (c) Competitive assay based on FRET mechanism. Reproduced with permission from (a) ref. 87, copyright 2013, American Chemical Society; (b) ref. 100, copyright 2011, American Chemical Society; (c) ref. 102, copyright 2014, MDPI.

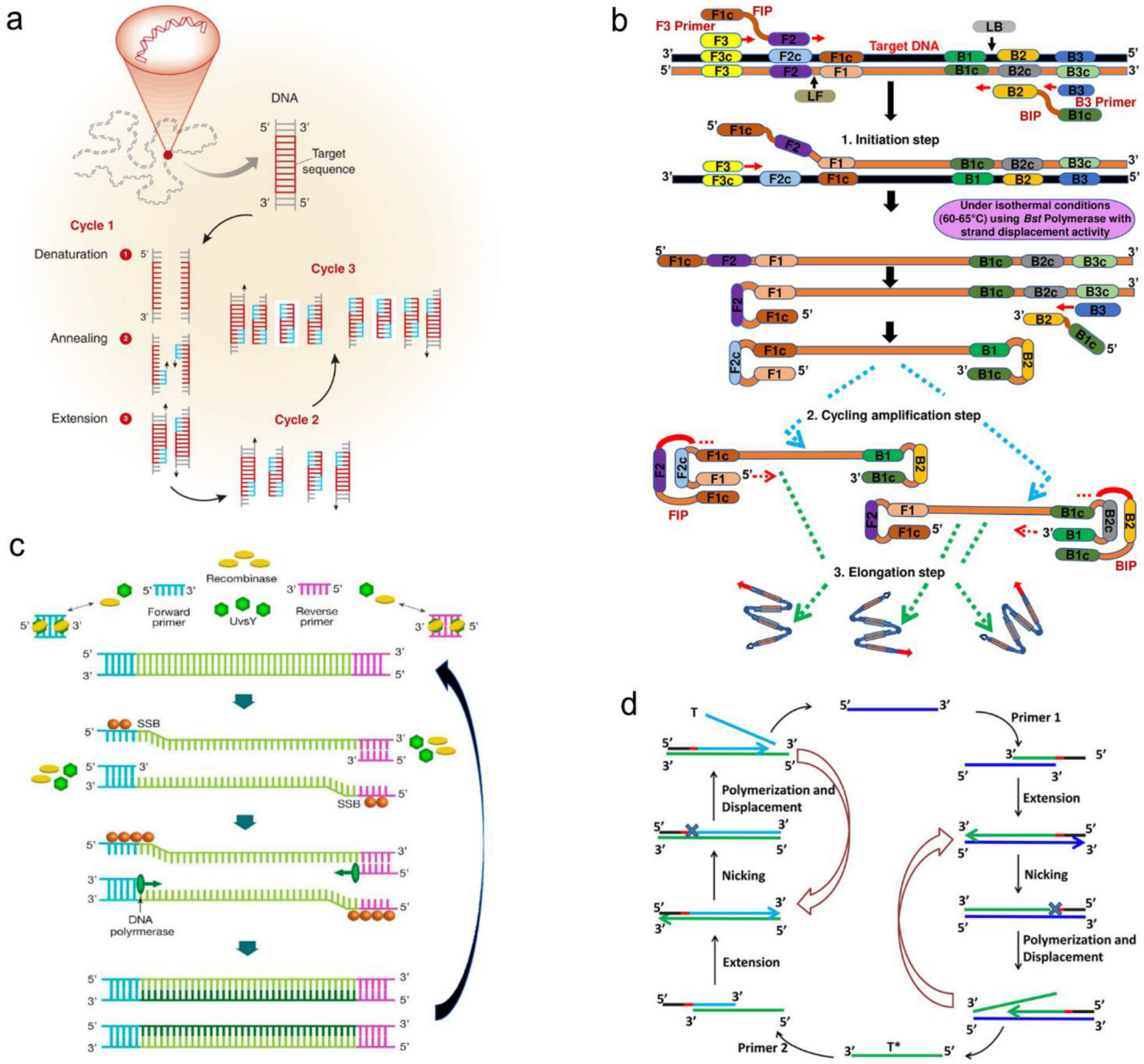

Figure 8.

Schematic illustration of nucleic acid amplification. (a) Polymerase chain reaction (PCR). (b) Loop-mediated isothermal amplification (LAMP). (c) Recombinase polymerase amplification (RPA). (d) Strand displacement amplification (SDA). Reproduced with permission from (a) ref. 118, copyright 2013, Elsevier; (b) ref. 123, copyright 2019, PLOS; (c) ref. 125, copyright 2020, MDPI; (d) ref. 120, copyright 2014, American Chemical Society.

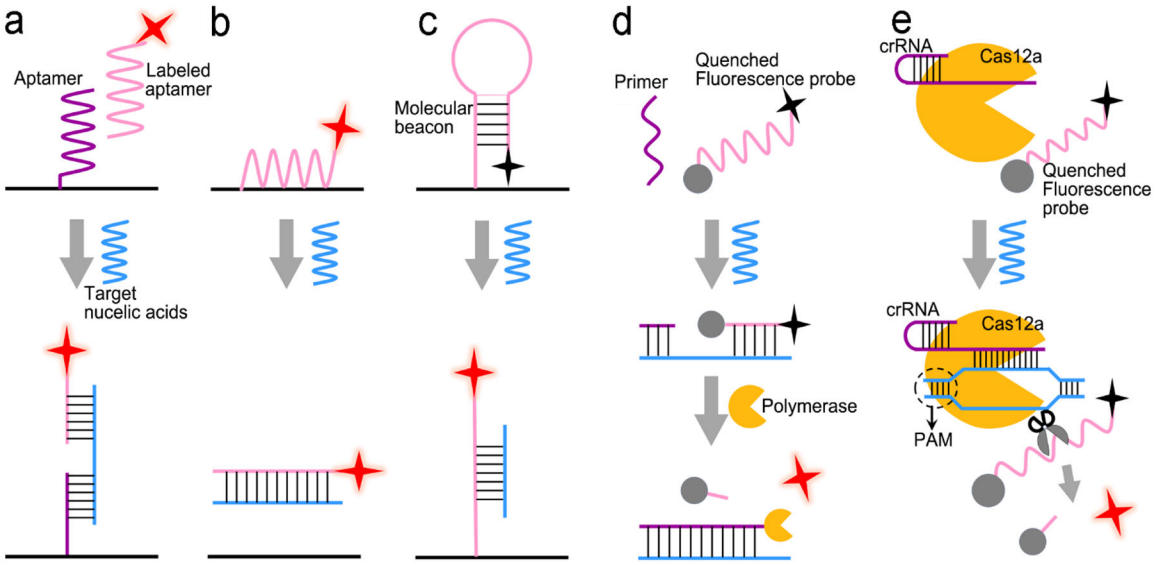

Figure 9.

Signal transduction modes for nucleic acid detection. (a) “Three-strand” hybridization mode; (b) “Two-strand” hybridization mode-based competitive assay; (c) “Molecular beacon” mode; (d) Enzyme-assisted assay using polymerase; (e). Enzyme-assisted assay using CRISPR/Cas12a

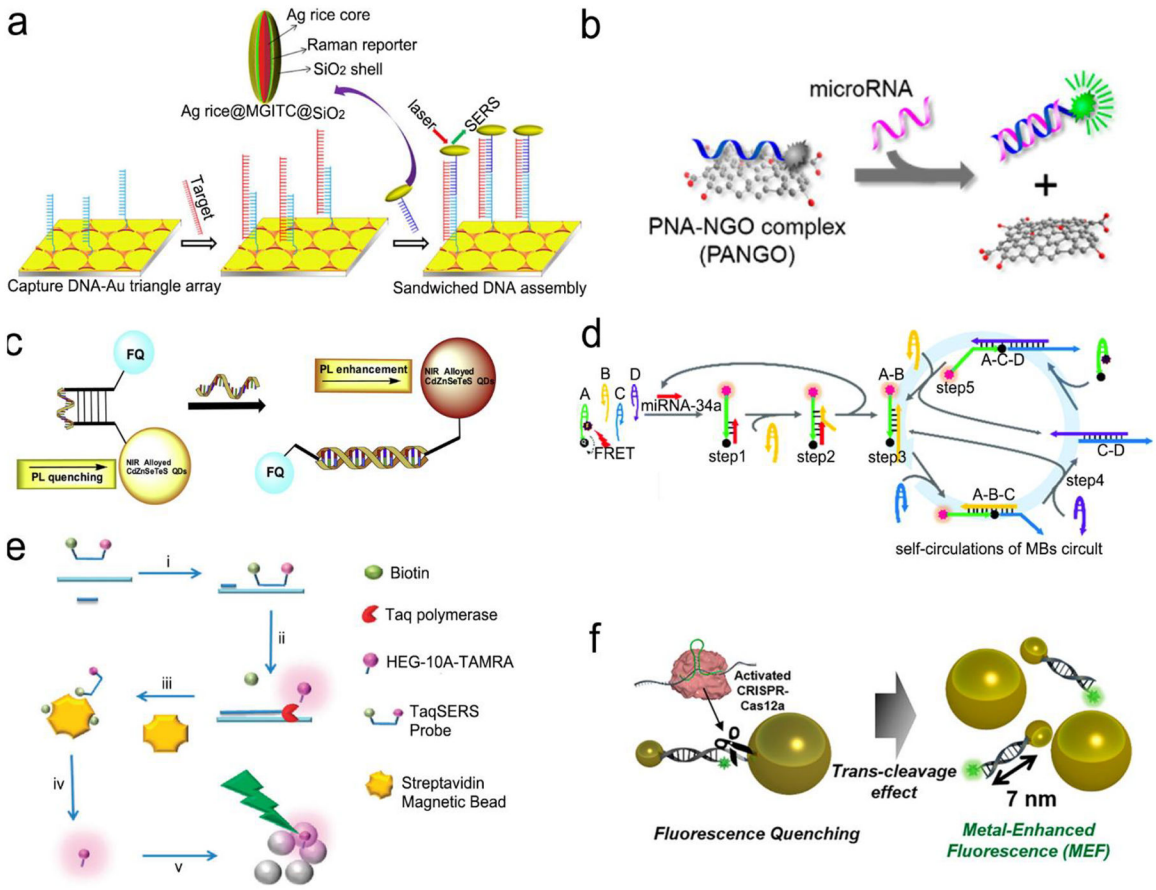

Figure 10.

Nucleic acid detection with SERS or fluorescent sensors. (a) “Three-strand” hybridization assay using SERS probes for detection of Hepatitis B Virus DNA. (b) “Two-strand” hybridization mode-based competitive interaction between single-strand and double-stranded complex graphene oxide. (c) “Molecular beacon” mode for detection of influenza virus RNA. (d) Nucleic acid amplification and test (NAAT) using self-circulation of chain reaction for signal amplification and “molecule beacon” mode for detection. (e) Taq polymerase-assisted assay. (f) CRISPR/Cas12a assisted assay with fluorescence probes determined by the size of metal nanoparticles and their distance. Reproduced with permission from (a) ref. 112, copyright 2013, American Chemical Society; (b) ref. 132, copyright 2013, American Chemical Society; (c) ref. 136, copyright 2016, Elsevier; (d) ref. 135, copyright 2019, The Royal Society of Chemistry; (e) ref. 137, copyright 2012, The Royal Society of Chemistry; (f) ref. 138, copyright 2020, American Chemical Society.

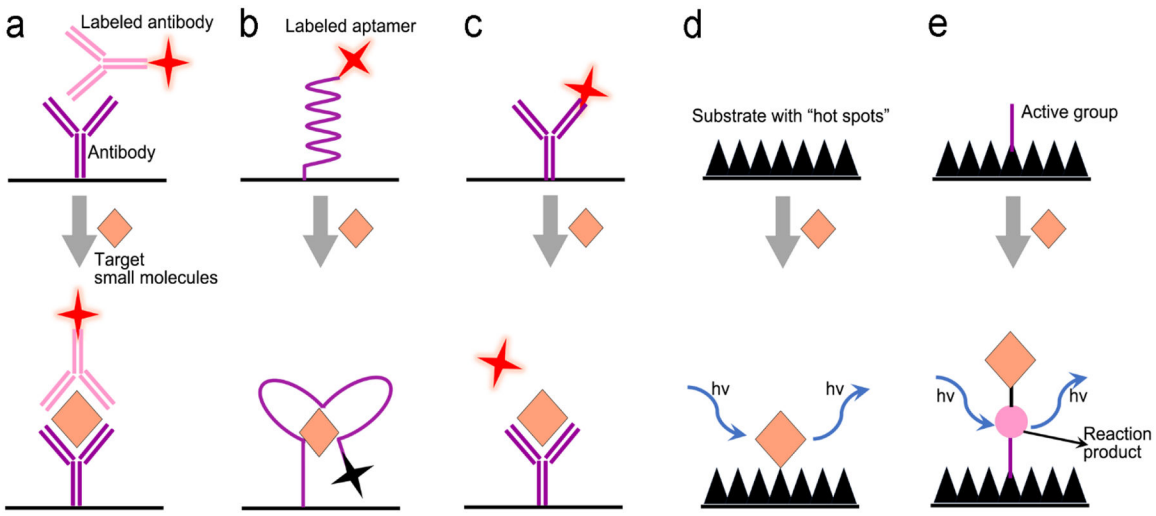

Figure 11.

Signal transduction modes for small molecule detection. (a) Sandwiched antibody-molecule-antibody assay; (b) Molecular beacon assay; (c) Competitive assay; (d) Direct detection using substrate with "hot spots" to enhance Raman scattering; (e) Target detection through monitoring their chemical reaction product using SERS sensor.

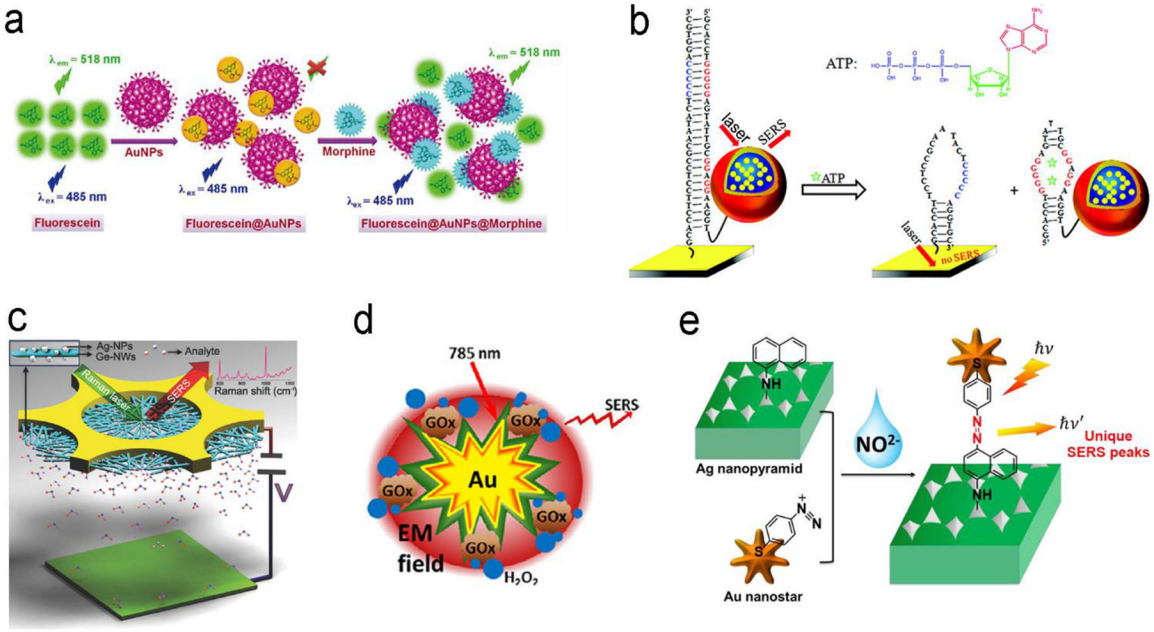

Figure 12.

Detection of small molecules with fluorescence or SERS sensors. (a) Competitive assay based on different affinity of fluorescein and morphine to Au nanoparticles. (b) Molecular beacon assay using SERS probe-linked aptamer for ATP detection. (c) SERS sensors with a “built-in” electrostatic preconcentration unit for capture of antibiotic analyte. (d) *in situ* generation and detection of SERS-active H_2O_2 for glucose detection. (e) *in situ* generation of SERS-active azo-moieties for nitrite detection. Reproduced with permission from (a) ref. 175, copyright 2018, Springer Nature; (b) ref. 64, copyright 2012, American Chemical Society; (c) ref. 166, copyright 2017, Wiley-VCH; (d) ref. 149, copyright 2014, Elsevier; (e) ref. 70, copyright 2018, Elsevier.

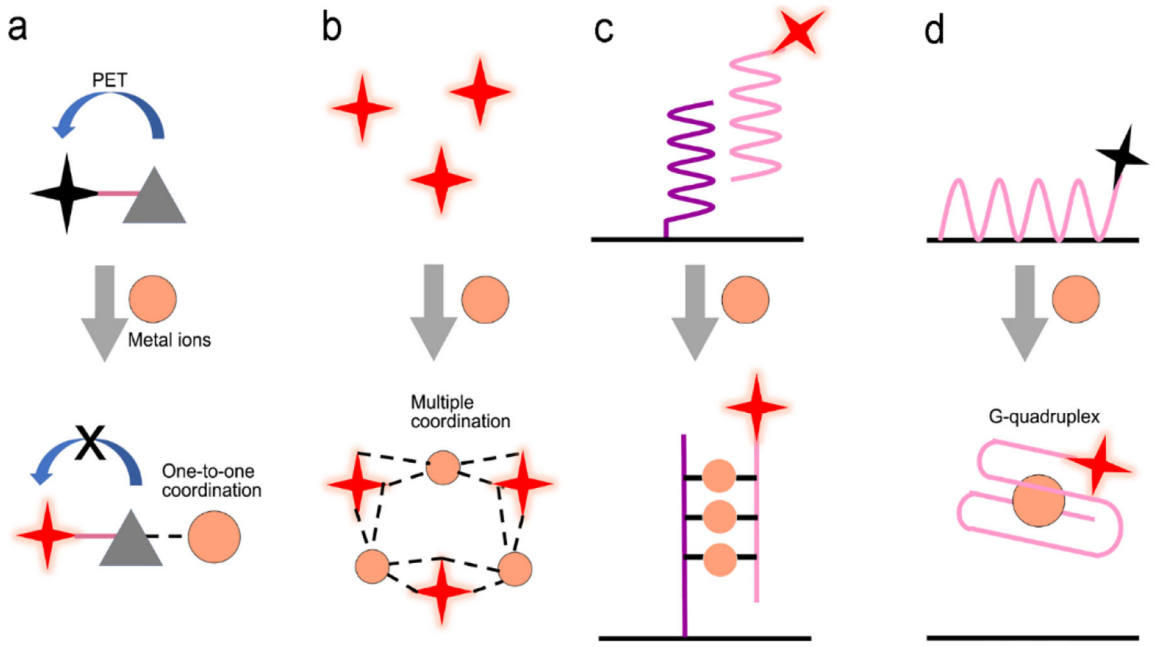

Figure 13.

Signal transduction modes/principles in SERS or fluorescence sensors for metal ion detection. (a) “One-to-one” model using single coordinate site between optical probe and target ion; (b) Aggregation of optical probes induced by multiple coordinate sites; (c) DNA hybridization assay; (d) Molecular beacon-based competitive assay.

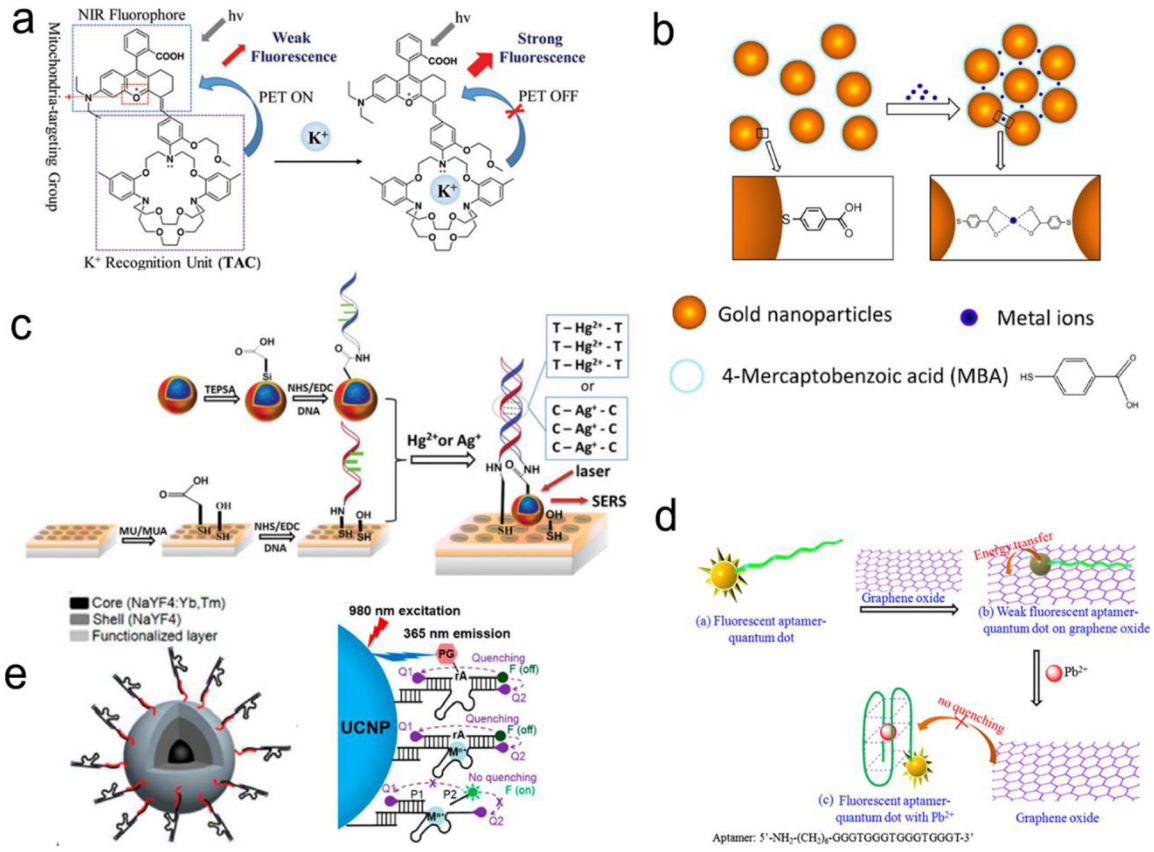

Figure 14.

Detection of metal ions by formation of metal ion-ligand complexes. (a) Coordination complex formed with one metal ion and one fluorescence probe, inhibiting photo-induced electron transfer (PET) to enhance the intensity of fluorescence. (b) Coordinate interaction induced aggregation of gold nanoparticles for SERS enhancement. (c) SERS probes coupled with an ordered Au nanohole array. (d) Competitive assay by formation of G-quadruplex/Pb^{2+} complex. (e) Catalytic nucleic acids (DNAzymes) activity activated by specific metal ions. Reproduced with permission from (a) ref. 181, copyright 2020, The Royal Society of Chemistry; (b) ref. 188, copyright 2017, IOP; (c) ref. 69, copyright 2015, The Royal Society of Chemistry; (d) ref. 189, copyright 2013, Elsevier; (e) ref. 190, copyright 2018, American Chemical Society.

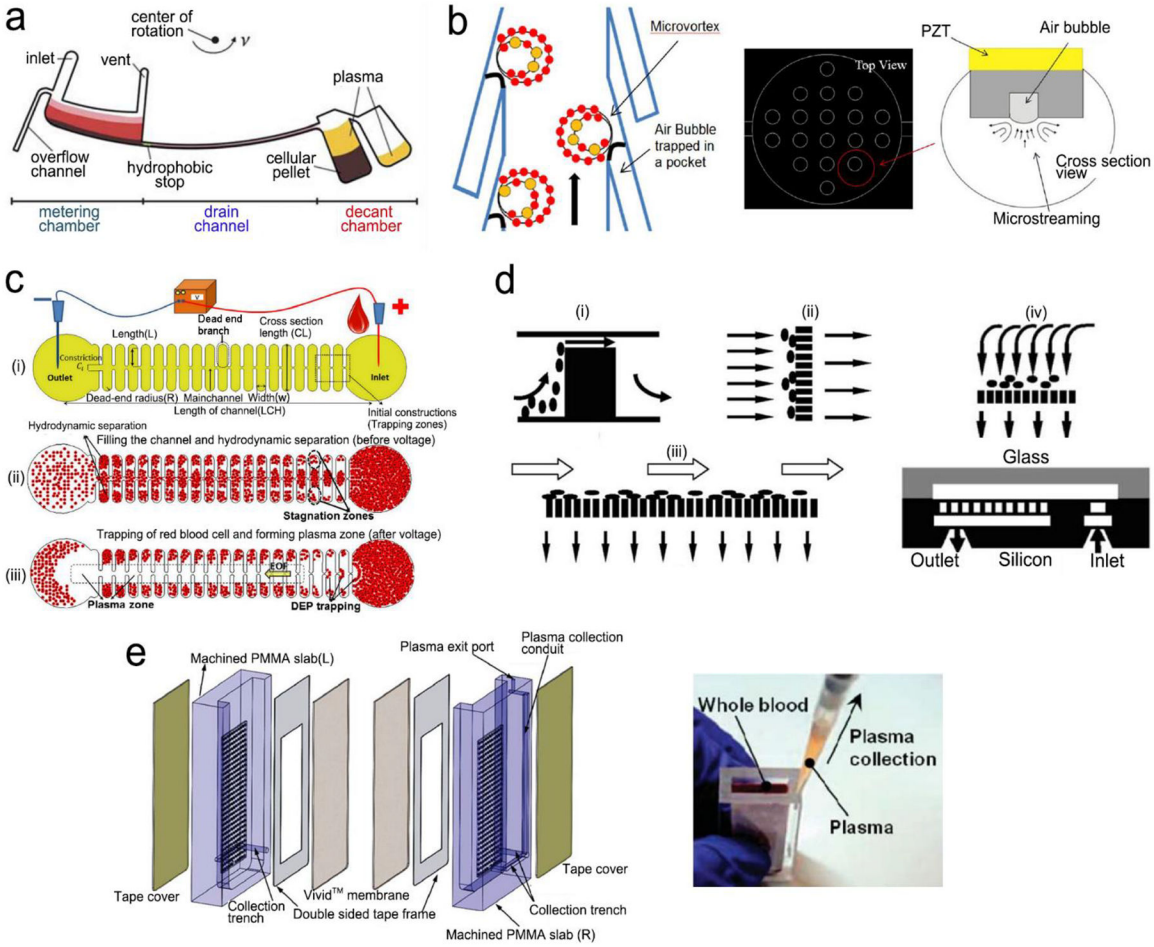

Figure 15.

On-chip plasma separation methods including active (a-c) and passive (d, e) methods: (a) Centrifugal separation in a CD-shaped disk. (b) Acoustic microstreaming vortex to trap blood cells. (c) Dielectrophoresis-induced plasma separation. (d) Silicon-based microfilter including (i) weir-type filter, (ii) pillar-type filter, (iii) cross-flow filter, and (iv) membrane filter. (e) Dual separation by combination of sedimentation and membrane filtration. Reproduced with permission from (a) ref. 226, copyright 2006, The Royal Society of Chemistry; (b) ref. 227, copyright 2021, Elsevier; (c) ref. 228, copyright 2015, Springer Nature; (d) ref. 229, copyright 2008, Springer Nature; (e) ref. 238, copyright 2013, American Chemical Society.

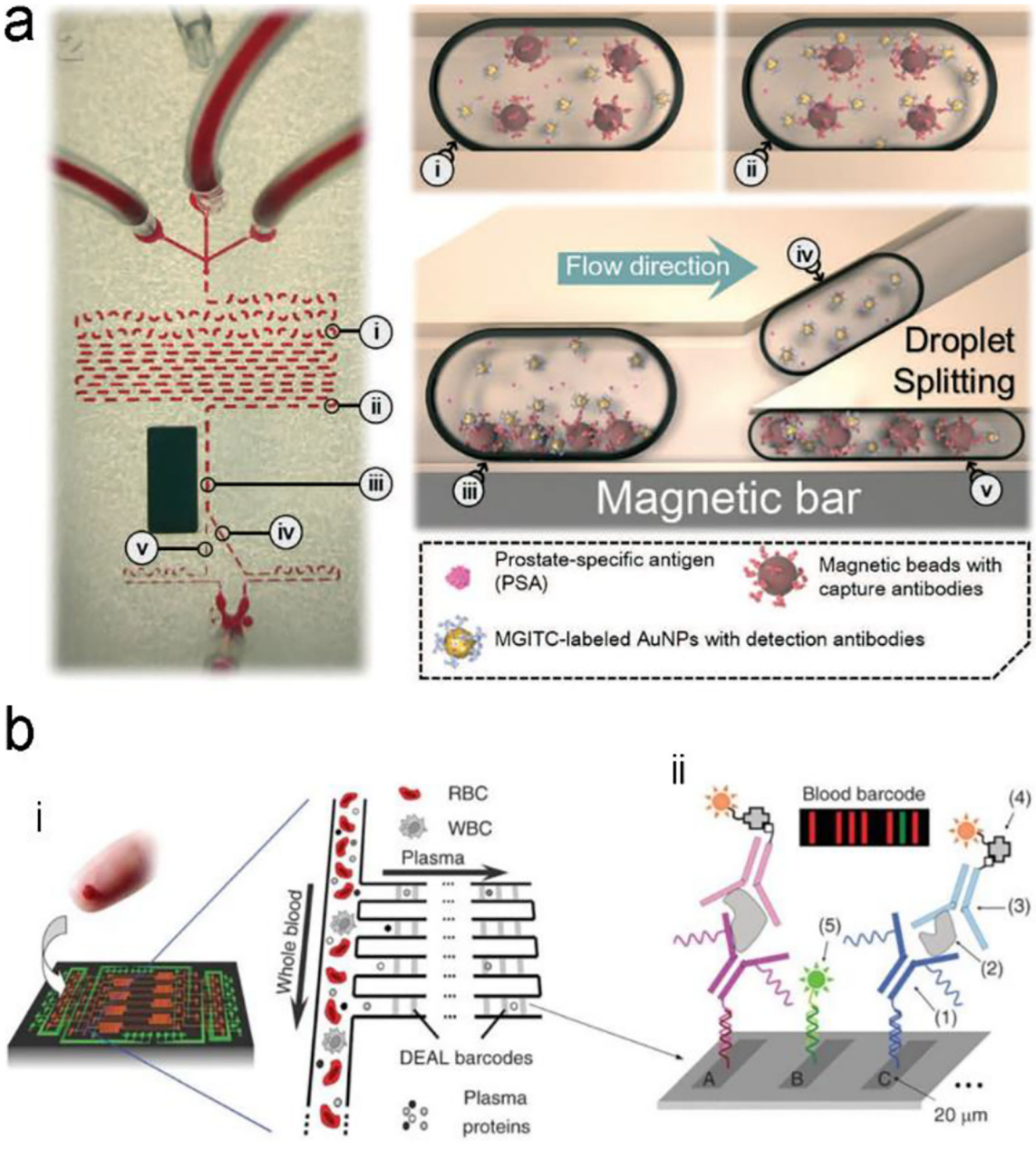

Figure 16.

A typical structure of active optofluidic device for protein detection. (a) SERS-based microdroplet device for detection of prostate-specific antigen (PSA) cancer markers. It has 5 compartments with different functions: (i) generating microdroplet and mixing reagents; (ii) forming immunocomplexes on magnetic beads; (iii) separating immunocomplexes by magnetic bar; (iv) moving the supernatant that contained the unbound SERS probes; and (v) separating magnetic immunocomplexes through droplet splitting. (b) In vitro fluorescence microfluidic device for multiplexed detection of proteins in finger-prick whole blood. Reproduced with permission from (a) ref. 218, copyright 2016, The Royal Society of Chemistry; (b) ref. 235, copyright 2008, Springer Nature.

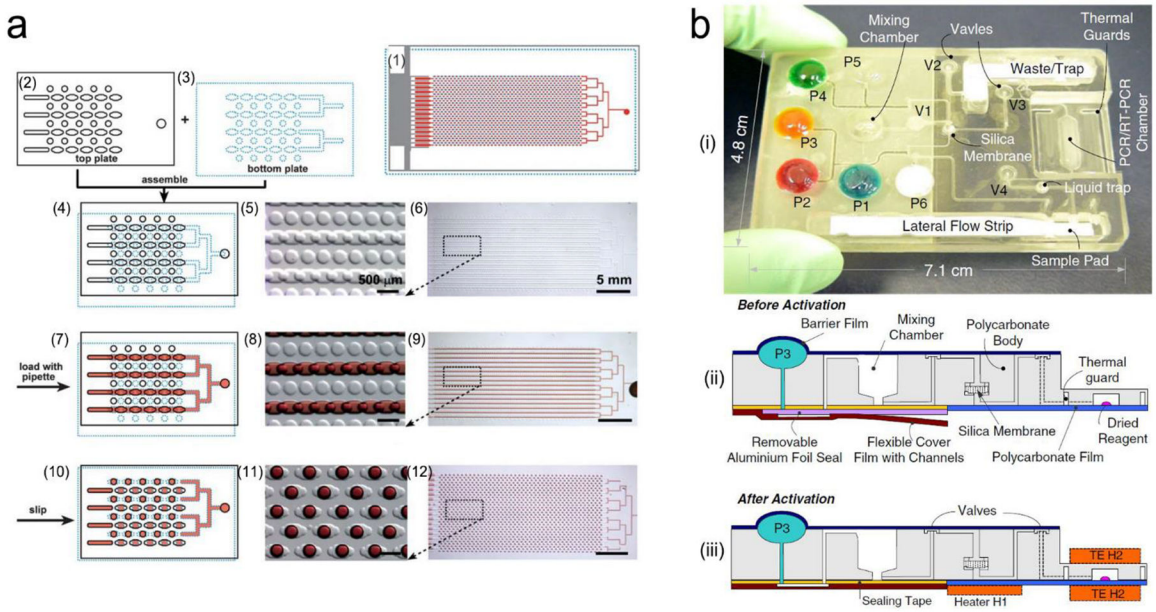

Figure 17.

Integrated microfluidic devices for nucleic acid testing. (a) Schematic digital PCR process with SlipChip: (1) assembled SlipChip after splitting; (2) and (3) the top plate and the bottom plate, respectively; (4–6) overlapping of the top and bottom plates to form a continuous fluidic path; (7–9) The aqueous reagent (red) filling the SlipChip through the connected elongated wells; (10–12) aqueous droplets formed in each compartment after splitting. (b) A self-contained microfluidic cassette integrated separation, amplification, and detection of nucleic acids. Reproduced with permission from (a) ref. 253, copyright 2010, The Royal Society of Chemistry; (b) ref. 267, copyright 2010, Springer Nature.

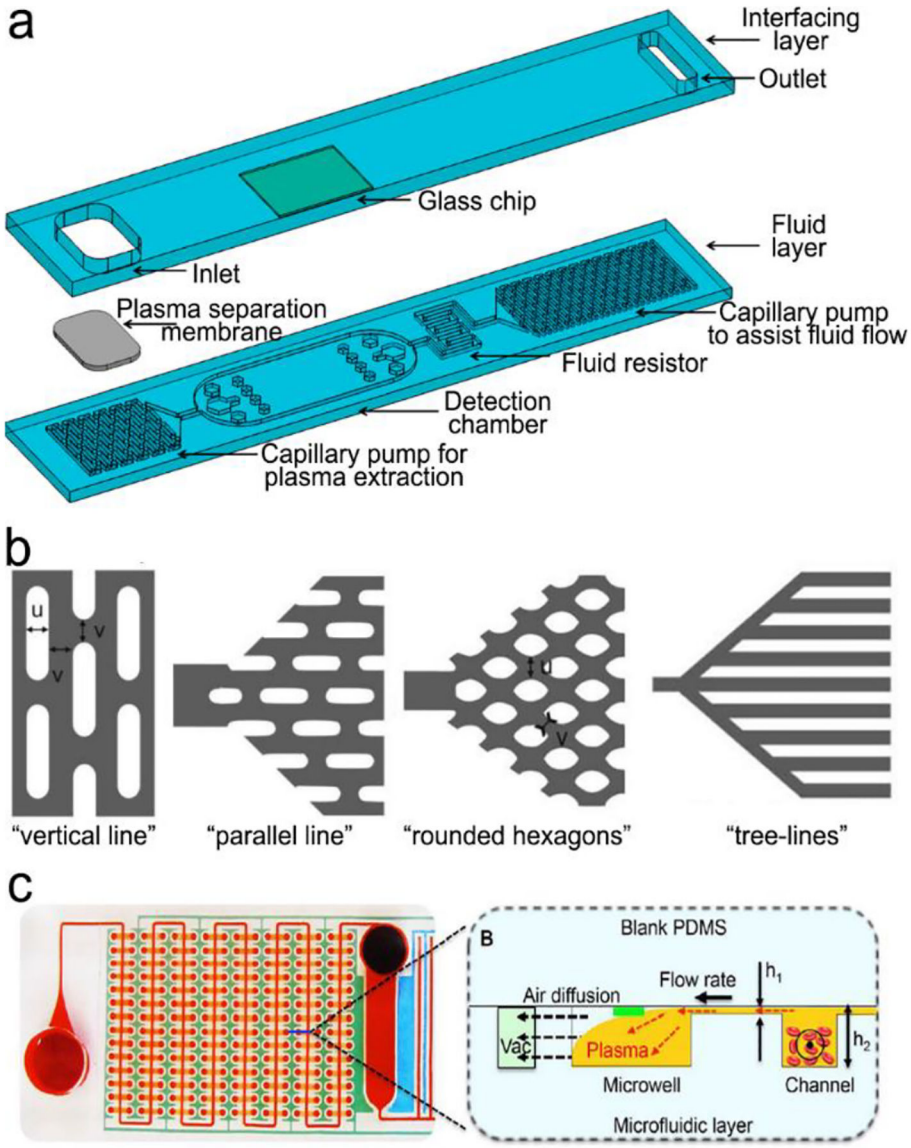

Figure 18.

(a) Basic structure of plastic-/glass-based lateral flow device. It is composed of interfacing layer (cover layer) and fluid layer. The fluid layer contains four main functional zones, including a pretreatment unit (plasma separation and extraction), a detection chamber, a fluid resistor and a "built-in" micropump. (b) and (c) examples of "built-in" micropumps: (b) capillary pumps such as "vertical lines", "parallel lines", "rounded hexagons" and "tree lines". (c) A pneumatic pump fabricated by multiple vacuum pillars. Reproduced with permission from (a) ref. 272, copyright 2017, MDPI; (b) ref. 273, copyright 2007, The Royal Society of Chemistry; (c) ref. 274, copyright 2017, The Royal Society of Chemistry.

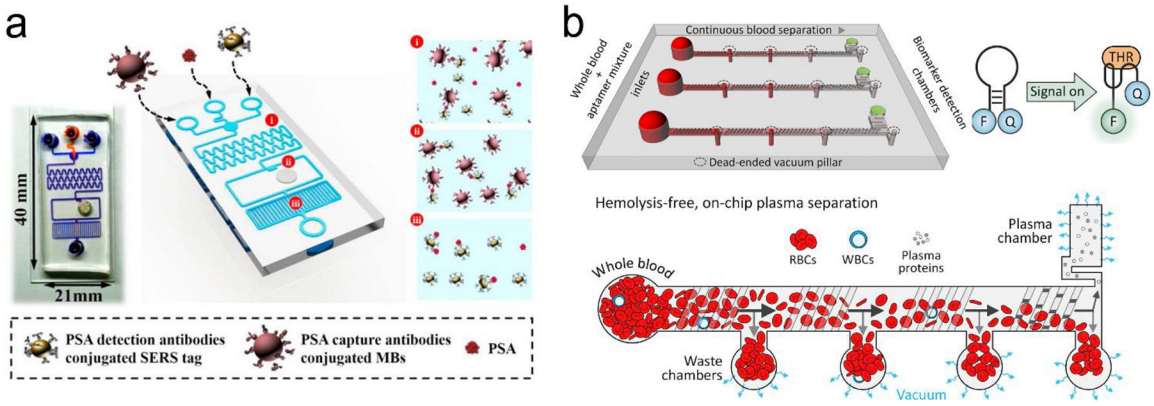

Figure 19.

(a) A passive microfluidic device with integrated capillary micropump and SERS probes, consisting of three compartments for: (i) mixing sample and reagents; (ii) preloading reagents and detecting; (iii) capillary pump. (B) A passive microfluidic device with integrated pneumatic micropump and fluorescence SERS probes. Reproduced with permission from (a) ref. 221, copyright 2019, American Chemical Society; (b) ref. 274, copyright 2017, Elsevier.

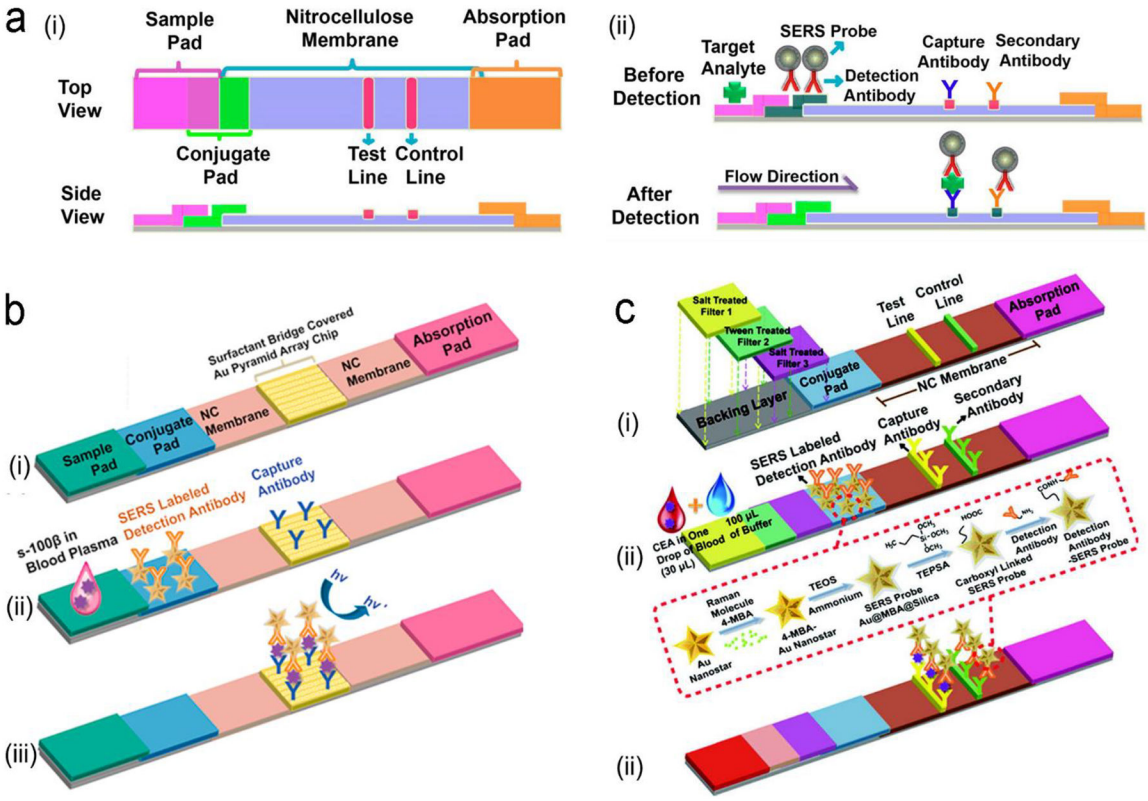

Figure 20.

Structure of PLFS with integration SERS probes. (a) SERS-PLFS for detection of traumatic brain injury (TBI) protein biomarker in diluted blood plasma samples. (i) basic constructure of PLFS; (ii) Side view of prestored reagents in the PLFS before detection; (iii) Side view after detection. (b) Gold nanostar@Raman reporter@silica sandwiched nanoparticles coupled with Au pyramid array for detection of TBI biomarker S-100β in blood plasma. (i) structure; (ii) before detection; (iii) after detection. (c) SERS-PLFS with a built-in plasma separation unit for whole blood detection. (i) structure; (ii) before detection; (iii) after detection. Reproduced with permission from (a) ref. 67, copyright 2017, American Chemical Society; (b) ref. 291, copyright 2021, Elsevier; (c) ref. 292, copyright 2020, American Chemical Society.

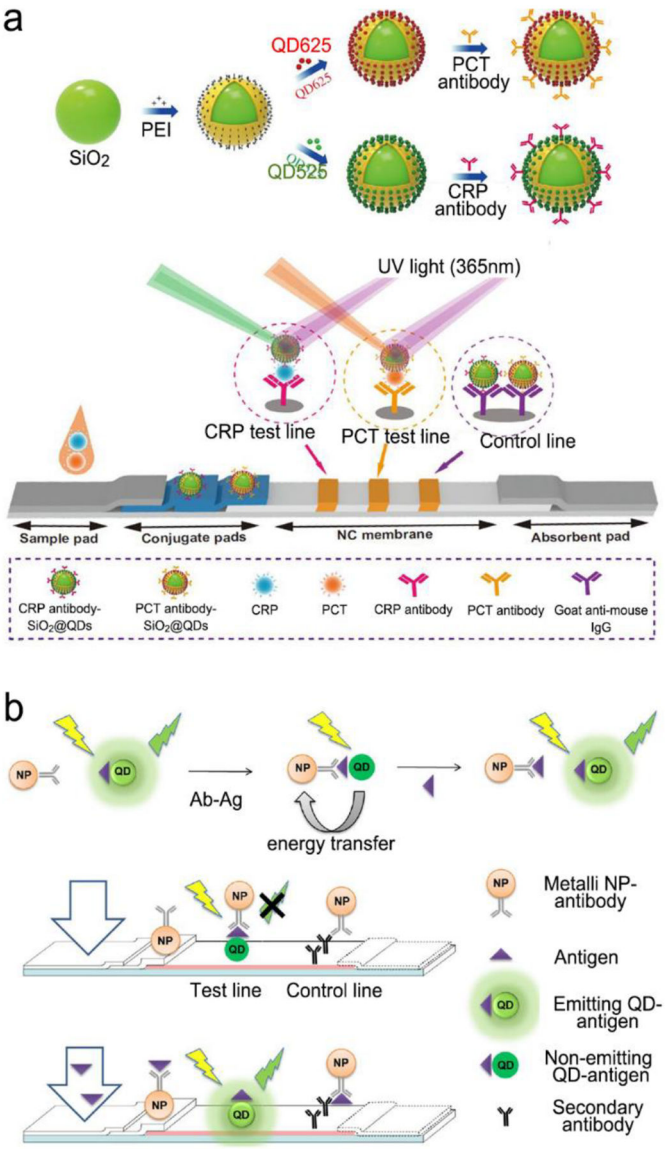

Figure 21.

Fluorescent PLFS. (a) PLFS using dual QD nanobeads for simultaneous detection of two sepsis biomarkers. (b) Competitive assay based on the “turn-on” fluorescence signal in PLFS. Reproduced with permission from (a) ref. 293, copyright 2020, Springer Nature; (b) ref. 295, copyright 2018, Springer Nature.

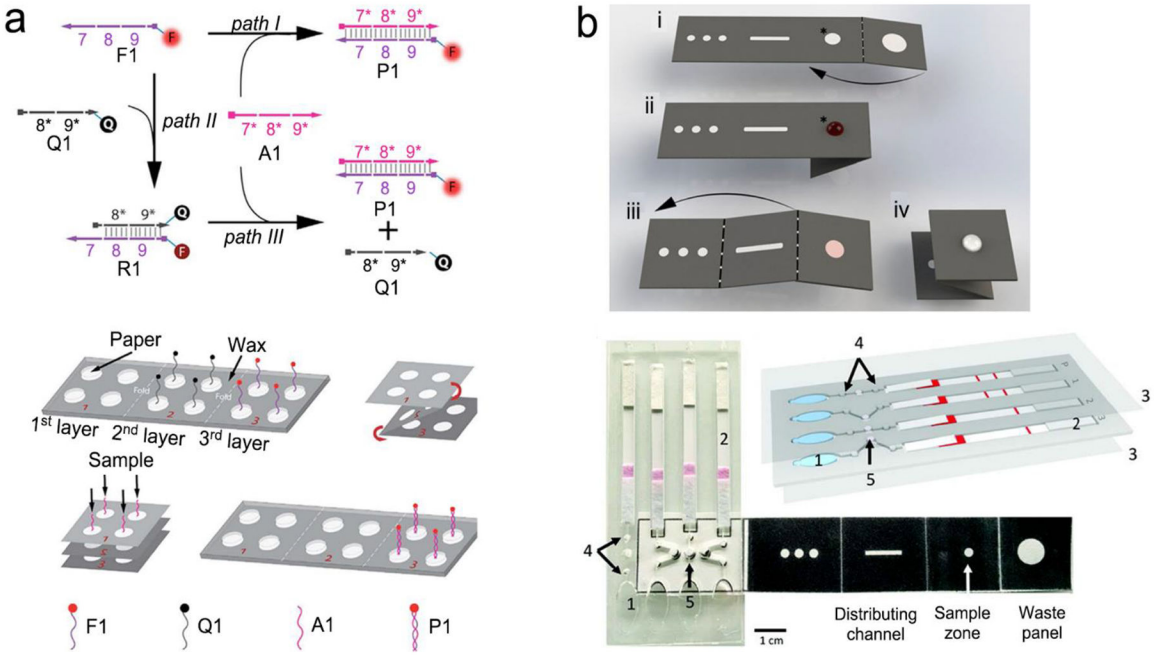

Figure 22.

Advanced structures of PLFS. (a) An origami paper-based devices for nucleic acid detection. (b) Hybrid device nucleic acid extraction, amplification and detection by combination of origami paper for extraction of nucleic acid, plastic microfluidic device for LAMP reaction and paper-based strip for detection of malaria DNA. Reproduced with permission from (a) ref. 310, copyright 2013, American Chemical Society; (b) ref. 2, copyright 2019, National Academy of Sciences.

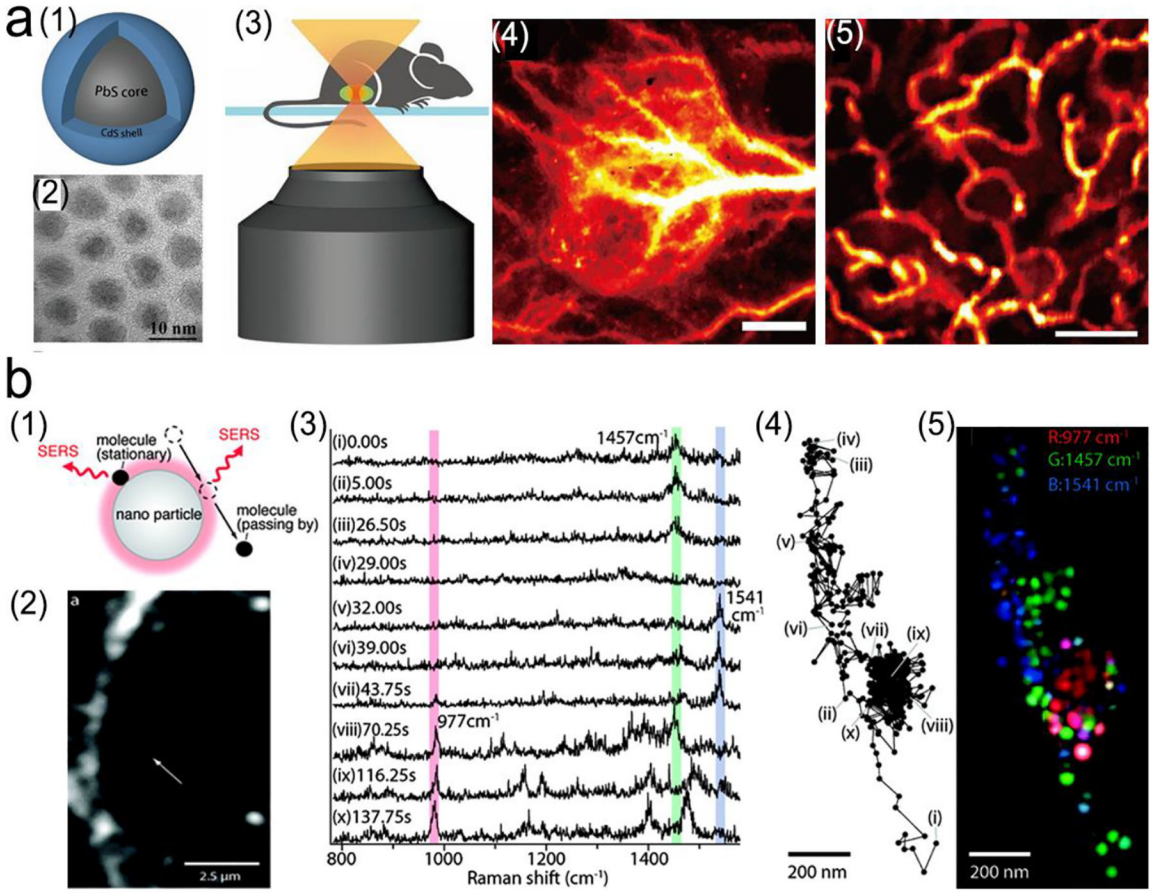

Figure 23.

Direct imaging of tissues with stained NIR fluorescence or SERS probes. (a) *In vivo* fluorescence imaging of tumor tissues through tail vein injection of PbS/CdS QDs into a mouse with xenograft MC38 tumors. (1) Schematic structure of PbS/CdS QDs probe. (2) TEM image of QDs. (3) Schematic illustration of non-invasive *in vivo* confocal imaging of the mouse through the skin; (4) *In vivo* wild-field fluorescence imaging of tumor tissues after tail vein injection of QDs. Scale bar: 1 mm; (5) Confocal fluorescence imaging of tumor vessels at a depth of ~180 μm. Scale bar: 200 μm. (b) SERS imaging of characteristic biomolecules in cells. (1) SERS signals from absorbed molecules and changes with their distance to gold nanoparticles. (2) A photo of a macrophage cell using dark-field microscope and the gold nanoparticle shown as a small white spot (white arrow) under dark-field microscope. (3) SERS spectra obtained form (a) with three characteristic peaks of phosphate at 997 cm^{-1}, CH_2 and CH_3 at 1457 cm^{-1}, Amid II at 1541 cm^{-1}. (4) Trajectory of a gold nanoparticle under dark-field microscope. (5) False-color mapping of the molecular distribution based on the trajectory of the nanoparticle form (4). Reproduced with permission (a) ref. 360, copyright 2018, National Academy of Sciences; (b) ref. 361, copyright 2011, American Chemical Society.

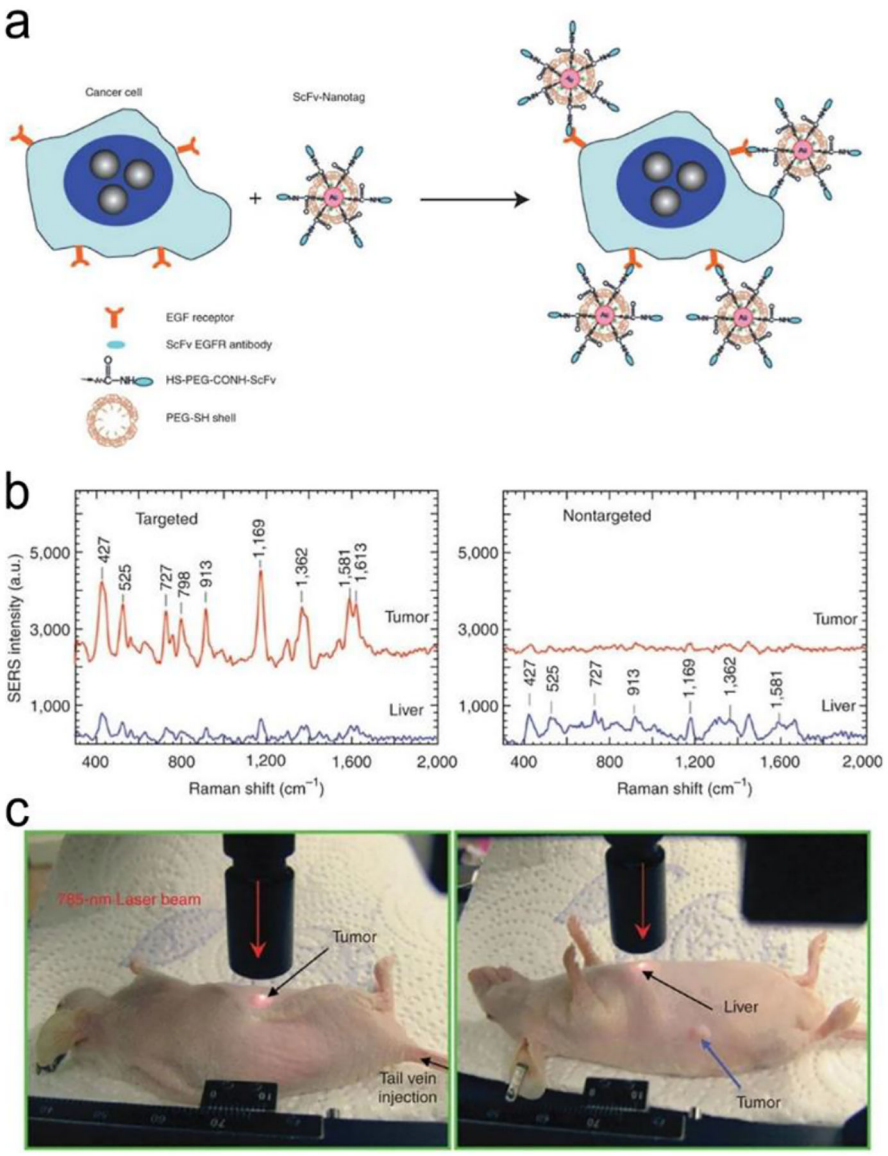

Figure 24.

In vivo cancer targeting and SERS detection using the PEGlyated SERS probes conjugated with the single-chain variable fragment (ScFv) antibodies, which can recognize the tumor biomarker epidermal growth factor receptor (EGFR). (a) Schematic illustration of the structure of the PEGlyated SERS probes. (b) *In vivo* SERS spectra obtained from the targeting and non-targeting SERS probes. (c) Photographs illustrating a 785 nm laser beam focusing on the tumor site or on the anatomical location of liver. Reproduced with permission ref. 368, copyright 2008, Springer Nature.

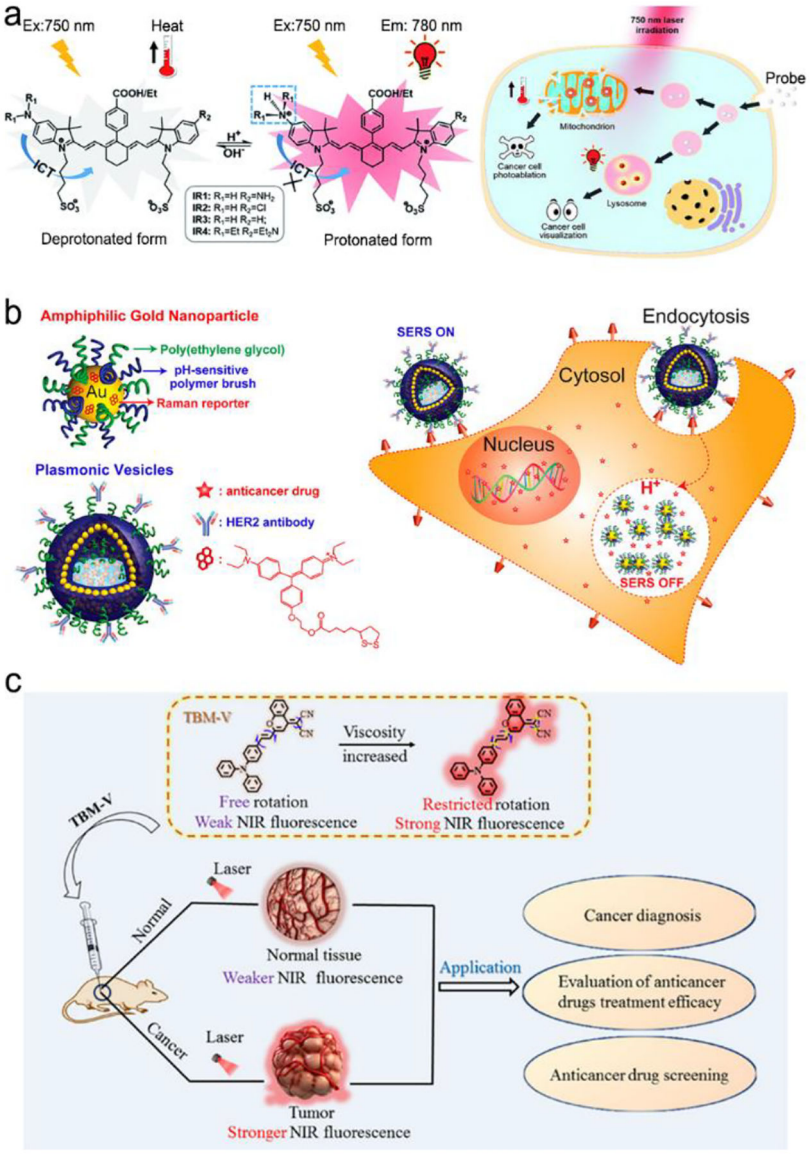

Figure 25.

Biomarker-triggered imaging. (a) pH activated electron transfer (ET) process in an organic NIR dye for cancer cell visualization. (b) Drug-loaded and targeted plasmonic vesicles for cancer cell targeting, imaging and therapy via pH-sensitive drug release. (c) Viscosity activated *in vivo* imaging of tumor tissue. Reproduced with permission (a) ref. 372, copyright 2016, The Royal Society of Chemistry; (b) ref. 375, copyright 2012, American Chemical Society; (c) ref. 376, copyright, American Chemical Society;

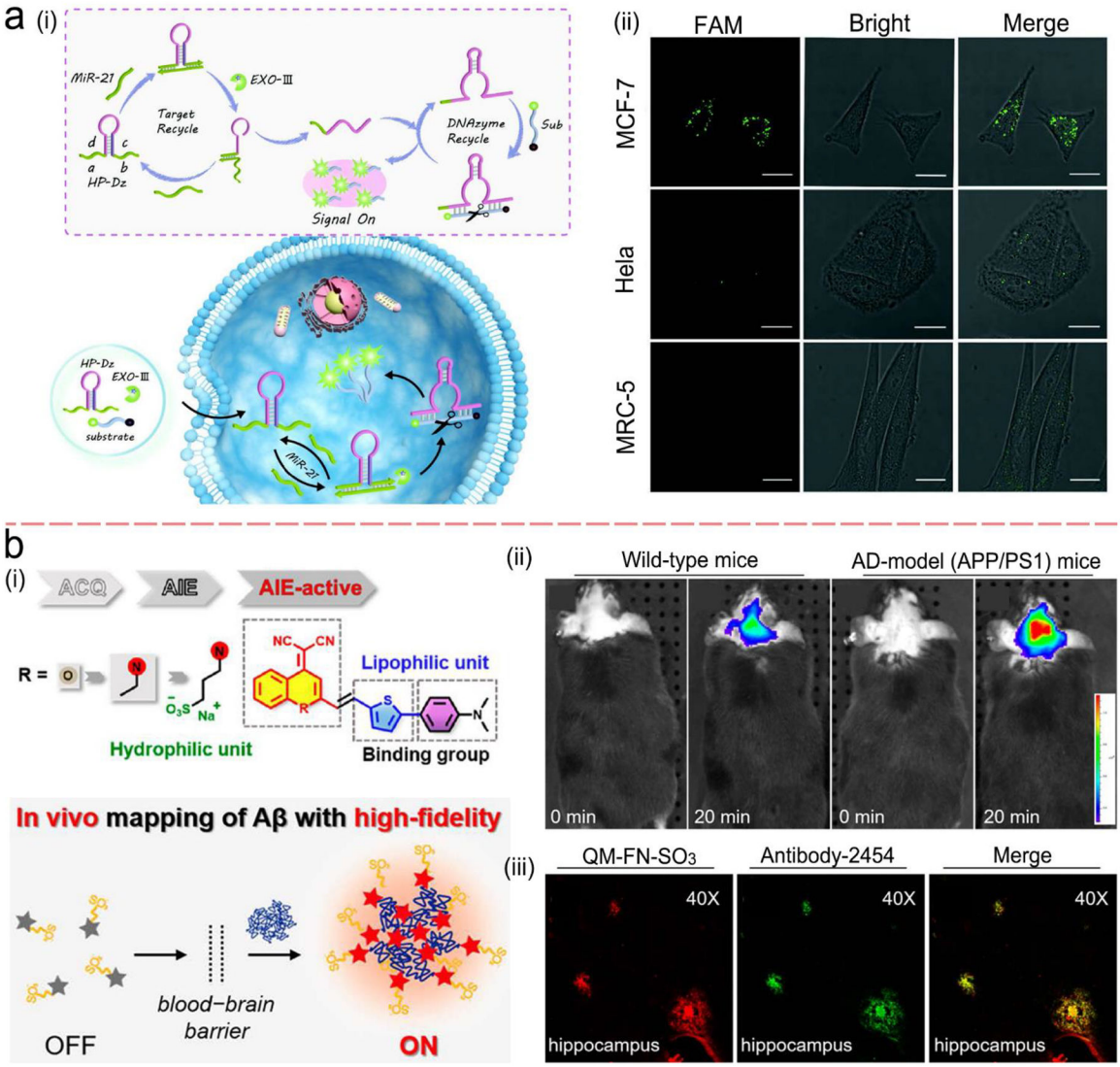

Figure 26.

(a) MicroRNA-21(miR-21)-activated imaging through a FRET process together with Exo-III-assisted nucleic acid amplification. (i) Schematic illustration of the imaging process; (ii) Fluorescence imaging of miR-21 in breast cancer cells (MCF-7) with high miR-21 expression, Hela cells with low miR-21expression and MRC-5 cells with no miR-21expression. The scale bar is 20 μm. (b) Amyloid-β (Aβ) plaque-activated AIE process for *in situ* imaging of Alzheimer's disease (AD). (i) Schematic illustration of synthesis of AIE probe and imaging process; (ii) *In vivo* imaging of Aβ deposition in the AD model (APP/PS1transgenic) mice in comparison to normal wild-type mice; (iii) *Ex vivo* fluorescence imaging of brain slices from APP/PS1 mice after injection of the AIE probes (QM-FN-SO3) with colocalization of the Aβ plaques stained with anti-Aβ antibody-2454. Reproduced with permission from (a) ref. 377, copyright 2020, American Chemical Society.; (b) ref. 379, copyright 2019, American Chemical Society.

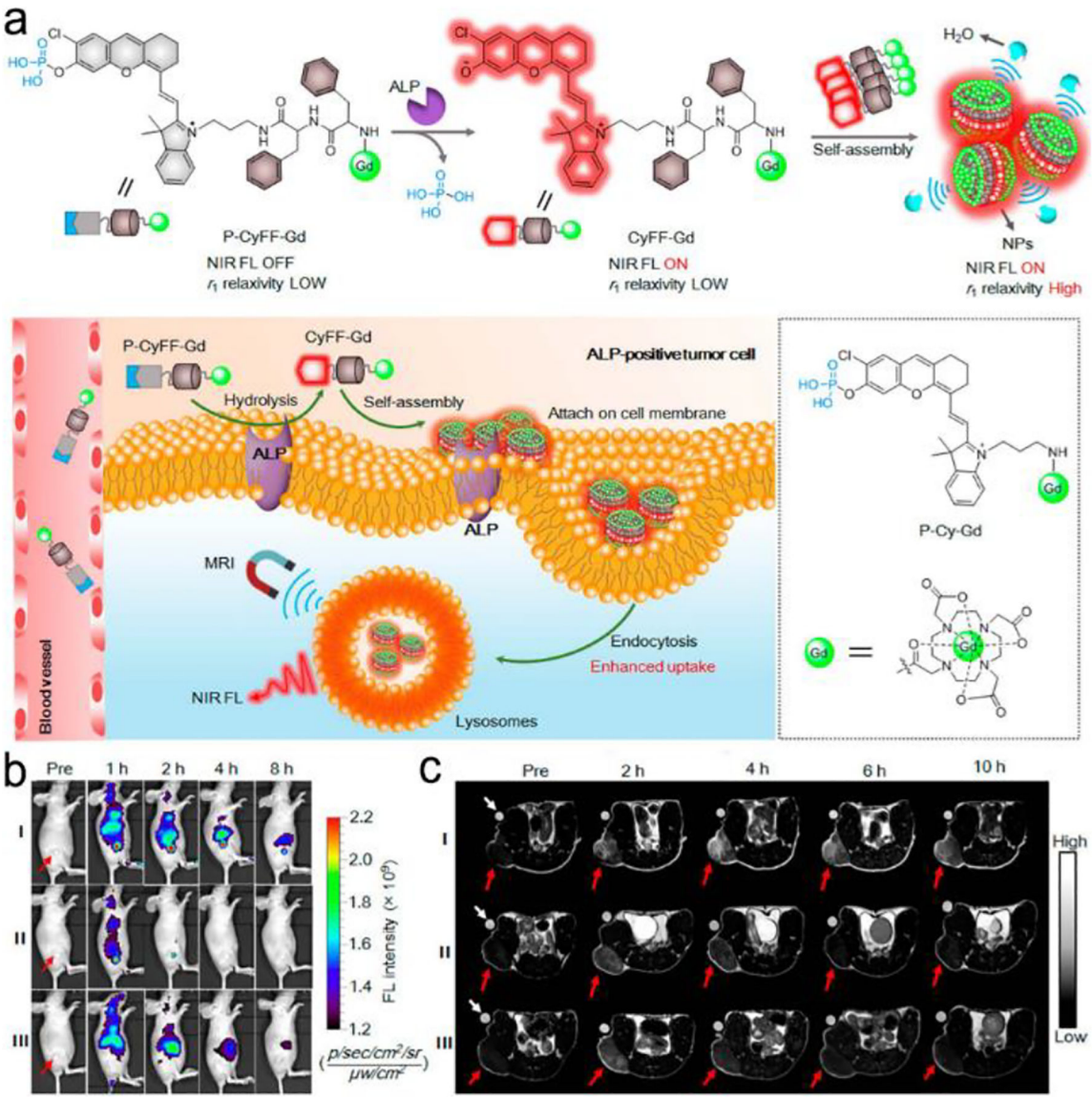

Figure 27.

In vivo bimodal imaging for tumor tissue visualization: Alkaline phosphatase (ALP) reaction-triggered ET imaging combined with magnetic resonance imaging (MRI). (a) Chemical mechanism of the ALP reaction-triggered NIR fluorescence imaging and the self-assembly for further signal amplification; (b) Schematic illustration of *in vivo* bimodal imaging of ALP-positive tumor cells; (c) ALP reaction-triggered NIR fluorescence imaging (left) and MRI imaging (right). Reproduced with permission from ref. 380, copyright 2019, American Chemical Society.